Hardware-Aware Precoding and Digital Predistortion for Massive MIMO Transmitters

by

Mohammed Almoneer

A thesis
presented to the University of Waterloo
in fulfillment of the
thesis requirement for the degree of
Doctor of Philosophy
in
Electrical and Computer Engineering

Waterloo, Ontario, Canada, 2022

© Mohammed Almoneer 2022

Examining Committee Membership

The following served on the Examining Committee for this thesis. The decision of the Examining Committee is by majority vote.

External Examiner: Mohamed Helaoui
Professor, Dept. of Electrical and Computer Engineering,
University of Calgary

Supervisors: Slim Boumaiza
Professor, Dept. of Electrical and Computer Engineering,
University of Waterloo

Patrick Mitran
Professor, Dept. of Electrical and Computer Engineering,
University of Waterloo

Internal Members: Vincent Gaudet
Professor, Dept. of Electrical and Computer Engineering,
University of Waterloo

Weihua Zhuang
Professor, Dept. of Electrical and Computer Engineering,
University of Waterloo

Internal-External Member: Baris Fidan
Professor, Dept. of Mechanical and Mechatronics Engineering,
University of Waterloo

Author's Declaration

I hereby declare that I am the sole author of this thesis. This is a true copy of the thesis, including any required final revisions, as accepted by my examiners.

I understand that my thesis may be made electronically available to the public.

Abstract

To cope with the ever-increasing demand for higher data rates, reduced latency, and improved coverage, new technologies are needed to advance the current state of wireless communication systems. One of the promising new additions to fifth-generation (5G) basestations is the use of massive multiple-input multiple-output (MIMO) technology. The key concept is to equip the basestation with tens or hundreds of radio-frequency (RF) transceiver chains, all utilizing the same time-frequency resources simultaneously. The additional degrees of freedom this offers allows the basestation to serve multiple users in the same resource block and enables multi-fold improvements in spectral efficiency. Nevertheless, this increase in the number of chains, coupled with the expected increase in transmission bandwidths, complicates the hardware design process and magnifies the impact of hardware imperfections on the system performance.

Mitigating hardware limitations and imperfections in conventional single-input single-output (SISO) transmitters is a well-established discipline, and extending most of the techniques developed for SISO transmitters to the MIMO case is relatively straightforward. The most prominent exception to this, however, is digital predistortion (DPD), which has been the most popular power amplifier (PA) linearization technique for the past three decades. The successful application of DPD to massive MIMO transmitters faces two major challenges. First, reducing the size and cost of the basestation necessitates placing the transmitter antennas in close proximity, which leads to unavoidable inter-antenna coupling. The combination of the PAs' nonlinearity and inter-antenna coupling gives rise to nonlinear crosstalk effects that cannot be mitigated using conventional DPD techniques. This phenomenon is exacerbated by the need to track the dynamic multi-user channel and update the employed precoding accordingly, the result of which is the constant variation in the average-power levels transmitted by the different PAs. Second, since tens or hundreds of low-power PAs are to be employed instead of a single high-power one, the overhead power budget for per-chain DPD must be reduced to maintain a reasonable overall efficiency. The power overhead incurred includes the power consumed by the real-time DPD engine, as well as that consumed by the transmitter-observation receiver (TOR) needed to train the DPD module.

The main objective of this work is developing robust and effective digital signal processing (DSP) techniques that mitigate the combined effects of PA nonlinearity and antenna crosstalk in massive MIMO transmitters. The thesis starts by investigating the impact of precoding on the average-power levels transmitted by the different RF chains, and analyzing the effect this has on the active impedances seen by the PAs in the presence of antenna crosstalk. It is shown that, although precoding is a system-level function that mit-

igates multi-user channel effects, it has a direct impact on the RF performance of the PAs. Hence, the DPD and precoding subsystems cannot be operated independently from one another. Based on this analysis, we propose two solutions to the problem. The first comprises a load-dependent DPD architecture and a low-complexity algorithm that reduces the disparity in average-power levels arising from conventional precoding schemes. The second solution comprises alternate precoding schemes that fully eliminate the disparity in average-power levels across the RF chains and, consequently, simplify the required DPD architecture. Both solutions ensure a stable performance across all channel conditions.

The second objective of this work is reducing the computational and power overheads of the DPD subsystem. To this end, we propose a computationally efficient algorithm for estimating the delay and phase offsets between the transmitter and the TOR used for DPD training. The proposed algorithm is less resource-consuming and more accurate than the exhaustive search methods employed in the literature. In addition, we propose a low-complexity real-time DPD architecture that requires less hardware resources to implement, introduces less latency, and consumes less power when compared with prior works.

Acknowledgements

All praise be to God for making this possible.

I would like to express my sincere gratitude to my supervisors, Professors Slim Boumaiza and Patrick Mitran, for providing me with this opportunity and guiding me through every step of the way. By virtue of their patience and support, I have been able to develop my research skills and gain invaluable experience. I would also like to thank my committee members for taking the time to review this work, and for their valuable feedback.

I feel fortunate to have made so many friends during this journey, and I want to thank them for the memories we shared. Special thanks are due to my friends and colleagues in the EmRG group for their companionship and helpfulness.

Finally, my deepest gratitude is towards my parents. Their unconditional support and encouragement is what motivates me to succeed. They have always been there for me and have helped me in everything I have pursued.

Table of Contents

List of Figures

List of Tables

List of Abbreviations

5G fifth-generation

ACPR adjacent-channel power ratio

ADC analog-to-digital converter

AM/AM amplitude-modulation to amplitude-modulation

AWG arbitrary waveform generator

AWGN additive white Gaussian noise

CORDIC coordinate-rotation digital computer

CSI channel state information

CTMM crosstalk and mismatch

CW continuous-wave

DAC digital-to-analog converter

DDC digital down-conversion

DISO dual-input single-output

DPD digital predistortion

DSP digital signal processing

EP equal-power

FFs flip-flops

FIR finite impulse response

FPGA field-programmable gate array

GaN Gallium Nitride

I/Q In-phase/Quadrature-phase

IF intermediate-frequency

LOS line-of-sight

LS least-squares

LUT look-up table

MIMO multiple-input multiple-output

ML maximum-likelihood

MMSE minimum mean-square error

MP memory polynomial

MRT maximum-ratio transmission

MSE mean-square error

OFDM orthogonal frequency-division multiplexing

PA power amplifier

PAPR peak-to-average power ratio

PHD polyharmonic distortion

PWL piece-wise linear

RF radio-frequency

RFLOP real-valued floating-point operation

RLS recursive least-squares

RNMSE root normalized mean-square error

RZF regularized zero-forcing

S-parameters scattering parameters

SINR signal-to-interference-and-noise ratio

SISO single-input single-output

SNR signal-to-noise ratio

SOCP second-order cone program

TDD time-division duplex

TOR transmitter-observation receiver

ZF zero-forcing

Notation

$\text{Re}\{z\}$	Real part of z
$\text{Im}\{z\}$	Imaginary part of z
z^*	Conjugation of z
$|z|$	Absolute value of z
$\mathbf{a}$	Bold lowercase letters denote column vectors
$\underline{\mathbf{a}}$	Bold underlined lowercase letters denote row vectors
$\|\mathbf{a}\|$	2-norm of $\mathbf{a}$
$\mathbf{A}$	Bold uppercase letters denote matrices
$(\mathbf{A})_{i,j}$	The ith-row-j^{th}-column element of $\mathbf{A}$
$A_{i,j}$	The ith-row-j^{th}-column element of $\mathbf{A}$
$\mathbf{A}^T$	Transpose of $\mathbf{A}$
$\mathbf{A}^H$	Conjugate transpose of $\mathbf{A}$
$\mathbf{A}^\dagger$	Moore–Penrose pseudoinverse of $\mathbf{A}$
$\text{tr}(\mathbf{A})$	Trace of $\mathbf{A}$
$\text{vec}(\mathbf{A})$	The vector obtained by stacking the columns of $\mathbf{A}$
$\|\mathbf{A}\|_F$	Frobenius norm of $\mathbf{A}$
$\mathbf{A} \otimes \mathbf{B}$	Kronecker product of the two matrices $\mathbf{A}$ and $\mathbf{B}$
$\mathbf{0}_{M \times N}$	$M \times N$ all-zero matrix
$\mathbf{I}_M$	$M \times M$ identity matrix
$\text{diag}([a_1, \ldots, a_M])$	$M \times M$ diagonal matrix whose diagonal elements are a_1 to a_M
$\text{card}(S)$	Number of elements in the set S
$\lceil a \rceil$	Least integer greater than or equal a
$\lfloor a \rfloor$	Greatest integer less than or equal a
$a \bmod b$	Remainder of the integer division a/b (between 0 and $b-1$)

Chapter 1

Introduction

1.1   Motivation

A number of technological advances have fundamentally changed our world, but none more so than the evolution of consumer electronics. The use of electronic devices permeates into every facet of our everyday lives; from personal computers and mobile phones to smart watches and fitness gadgets. The enormous volumes of data generated by these devices, and the need for handling and transferring them securely and reliably, is what drives the continuous development in networking and cellular infrastructure. Next-generation cellular networks should be able to address not only the current demand, but also that expected with the adoption of new technologies, such as self-driving cars and smart homes. 5G cellular networks are envisioned to cope with the expected multi-fold increase in data rates and number of connected devices, all while maintaining a negligible round-trip latency and a high quality of service [1, 2]. The main challenge to achieving these objectives is to increase the data throughput of 5G basestations beyond the capabilities of those of predecessor cellular systems.

While the traditional approaches to increasing system capacity have been to utilize more spectrum and densify the deployment of access points, these alone will not suffice in meeting 5G requirements. Improving the spectral efficiency in the utilized band is, thus, essential. One of the key enabling technologies in 5G basestations is the use of massive MIMO transceivers [3–5]. A 5G basestation is expected to feature tens or hundreds of RF transceiver chains, all utilizing the same time-frequency resources simultaneously. The use of multiple chains, and the additional degrees of freedom this offers, is the only viable approach to attaining substantial improvements in spectral efficiency [6]. Nevertheless,

1

this increase in the number of chains, coupled with the expected increase in transmission bandwidths, brings about new challenges that were not present in predecessor cellular systems. Not only does the hardware design process become more challenging, but so does the implementation of the associated DSP functions.
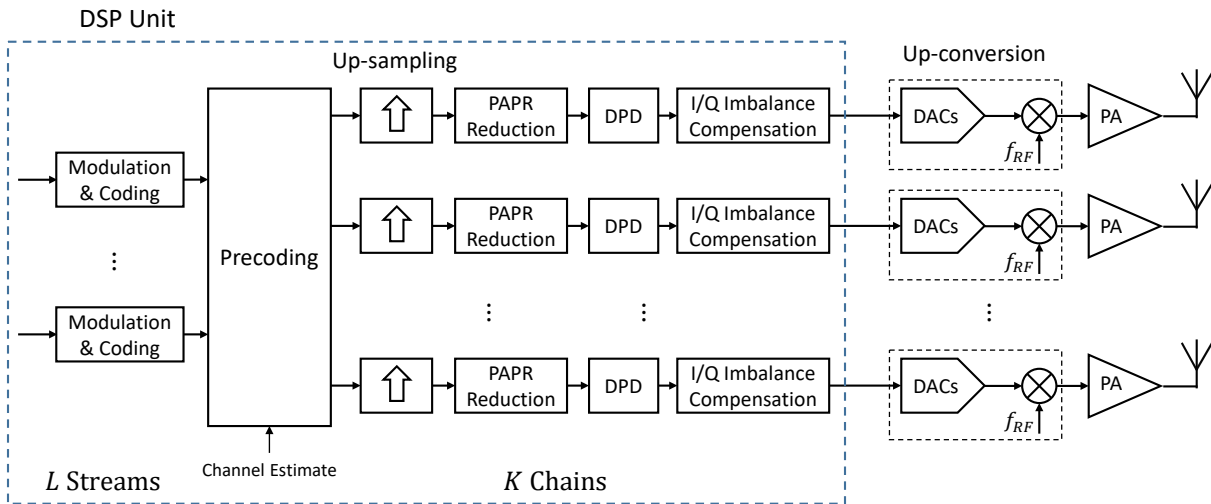
Figure 1.1: Block diagram of a fully digital massive MIMO transmitter.

Fig. 1.1 shows the block diagram of a fully digital massive MIMO transmitter system that comprises K RF chains and serves $L < K$ users. Each of the K chains employs an up-conversion unit, a PA, and an antenna. This architecture is to be utilized in transmitters that cover traditional sub-6 GHz bands, and may also be deployed in their millimeter-wave counterparts [7]. Besides carrying out the essential functions of modulation, forward error-coding, channel estimation, and precoding, the DSP unit must also compensate for hardware limitations and imperfections. Digital compensation and pre-processing techniques for SISO transceiver systems are relatively well-studied [8]. The four main pre-processing modules in almost every SISO transmitter are upsampling, peak-to-average power ratio (PAPR) reduction, DPD, and In-phase/Quadrature-phase (I/Q) imbalance compensation. These modules are also needed in MIMO transmitters as shown in Fig. 1.1.

All four pre-processing functions in Fig. 1.1 are direct extensions of their counterparts in SISO systems, with the exception of DPD. DPD is almost always necessary to compensate for PA nonlinearity, which degrades the transmitted signal quality and causes spectral regrowth that interferes with adjacent frequency bands. DPD techniques for SISO systems are relatively well-studied [9], but extending them to the MIMO case is not straightforward. This is because of the high level of integration required in 5G basestations to reduce fabri-

cation and operation costs, whereby the transmitter antennas are situated closely together and inevitable inter-antenna coupling arises. The combination of the PAs' nonlinearity and inter-antenna coupling gives rise to nonlinear crosstalk effects that cannot be mitigated by employing a conventional SISO DPD module in each chain [10–12]. This problem can be circumvented by introducing RF isolators between each PA-antenna pair, which would isolate each PA from its terminating antenna and protect against crosstalk-induced effects. However, implementing such a solution is challenging since isolators are bulky and expensive.

Therefore, effective signal processing techniques are needed to mitigate the resulting distortions and ensure that signal quality requirements are met. Over the past decade, there have been numerous works on the MIMO-DPD problem, but it was only recently that practical solutions were developed [13]. The main problem with these solutions, however, is that they do not consider the impact precoding has on the RF performance. In a multi-user MIMO system, precoding serves to mitigate the free-space channel and ensure that each user terminal receives its intended signal, with little to no interference from other users. Precoding dictates the average-power levels across the different RF chains and, consequently, the power levels of the crosstalk signals impacting the different PAs. Since the free-space channel is time-varying, the employed precoding must be updated accordingly, which can lead to channel-dependent variations in RF performance. It is, therefore, crucial to develop a MIMO-DPD solution that takes precoding into account.

Another challenge facing the implementation of DPD in massive MIMO systems is energy efficiency. Since basestation transmitters are expected to employ tens or hundreds of low-power PAs instead of a single high-power one, the overhead power margin for per-chain DPD (as a percentage of the PA transmit power) must be reduced to maintain a reasonable overall efficiency. The power overhead incurred includes the power consumed by the logic circuits in the always-running DPD engine and that consumed by the TOR required to capture the PA output and update the DPD coefficients. Both sources of power consumption scale up with the instantaneous transmission bandwidth, which is expected to increase from the current 5-20 MHz to hundreds of MHz.

1.2   Thesis Objectives

This thesis aims at developing efficient and reliable DSP algorithms that address the combined effects of PA nonlinearity and antenna crosstalk in massive MIMO systems. The objectives of this work are as follows:

1. Analyzing the effects of antenna crosstalk and precoding on the linearizability of the PAs in a highly-integrated MIMO system, and developing a MIMO-DPD architecture that takes these effects into account.

2. Developing new precoding schemes that exploit the additional degrees of freedom offered in a massive MIMO system, with the aim of reducing the requirements on the RF front ends and simplifying the DPD subsystem.

3. Devising a low-complexity DPD architecture and training algorithm that reduce the computational and power overheads of both the real-time DPD engine and the TOR required for training.

1.3 Thesis Outline

This thesis is organized as follows. Chapter 2 presents the necessary background theory for the following chapters. It begins with an overview on massive MIMO systems before presenting a detailed description of the theory behind SISO DPD, and how it can be extended to the MIMO case. The chapter also explains the nuances of downlink precoding and reviews conventional linear precoding methods.

Chapter 3 begins with analyzing the effects of antenna crosstalk and precoding on the active load impedances seen by the PAs. This analysis is then used to devise a low-complexity precoding technique and a load-dependent DPD structure that ensure reliable performance across all operating conditions. The proposed architecture is experimentally validated on a prototype MIMO transmitter.

Chapter 4 presents the proposed precoding schemes. Unlike conventional precoders, the proposed ones ensure that all PAs transmit at the same average-power level. The proposed precoders ease the requirements on the RF front ends and reduce the complexity of the DPD engine, as exemplified by the numerical simulations and experimental results presented.

Chapter 5 presents a computationally efficient algorithm for estimating the delay and phase offsets associated with the TOR used for DPD training. The chapter also presents a low-complexity real-time DPD architecture that reduces the power consumption of the DPD engine below that incurred in prior works.

Finally, Chapter 6 concludes this work by summarizing the contributions and outlining possible directions for future research.

Chapter 2

Background Theory

This chapter presents the necessary background theory and lays the theoretical foundations for the following chapters. We start by briefly describing the massive MIMO system architecture and outlining the main DSP functionalities. We then present a detailed description of the two DSP challenges tackled in this work, namely, DPD and precoding.

2.1 Introduction to Massive MIMO Systems

2.1.1 The Fully Digital MIMO Architecture

Massive MIMO is one of the key enabling technologies in 5G and future wireless systems. The basic concept is to equip the basestation with tens or hundreds of RF transceiver chains, all utilizing the same time-frequency resources simultaneously. The additional degrees of freedom this offers allows the basestation to serve multiple users in the same resource block and enables multi-fold improvements in spectral efficiency [4–6]. Fig. 2.1 shows the basic idea behind massive MIMO. A basestation equipped with a large number of antennas, K, serves L single-antenna user terminals that are not co-located. While the term "massive" implies that $L \ll K$, significant performance gains can still be obtained with K/L ratios as small as 2 [14].

During the uplink phase, the basestation has to separate the signals corresponding to the different users. Whereas during the downlink phase, the basestation *precodes* the users' signals so as to counteract the free-space channel and ensure that each terminal receives only its intended signal (note that the notion of precoding in a MIMO system is completely

different from that in a SISO one, cf., [15–17]). Accordingly, the basestation must estimate both the uplink and downlink channels. Both channels are the same in time-division duplex (TDD) operation, assuming proper reciprocity calibration [18]. In this mode, the basestation acquires knowledge of the channel from the pilot signals transmitted by the user terminals during the uplink phase [6].

(a) Downlink.

(b) Uplink.
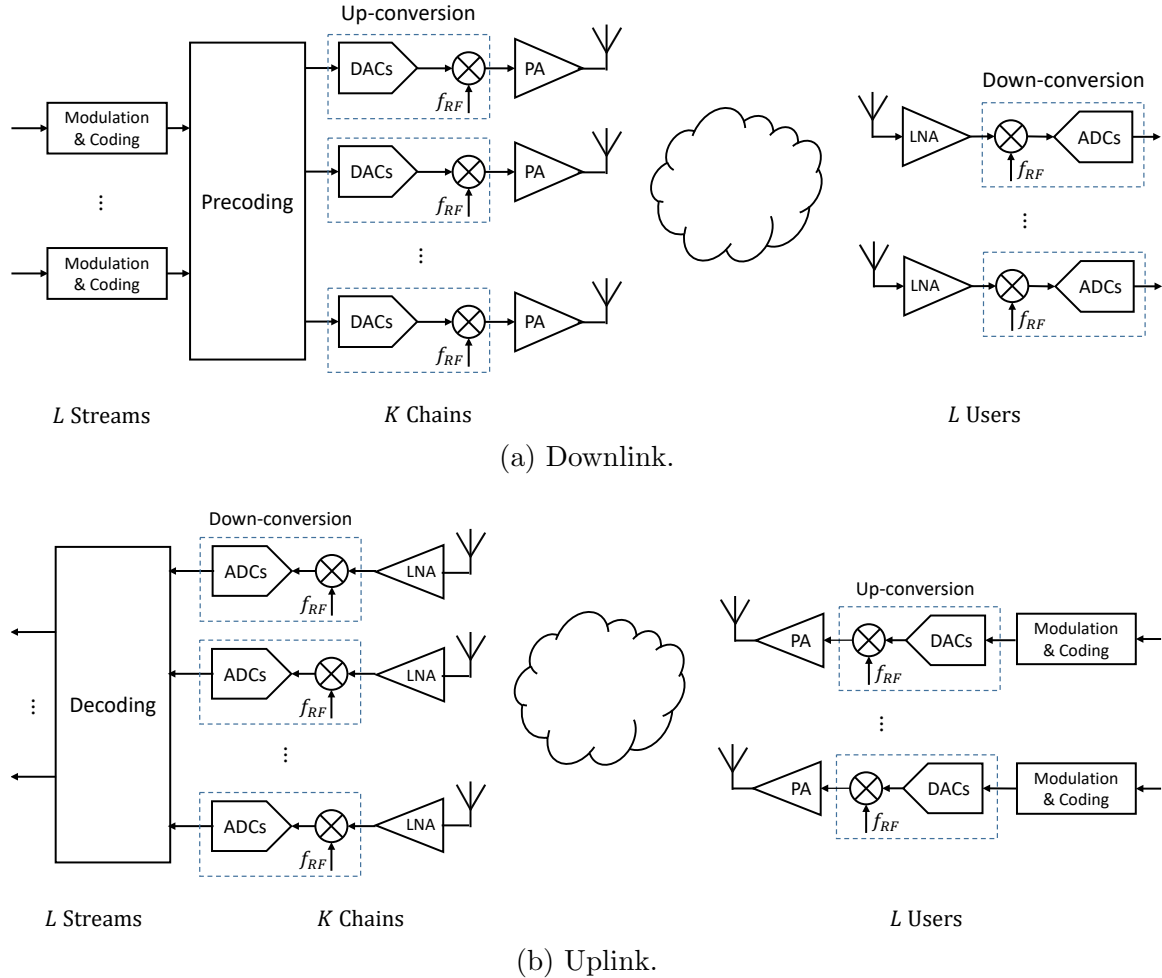
Figure 2.1: The fully digital massive MIMO architecture.

The basestation architecture, shown in Fig. 2.1, is fully digital, in the sense that each RF chain has a digital input. Less complex hybrid analog-digital architectures, such as that shown in Fig. 2.2, are also possible [19]. Hybrid architectures offer appreciable reductions in terms of hardware complexity and power consumption, at the expense of reduced

6

flexibility and performance [20]. These sub-optimal architectures are not suitable for deployment in dense sub-6 GHz urban environments, which feature rich multi-path scattering, but can be cost effective when deployed in line-of-sight (LOS)-dominated millimeter-wave environments [21, 22]. In this work, we only consider the fully digital architecture.
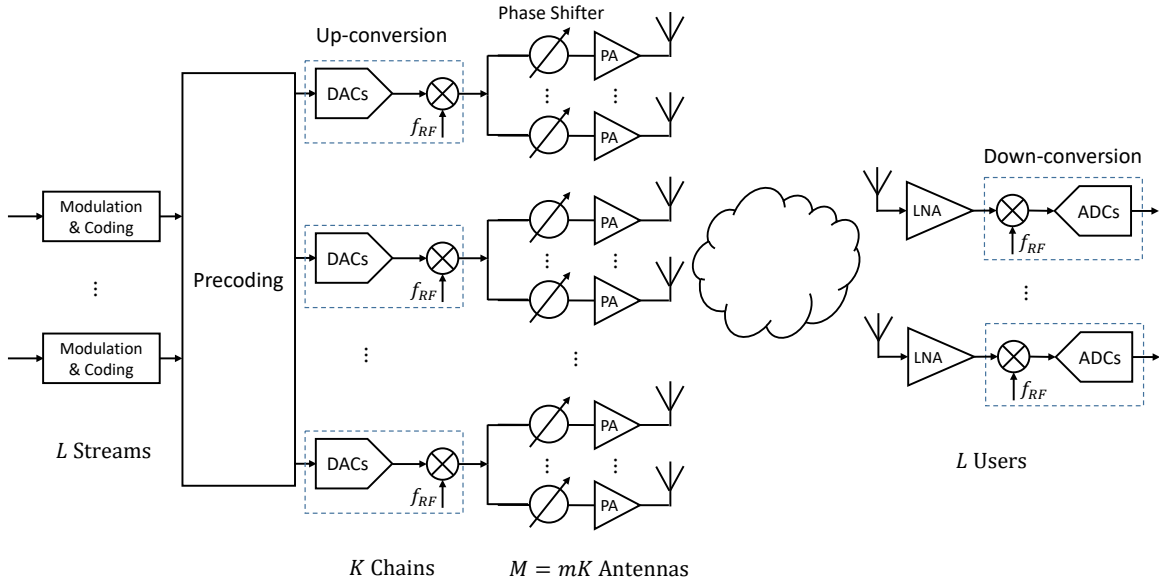
Figure 2.2: Downlink in a hybrid analog-digital massive MIMO system.

2.1.2 Compensating Hardware Imperfections Using DSP

Besides carrying out the essential functions of modulation, forward error-coding, channel estimation, and precoding, the DSP unit in a massive MIMO basestation must also address hardware limitations and imperfections. As shown in Fig. 2.3, the four main pre-processing modules required in each RF chain are up-sampling, PAPR reduction, DPD, and I/Q imbalance compensation. Thus, a more realistic depiction of the MIMO transmitter in Fig. 2.1a is that shown in Fig. 1.1.

The I/Q imbalance compensator serves to mitigate the gain and/or phase imbalances between the In-phase and Quadrature-phase paths in the up-conversion unit. It is only necessary if a direct-conversion configuration (also known as zero-intermediate-frequency (IF)) is utilized [23–25]. The DPD module compensates for PA nonlinearity, which degrades the transmitted signal quality and causes spectral regrowth that interferes with coexisting

communication systems. As Fig. 2.3 shows, training the DPD and I/Q imbalance compensator modules requires a dedicated TOR (a directional coupler plus a down-conversion unit) that captures the PA output signal and feeds it back to the DSP unit. The power overhead incurred by the TOR decreases the overall system efficiency but helps ensure that signal quality requirement are met.
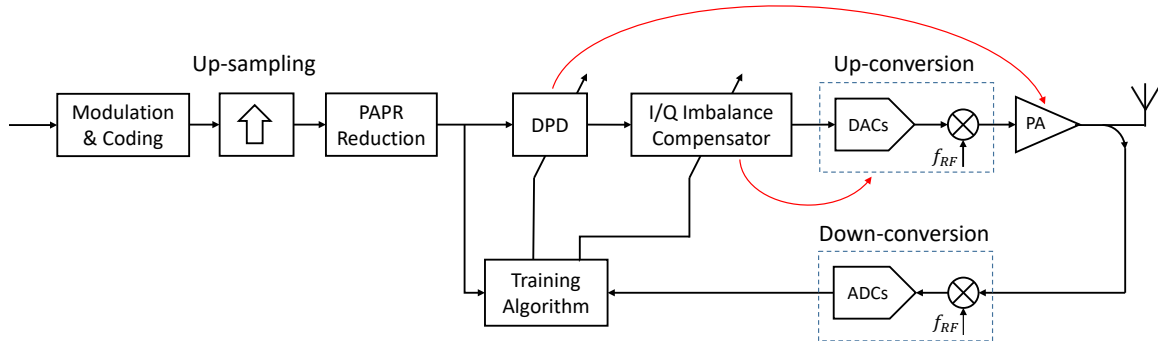
Figure 2.3: A SISO transmitter system with a conventional TOR configuration.

The PAPR reduction module limits the dynamic range of the input signal, which relaxes the resolution requirements on the digital-to-analog converter (DAC) modules and improves the power efficiency of the system. This is because amplifying a high-PAPR signal requires operating the PA in a large average-power-backoff to avoid clipping, which significantly reduces its efficiency [26]. Finally, up-sampling (usually by a factor of 3 to 5) is needed to ensure that PAPR reduction does not generate out-of-band noise [27, 28], and that the DPD module can suppress the out-of-band emissions arising from PA nonlinearity [9].

All pre-processing functions in Fig. 2.3 are readily extendable to the MIMO case, with the exception of DPD. This is because the combination of the PAs' nonlinearity and inter-antenna coupling gives rise to nonlinear crosstalk effects that cannot be fully mitigated by employing conventional SISO DPD techniques [10–12]. This problem is further exacerbated by the impact precoding has on the distribution of average-power levels across the RF chains. Hence, the DPD and precoding subsystems cannot be operated in isolation from one another. In addition, since basestations are now expected to employ tens or hundreds of PAs, the overhead margin for per-chain DPD must be reduced, below that allowed in conventional transmitters, to maintain a reasonable overall efficiency.

To lay out the theoretical foundations for what follows, the remainder of this chapter provides an in-depth exposition of the two DSP functions tackled in this work, namely, DPD and precoding.

2.2 DPD in MIMO Systems

2.2.1 Overview on SISO DPD

(a) Full system.

(b) Baseband-equivalent model.
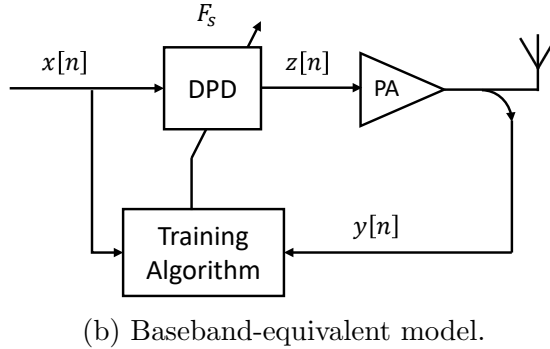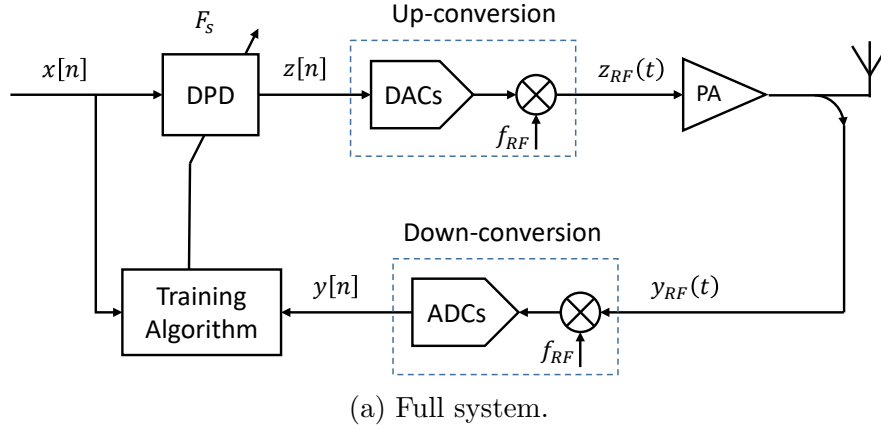
Figure 2.4: DPD in SISO Systems.

Fig. 2.4a shows a streamlined version of the SISO transmitter system in Fig. 2.3. Here, the complex baseband input signal $x[n]$ is that obtained after modulation and coding, up-sampling, and PAPR reduction. The I/Q compensation module, if present, is considered part of the up-conversion unit during DPD training [23]. All baseband processing in Fig. 2.4a is carried out at a rate of F_s samples/sec (which is 3-5 times the rate of the information-bearing signal before up-sampling). The baseband DPD and feedback signals are denoted as $z[n]$ and $y[n]$ respectively, while their continuous-time passband counterparts are denoted as $z_{RF}(t)$ and $y_{RF}(t)$ respectively. Below, we show that a direct relation between the baseband signals ($z[n]$ and $y[n]$) can be derived. Hence, the system in Fig. 2.4a can be reduced to its baseband-equivalent form in Fig. 2.4b.

Modeling PA Nonlinearity

In what follows, we assume that all hardware components in Fig. 2.4a are ideal and that the nonlinearity in the chain is only due to the PA. Assuming certain regularity conditions are satisfied, the input-output relationship of nearly any time-invariant nonlinear system can be represented in terms of a Volterra series. Such representation takes the form [29]

$$
\begin{aligned}
y_{RF}(t) &= \sum_{n=0}^{\infty} H_n \left[z_{RF}(t) \right] \\
&= \sum_{n=0}^{\infty} \int_{\mathbb{R}} \int_{\mathbb{R}} \cdots \int_{\mathbb{R}} h(\tau_1, \ldots, \tau_n) \prod_{r=1}^{n} z_{RF}(t - \tau_r) \; d\tau_1 \ldots d\tau_n \\
&= \sum_{n=0}^{\infty} \int_{\mathbb{R}^n} h(\boldsymbol{\tau}_n) \prod_{r=1}^{n} z_{RF}(t - \tau_r) \, d\boldsymbol{\tau}_n,
\end{aligned}
\tag{2.1}
$$

where $\boldsymbol{\tau}_n = [\tau_1, \ldots, \tau_n]^T$, and $d\boldsymbol{\tau}_n = \prod_{r=1}^{n} d\tau_r$. In this form of representation, $H_n[.]$ is called the nth-order Volterra operator and $h(\tau_1, \ldots, \tau_n)$ is the nth-order Volterra kernel. Note that Volterra kernels generalize the one-dimensional impulse response of linear systems.

If the spectrum of the passband PA input $z_{RF}(t)$ spans a limited bandwidth around the carrier frequency f_{RF}, then $z_{RF}(t)$ can be expressed in terms of its baseband equivalent $z(t)$ as

$$
z_{RF}(t) = \text{Re}\{z(t)e^{j\omega_{RF}t}\} = \frac{1}{2} \left(z(t)e^{j\omega_{RF}t} + z^*(t)e^{-j\omega_{RF}t} \right),
\tag{2.2}
$$

where $\omega_{RF} = 2\pi f_{RF}$. Substituting this expression in (2.1) gives

$$
y_{RF}(t) = \sum_{n=0}^{\infty} \int_{\mathbb{R}^n} \frac{h(\boldsymbol{\tau}_n)}{2^n} \prod_{r=1}^{n} \left(z(t - \tau_r)e^{j\omega_{RF}(t-\tau_r)} + z^*(t - \tau_r)e^{-j\omega_{RF}(t-\tau_r)} \right) d\boldsymbol{\tau}_n.
\tag{2.3}
$$

The expression in (2.3) shows that the PA output contains harmonic components centered around integer multiples of ω_{RF}. Since only the fundamental spectral component of the output signal is of interest, we can assume that other harmonics are filtered out at the PA output. Out of all possible product terms in (2.3), the terms with a carrier component of $e^{j\omega_{RF}t}$ can only be obtained from the product of k conjugated terms $z^*(t - \tau_r)e^{-j\omega_{RF}(t-\tau_r)}$ and $k + 1$ non-conjugated terms $z(t - \tau_r)e^{j\omega_{RF}(t-\tau_r)}$. These desired terms constitute a subset of all terms arising from a product with an odd order, i.e., $n = 2k + 1$. If the Volterra kernels $h(\boldsymbol{\tau}_n)$ are assumed to be symmetric functions of their arguments, i.e., any permutation of the arguments does not alter the function values, then (2.3) reduces to [30]

$$
y_{RF}(t) = \frac{1}{2} \left(y(t)e^{j\omega_{RF}t} + y^*(t)e^{-j\omega_{RF}t} \right),
\tag{2.4}
$$

10

where

$$y(t) = \sum_{k=0}^{\infty} \int_{\mathbb{R}^{2k+1}} f(\boldsymbol{\tau}_{2k+1}) \prod_{r=1}^{k} z^*(t - \tau_r) \prod_{s=k+1}^{2k+1} z(t - \tau_s) \, d\boldsymbol{\tau}_{2k+1}.$$

The n-variate complex-valued functions $f(\boldsymbol{\tau}_{2k+1})$ are the Volterra kernels of the baseband-equivalent system in Fig. 2.4b. A physical PA must exhibit a fading memory effect, i.e., its output cannot depend on the infinite past. This, coupled with the requirement of causality, limits the domain of integration in (2.4) from $\mathbb{R}^{2k+1}$ to $[0, T]^{2k+1}$, where T represents the maximum memory span of the PA. If the band-limited output signal is sampled at a sufficiently high rate, i.e., F_s, the relation between the discrete-time baseband input and output becomes [31]

$$y[n] = \sum_{k=0}^{\infty} \sum_{l_1=0}^{M} \cdots \sum_{l_k=l_{k-1}}^{M} \sum_{l_{k+1}=0}^{M} \cdots \sum_{l_{2k+1}=l_{2k}}^{M} f[\boldsymbol{l}_{2k+1}] \prod_{r=1}^{k} z^*[n - l_r] \prod_{s=k+1}^{2k+1} z[n - l_s], \qquad (2.5)$$

where $M = \lceil T/T_s \rceil$, $T_s = 1/F_s$, $\boldsymbol{l}_{2k+1} = [l_1, \ldots, l_{2k+1}]^T$, $f[\boldsymbol{l}_{2k+1}] = f(\boldsymbol{\tau}_{2k+1}T_s)$, $z[n] = z(nT_s)$, and $y[n] = y(nT_s)$.

The expression in (2.5) is the general Volterra-series representation of the baseband PA output $y[n]$ in terms of the baseband input $z[n]$. The general form depicted in (2.5) is of little practical value, and a simplified finitely-parameterized representation is needed for modeling purposes. Over the past two decades, many empirical models have been developed. The simplest of which is the memory polynomial (MP) model [32]

$$y[n] = \sum_{p=0}^{P-1} \sum_{m=0}^{M} a_{pm} \, z[n - m] \, \big| z[n - m] \big|^p. \qquad (2.6)$$

This model can be obtained from the general one in (2.5) by limiting the maximum nonlinearity order to P, setting $l_r = m \ \forall \, r \in \{1, \ldots, 2k + 1\}$, and writing the baseband Volterra kernels in the form of coefficients.

Theoretically speaking, the summation over p in (2.6) should only be over even indices. This is because the product of k conjugated terms $z^*[n - m]$ and $k + 1$ non-conjugated terms $z[n - m]$ results in $z[n - m]|z[n - m]|^{2k}$. Terms with odd p indices in (2.6) cannot be obtained from the general model in (2.5). Nevertheless, empirical fitting of the input-output relationship of most PAs to the model in (2.6) yields non-negligible values for the coefficients corresponding to odd-indexed terms. The explanation for this is that the general model in (2.5) was formulated under somewhat restrictive assumptions and hence, does not describe the exact input-output relationship of a physical PA. By including odd p indices in (2.6), a richer basis set is obtained and the model accuracy is improved [33].

Synthesizing the Predistorter

The basic principle behind DPD is to apply a nonlinear function to the input signal so that the tandem connection of the DPD module and the nonlinear PA approximates an ideal linear PA (see Fig. 2.5). In general, the DPD output is a weighted sum of nonlinear functions of the input signal samples

$$z[n] = \sum_{i=1}^{P} w_i \phi_i(\mathbf{x}[n]), \tag{2.7}$$

where $\mathbf{x}[n] = [x[n], \ldots, x[n-M]]$ is a row vector containing the current and previous M input samples, M is the model memory depth, $\phi_1(.), \ldots, \phi_P(.)$ are the basis functions, and $w_1, \ldots, w_P$ are the DPD coefficients.
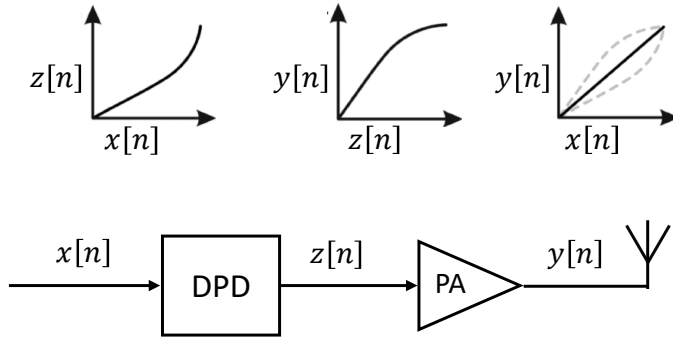
Figure 2.5: The basic theory behind DPD.

The expression in (2.7) is a Volterra-series representation of the DPD module, with the functions $w_1\phi_1(.), \ldots, w_P\phi_P(.)$ representing its Volterra operators. The composite system formed by the tandem connection of the DPD module and PA can also be expressed in terms of a Volterra series with, in general, infinitely many operators. The pth-order inverse theory in [34] states that the DPD operators can be synthesized in a way that ensures all nonlinear operators of the composite system up to the pth-order are zero. The synthesized DPD operators, using the method in [34], are composite functions of the PA operators. Since the PA operators in (2.5) form a closed set under composition, the composed DPD operators are of the same form as the PA operators. Therefore, the predistorter in (2.7) should have the same form as the Volterra-based PA model in (2.5), with $y[n]$ and $z[n]$ replaced by $z[n]$ and $x[n]$ respectively. Obviously, pruned versions of this general model are needed for practical DPD implementations. The MP model in (2.6), or the more advanced models in the literature (e.g., [35–38]) can be utilized.

The predistorter in (2.7) can be directly synthesized from the feedback signal, without the need for explicitly identifying the PA Volterra operators. The DPD basis functions are selected beforehand and the coefficients are updated iteratively, using Newton's method, until convergence is observed. The adaptation algorithm in [39, 40] is derived below.

The objective of the DPD module is to make the PA output be as close as possible to a scaled version of the original input signal, i.e., $y[n] \approx G x[n]$ where G is the desired gain. The maximum value of G that can be chosen is set by the saturation limit of either the PA or the DAC(s). The DPD coefficients are those that minimize the following cost function

$$J(\mathbf{w}) = \frac{1}{N-M} \sum_{n=M}^{N-1} \left(\frac{y[n]}{G} - x[n] \right) \left(\frac{y[n]}{G} - x[n] \right)^*, \qquad (2.8)$$

where $\mathbf{w} = [w_1, \ldots, w_P]^T$ is the vector of coefficients and N is the number of input samples. Notice that the first M samples have been omitted to avoid the boundary effect. In order to derive the update equation, a suitable model for the PA is needed. Since most PAs are only weakly nonlinear, a simple PA model is [40]

$$y[n] \approx h_0 z[n] + \eta[n], \qquad (2.9)$$

where h_0 is a complex-valued constant and $\eta[n]$ represents the higher-order nonlinear distortion, which is assumed to be uncorrelated with $z[n]$. This model may seem rather crude; for if the PA nonlinearity were negligible, no linearization would be needed. Such simple model, however, makes the DPD update equation independent of the specific PA nonlinearity and significantly reduces training complexity. Furthermore, the training process is iterative and the DPD coefficients should converge to, at least, a sub-optimal solution with enough iterations. With this model, the cost function becomes linear in $\mathbf{w}$, and the Newton's update equation for a real-valued cost function with complex-valued arguments simplifies to [41]

$$\mathbf{w}^l \approx \mathbf{w}^{l-1} - \mu \left[\left(\frac{\partial^2 J}{\partial \mathbf{w}^* \partial \mathbf{w}^T} \right)^{-1} \left(\frac{\partial J}{\partial \mathbf{w}} \right)^* \right]_{\mathbf{w}=\mathbf{w}^{l-1}}, \qquad (2.10)$$

where $\mathbf{w}^l$ denotes the coefficients vector after the lth iteration and $\mu \in (0, 1]$ is the step size. The respective elements of the $P \times 1$ vector $\frac{\partial J}{\partial \mathbf{w}}$ and the $P \times P$ matrix $\frac{\partial^2 J}{\partial \mathbf{w}^* \partial \mathbf{w}^T}$ are

$$\left[\frac{\partial J}{\partial \mathbf{w}} \right]_j = \frac{\partial J}{\partial w_j}, \qquad \left[\frac{\partial^2 J}{\partial \mathbf{w}^* \partial \mathbf{w}^T} \right]_{ij} = \frac{\partial^2 J}{\partial w_i^* \partial w_j}. \qquad (2.11)$$

The derivatives above are Wirtinger derivatives. That is, when differentiating with respect to w_i, w_i^* is regarded as a constant, and vice versa [41]. Substituting (2.7) and

(2.9) into (2.8) and differentiating gives

$$\frac{\partial J}{\partial w_j} = \frac{1}{N-M} \sum_{n=M}^{N-1} \left(\frac{y[n]}{G} - x[n]\right)^* \frac{h_0}{G} \phi_j(\underline{\mathbf{x}}[n]) \tag{2.12}$$

$$\frac{\partial^2 J}{\partial w_i^* \partial w_j} = \frac{1}{N-M} \sum_{n=M}^{N-1} \left|\frac{h_0}{G}\right|^2 \phi_i^*(\underline{\mathbf{x}}[n]) \phi_j(\underline{\mathbf{x}}[n]). \tag{2.13}$$

Substituting (2.12) and (2.13) into (2.10) and rewriting the result in matrix form yields the following update equation [39, 40]

$$\mathbf{w}^l = \mathbf{w}^{l-1} - \mu \frac{G}{h_0} \left(\mathbf{\Phi}^H \mathbf{\Phi}\right)^{-1} \mathbf{\Phi}^H \left(\frac{\mathbf{y}}{G} - \mathbf{x}\right), \tag{2.14}$$

where $\mathbf{x} = [x[M], \dots, x[N-1]]^T$ and $\mathbf{y} = [y[M], \dots, y[N-1]]^T$ are the input and output vectors respectively, and

$$\mathbf{\Phi} = \begin{bmatrix} \phi_1(\underline{\mathbf{x}}[M]) & \dots & \phi_P(\underline{\mathbf{x}}[M]) \\ \vdots & & \vdots \\ \phi_1(\underline{\mathbf{x}}[N-1]) & \dots & \phi_P(\underline{\mathbf{x}}[N-1]) \end{bmatrix}.$$

In practice, the feedback signal exhibits delay and phase offsets from the transmitted one due to propagation delay and imperfect synchronization. These offsets must be compensated for in order for the DPD iterations to converge reliably. Let $g[n], n = 0, \dots, S-1$ be the S baseband samples captured by the TOR. Without loss of generality, we assume that $S > N$. In Appendix A, we show that the maximum-likelihood (ML) estimates of the delay, amplifier gain, and phase offset (d_0, h_0, and θ respectively) are given by [1]

$$\hat{d}_0 = \underset{d \in [0, S-N]}{\operatorname{argmax}} \left|\mathbf{z}^H \mathbf{g}(d)\right| \tag{2.15}$$

$$\hat{h}_0 e^{j\hat{\theta}} = \left(\mathbf{z}^H \mathbf{z}\right)^{-1} \mathbf{z}^H \mathbf{g}(\hat{d}_0), \tag{2.16}$$

where $\mathbf{z} = [z[0], \dots, z[N-1]]^T$ and $\mathbf{g}(d) = [g[d], \dots, g[d+N-1]]^T$. Note that in (2.16), θ is the combined phase offset due to transmitter circuitry and imperfect synchronization. This forces the estimate of the amplifier gain (i.e., $\hat{h}_0$) to be a positive real value. The delay-compensated output vector is then $\mathbf{y} = [g[\hat{d}_0 + M], \dots, g[\hat{d}_0 + N-1]]^T$, and the modified update equation becomes

$$\mathbf{w}^l = \mathbf{w}^{l-1} - \tau \left(\mathbf{\Phi}^H \mathbf{\Phi}\right)^{-1} \mathbf{\Phi}^H \left(\frac{\mathbf{y}}{G} e^{-j\hat{\theta}} - \mathbf{x}\right), \tag{2.17}$$

---

[1]While these expressions seem intuitive, we could not find a formal derivation in related literature.

where $\tau = \mu G / \hat{h}_0$. It is customary to select the first basis function to be the input itself, i.e., $\phi_1(\underline{\mathbf{x}}[n]) = x[n]$. Hence, a good initial estimate of the DPD coefficients vector is $\mathbf{w}^0 = [G/\hat{h}_0, 0, \ldots, 0]^T$.

Finally, we note that the matrix inversion required in (2.17) is ill-conditioned. This is because $x[n]$ is an up-sampled version of the information-bearing signal, which means that the input samples to the DPD block are linearly dependent. Consequently, the use of bases of the form $\phi_i(\underline{\mathbf{x}}[n]) = x[n - l_i]$, which are needed to compensate for the PA's linear frequency response [35], increases the condition number of $\mathbf{\Phi}$. A simple solution to this problem is to utilize diagonal regularization (or ridge regression), i.e., the matrix inversion is regularized by a very small positive constant λ, so that it becomes $\left(\mathbf{\Phi}^H \mathbf{\Phi} + \lambda \mathbf{I}_K \right)^{-1}$ [42]. This form of regularization allows for efficiently updating $\mathbf{w}$ using the well-known recursive least-squares (RLS) algorithm (thereby, circumventing the need for explicit matrix inversion), and has the added benefit of decreasing the 2-norm of $\mathbf{w}$ [42].

The Standard TOR Architecture

(a) Direct-conversion (zero IF).

(b) Two-stage conversion (non-zero IF).
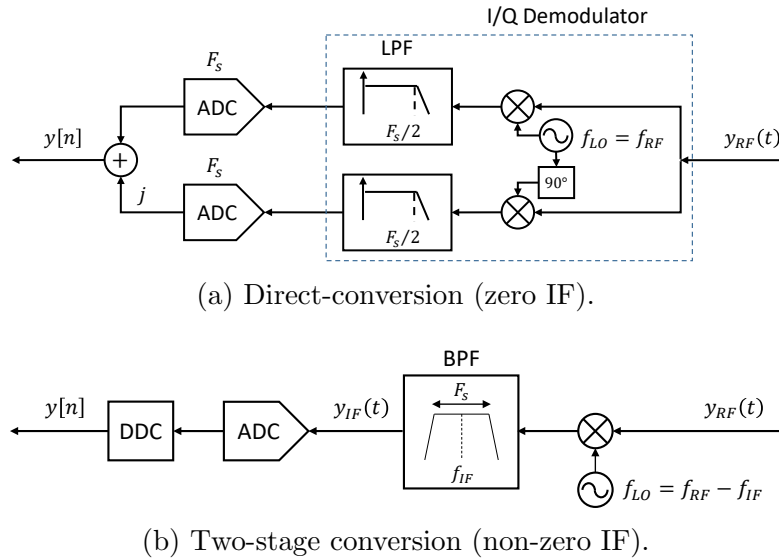
Figure 2.6: The two conventional TOR architectures.

As shown in Fig. 2.4a, training the DPD module requires a dedicated TOR that captures the transmitted signal and feeds it back to the baseband processing unit. Fig. 2.6 shows the block diagrams of the two conventional TOR architectures. The first is the

direct-conversion (or zero-IF) architecture, in which an I/Q demodulator down-converts the feedback signal to baseband and the baseband signal is sampled by two Nyquist-rate analog-to-digital converter (ADC)s (i.e., $F_{\text{ADC}} \geq F_s$). The second architecture is the non-zero-IF one, in which a high-speed ADC captures the feedback signal and a digital down-conversion (DDC) unit down-converts it to baseband. Proper DDC on the pass-band feedback signal $y_{IF}[n]$ requires that $f_{IF} \geq F_s/2$ and $F_{\text{ADC}} \geq 2(f_{IF} + F_s/2)/n$, where $n = \lfloor (f_{IF} + F_s/2)/F_s \rfloor$ [43]. The lowest possible ADC sampling rate for which DDC is possible is $2F_s$ and this can be achieved by choosing $f_{IF} = mF_s/2$, where m is any non-zero integer. The first architecture is less demanding in terms of the ADC speed required, but is prone to I/Q imbalance (due to mismatches in the conversion gains of the quadrature mixer branches and/or deviation from the ideal 90° phase shift).

Performance Metrics

The quality of the PA output signal is often assessed through the evaluation of two performance metrics. The first is the root normalized mean-square error (RNMSE), which measures the discrepancy between the baseband input signal $x[n]$ and the captured feedback signal $y[n]$, i.e.,

$$\text{RNMSE} = 100 \times \sqrt{\frac{\sum_{n=0}^{N-1} \left| y[n] - \alpha\, x[n] \right|^2}{\sum_{n=0}^{N-1} \left| \alpha\, x[n] \right|^2}} \quad \%, \tag{2.18}$$

where α is the least-squares (LS) estimate of the complex-valued channel gain, i.e.,

$$\alpha = \frac{\sum_{n=0}^{N-1} x^*[n] y[n]}{\sum_{n=0}^{N-1} \left| x[n] \right|^2}.$$

The second is the adjacent-channel power ratio (ACPR), which is the ratio of the output power in the adjacent frequency band F_{adj} to that in the desired band F_{ch}, i.e.,

$$\text{ACPR} = 10 \log_{10} \left(\frac{\int_{F_{\text{adj}}} \Phi_y(f)\, df}{\int_{F_{\text{ch}}} \Phi_y(f)\, df} \right) \quad \text{dB}, \tag{2.19}$$

where $\Phi_y(f)$ is the estimated power spectral density of $y[n]$. An example to demonstrate the evaluation of the ACPR metric is shown in Fig. 2.7, which depicts the normalized output spectrum of an 8-Watt Doherty PA. Here, the center frequency is 3.5 GHz and the channel bandwidth is 100 MHz, including a guard-band of 0.845 MHz on each side [44].

Thus, the desired band is $F_{ch} = \{f : f \in [3.450845, 3.549155]\,\text{GHz}\}$ and the lower/upper bands at $\mp$ 100-MHz offsets are $F_{adj,L} = \{f : f \in [3.350845, 3.449155]\,\text{GHz}\}$ and $F_{adj,U} = \{f : f \in [3.550845, 3.649155]\,\text{GHz}\}$ respectively. The lower/upper ACPRs before and after DPD are $-33.5/-30.5$ and $-58.6/-58.1$ respectively.
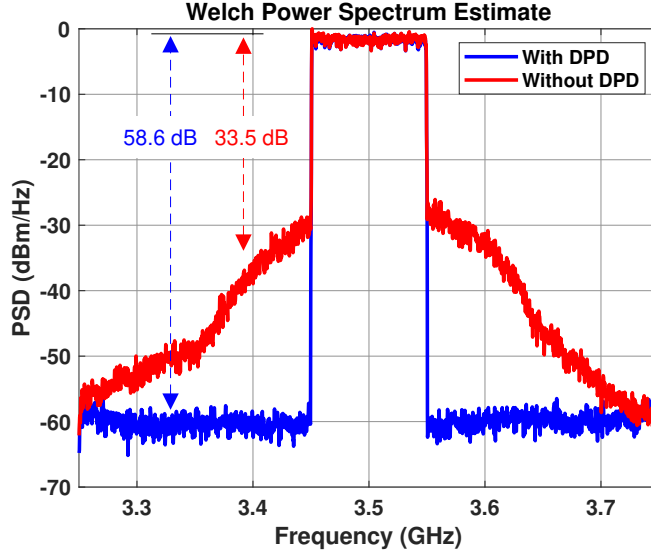
Figure 2.7: The normalized spectrum of an 8-Watt Doherty PA with and without DPD.

2.2.2 Modeling the Behavior of PAs under Crosstalk

As was the case with the SISO model in Section 2.2.1, the MIMO system model is formulated in baseband-equivalent form. Fig. 2.8 shows the incident and reflected waves in a multi-antenna transmitter system with K parallel paths. Let $a_{1k}[n]$ denote the incident voltage wave at the input of the kth PA. This signal is amplified by the PA and results in an output voltage wave $b_{2k}[n]$ that is directed towards the kth antenna. A well-designed antenna emits most of this incident energy into space towards a far-field receiver. Inevitably, however, a portion of this energy is reflected back towards the PA and other portions are picked up by the neighboring $K - 1$ antennas that are in close proximity. The incident wave on the output port of the kth PA, denoted by $a_{2k}[n]$, is comprised of the reflected wave from the kth antenna plus the coupled waves from the neighboring $K - 1$ antennas [45]

$$a_{2k}[n] = \sum_{i=1}^{K} \sum_{q=0}^{Q-1} \lambda_{ki}[q] b_{2i}[n-q], \tag{2.20}$$

17
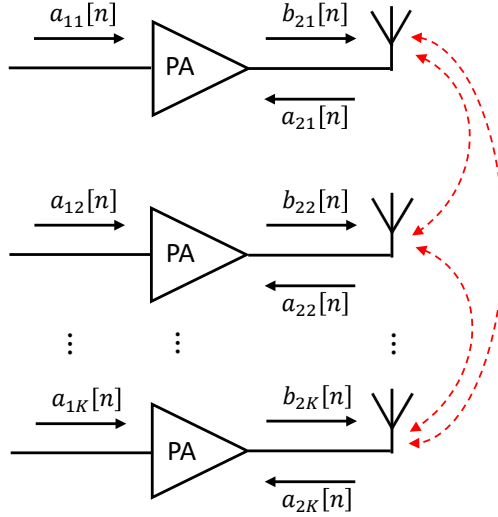
Figure 2.8: The incident and reflected waves in a multi-antenna system with K chains.

where $\lambda_{ki}[0], \ldots, \lambda_{ki}[Q-1]$ are the coefficients of the finite impulse response (FIR) filter that characterizes the coupling from the ith to the kth path. The time-domain FIR filters in (2.20) can be extracted from the antenna array scattering parameters (S-parameters) as follows. Given the S-parameters at a finite set of frequencies within the desired bandwidth $\{f_1, \ldots, f_L\} \in [f_{RF} - F_s/2, f_{RF} + F_s/2]$, the Q-tap filter $\boldsymbol{\lambda}_{ki}$ is the LS solution to

$$\mathbf{F}\boldsymbol{\lambda}_{ki} = \mathbf{s}_{ki}, \tag{2.21}$$

where

$$\boldsymbol{\lambda}_{ki} = \begin{bmatrix} \lambda_{ki}[0] & \ldots & \lambda_{ki}[Q-1] \end{bmatrix}^T$$

$$\mathbf{s}_{ki} = \begin{bmatrix} S_{ki}(f_1) & \ldots & S_{ki}(f_L) \end{bmatrix}^T$$

$$\mathbf{F} = \begin{bmatrix} 1 & e^{-j2\pi f_1'} & \ldots & e^{-j2\pi f_1'(Q-1)} \\ 1 & e^{-j2\pi f_2'} & \ldots & e^{-j2\pi f_2'(Q-1)} \\ \vdots & \vdots & \ddots & \vdots \\ 1 & e^{-j2\pi f_L'} & \ldots & e^{-j2\pi f_L'(Q-1)} \end{bmatrix},$$

and $f_i' = (f_i - f_{RF})/F_s, i = 1, \ldots, L$.

The output signal of the kth PA $b_{2k}[n]$ depends not only on its input $a_{1k}[n]$, but also on the incident wave on its output port $a_{2k}[n]$ [26]. Therefore, the behaviour of each PA in the array can be described by a dual-input single-output (DISO) Volterra series. The DISO

models in [10–12] are based on the assumption that $a_{2k}[n]$ is relatively small in magnitude and hence, $|a_{2k}[n]|^p \approx 0 \,\forall\, p > 1$. This assumption significantly simplifies the general DISO model, as only linear terms of $a_{2k}[n]$ need to be considered. The simplified model reads [11]

$$
\begin{aligned}
b_{2k}[n] &= \sum_{i=0}^{\infty}\sum_{l_1=0}^{M}\cdots\sum_{l_i=l_{i-1}}^{M}\sum_{l_{i+1}=0}^{M}\cdots\sum_{l_{2i+1}=l_{2i}}^{M} f[\boldsymbol{l}_{2i+1}]\prod_{r=1}^{i}a_{1k}^{*}[n-l_r]\prod_{s=i+1}^{2i+1}a_{1k}[n-l_s] \\
&+\sum_{i=0}^{\infty}\sum_{p_1=0}^{M}\sum_{p_2=0}^{M}\cdots\sum_{p_{i+1}=p_i}^{M}\sum_{p_{i+2}=0}^{M}\cdots\sum_{p_{2i+1}=p_{2i}}^{M} g[\boldsymbol{p}_{2i+1}]a_{2k}[n-p_1]\prod_{u=2}^{i+1}a_{1k}^{*}[n-p_u] \\
&\qquad\qquad\qquad\qquad\qquad\qquad\qquad\qquad\times\prod_{v=i+2}^{2i+1}a_{1k}[n-p_v] \\
&+\sum_{i=1}^{\infty}\sum_{q_1=0}^{M}\sum_{q_2=0}^{M}\cdots\sum_{q_i=q_{i-1}}^{M}\sum_{q_{i+1}=0}^{M}\cdots\sum_{q_{2i+1}=q_{2i}}^{M} h[\boldsymbol{q}_{2i+1}]a_{2k}^{*}[n-q_1]\prod_{a=2}^{i}a_{1k}^{*}[n-q_a] \\
&\qquad\qquad\qquad\qquad\qquad\qquad\qquad\qquad\times\prod_{c=i+1}^{2i+1}a_{1k}[n-q_c], \qquad\qquad (2.22)
\end{aligned}
$$

where $\boldsymbol{l}_{2ik+1} = [l_1,\ldots,l_{2i+1}]^T$, $\boldsymbol{p}_{2i+1} = [p_1,\ldots,p_{2i+1}]^T$, and $\boldsymbol{q}_{2i+1} = [q_1,\ldots,q_{2i+1}]^T$. This model can be considered as a generalization of the well-known polyharmonic distortion (PHD) models in [46, 47]. Like the general SISO model in (2.5), the above model is only of theoretical value. Pruned versions of (2.22) were proposed in [10–12]. These models are dual-input extensions of the SISO MP model in (2.6). For instance, the pruned DISO model in [11] is given by

$$
\begin{aligned}
b_{2k}[n] &= \sum_{p=0}^{P_1-1}\sum_{m=0}^{M_1}\alpha_{pm}a_{1k}[n-m]\left|a_{1k}[n-m]\right|^p \\
&+\sum_{p=0}^{P_2-1}\sum_{m_1=0}^{M_2}\sum_{m_2=0}^{M_3}\beta_{pm_1m_2}a_{2k}[n-m_1]\left|a_{1k}[n-m_2]\right|^p \\
&+\sum_{p=0}^{P_3-3}\sum_{m_1=0}^{M_4}\sum_{m_2=0}^{M_5}\gamma_{pm_1m_2}a_{2k}^{*}[n-m_1]a_{1k}^{2}[n-m_2]\left|a_{1k}[n-m_2]\right|^p. \qquad (2.23)
\end{aligned}
$$

The models in [10–12] were experimentally verified, using active load-pull measurements [48–50], to be of remarkable accuracy. The authors of [11] showed that the more complex models in [51, 52], which take higher-order effects of $a_{2k}[n]$ into account, yield no appreciable improvement in modeling accuracy over that obtained with the model in (2.23).

2.2.3 The Dual-input DPD Architecture

As explained in the previous subsection, the behavior of each PA in the array is affected by the incident wave on its output port, which in turn is a function of all input signals to the array. If the antennas are spaced far enough, the contribution from the neighboring paths can be neglected and the only significant constituent of $a_{2k}[n]$ is that due to $b_{2k}[n]$, i.e., each PA sees only the reflection of its own output signal. In that case, $b_{2k}[n]$ can be expressed as a function of $a_{1k}[n]$, and employing conventional SISO DPD in each path becomes sufficient [53]. In reality, however, a highly integrated design that places all chains closely together is advantageous in terms of cost and reliability. Hence, antenna crosstalk cannot be neglected in practice.
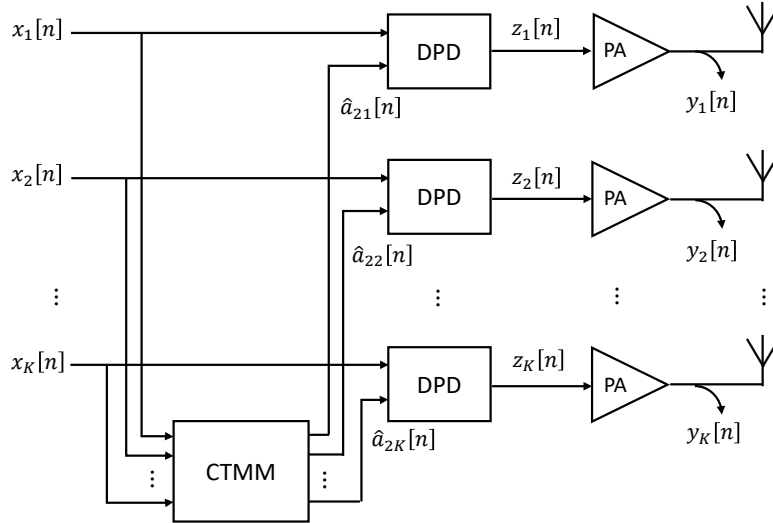
Figure 2.9: A fully digital MIMO system that employs a dual-input DPD architecture [13].

Recently, the authors of [13] proposed a DPD architecture that accounts for the antenna crosstalk in MIMO systems. Fig. 2.9 shows a K-path fully digital MIMO system with DISO DPD modules employed in each path. This figure is in baseband-equivalent form, as was Fig. 2.4b. The kth DPD output constitutes the incident input wave on the kth PA, i.e., $a_{1k}[n] = z_k[n]$. The kth DPD module takes two inputs: the first is $x_k[n]$ and the second is $\hat{a}_{2k}[n]$, which is an estimate of the incident wave at the kth PA output. It is natural to expect that the DPD model has the same form as the simplified DISO PA model in

(2.23) [13], i.e.,

$$z_k[n] = \sum_{p=0}^{P_1-1} \sum_{m=0}^{M_1} \eta_{pm} x_k[n-m] \left| x_k[n-m] \right|^p$$
$$+ \sum_{p=0}^{P_2-1} \sum_{m_1=0}^{M_2} \sum_{m_2=0}^{M_3} \mu_{pm_1m_2} \hat{a}_{2k}[n-m_1] \left| x_k[n-m_2] \right|^p$$
$$+ \sum_{p=0}^{P_3-3} \sum_{m_1=0}^{M_4} \sum_{m_2=0}^{M_5} \epsilon_{pm_1m_2} \hat{a}_{2k}^*[n-m_1] x_k^2[n-m_2] \left| x_k[n-m_2] \right|^p. \qquad (2.24)$$

The incident waves at the PAs' outputs (referred to as the crosstalk and mismatch (CTMM) signals henceforth) can be estimated from the K input signals if the following approximation is made: $b_{2k}[n] \approx G x_k[n] \, \forall k$ where G is desired PA gain. In essence, this approximation is equivalent to assuming that the DPD modules are able to compensate for all distortions. The CTMM signals are estimated by introducing this approximation in (2.20) [13]

$$\hat{a}_{2k}[n] = \sum_{i=1}^{K} \sum_{q=0}^{Q-1} \lambda'_{ki}[q] x_k[n-q], \qquad (2.25)$$

where $\lambda'_{ki}[q] = G\lambda_{ki}[q]$. The DPD module in each path is trained using the conventional training process described in Section 2.2.1, with the extension that the DPD bases are now dual-input functions. The output of each PA is captured using a dedicated TOR and the feedback signals $y_1[n], \ldots, y_K[n]$ are used to train the DPD modules. The feedback signals are scaled versions of the PAs' output waves, i.e., $y_k[n] = \gamma \, b_{2k}[n]$.

The authors of [54] demonstrated that this dual-input architecture is also applicable in hybrid beamforming systems. In a hybrid beamforming system, such as that depicted in Fig. 2.2, the antenna array is divided into a number of subarrays with each subarray having one digital input. The input to each subarray is split into multiple paths with different phase shifts, before being amplified and transmitted through the antennas. By treating each subarray as one large PA [55–60], the hybrid beamforming system reduces to a digital one and the DPD architecture described above becomes applicable, as shown in Fig. 2.10.

Finally, we note that the formulation presented above is based on the assumption that inter-path coupling occurs only after the PAs (due to antenna crosstalk). If significant inter-path coupling occurs before the PAs, the input signal to the kth PA (i.e., $a_{1k}[n]$) would no longer be $z_k[n]$, but rather a linear combination of the outputs of all DPD modules. This would introduce significant distortions that can only be compensated with

a high-complexity multi-input DPD module in each path [61–65]. In practice, inter-path coupling before the PAs is indeed negligible and the dual-input DPD architecture proposed in [13] is effective at eliminating nonlinear distortions.
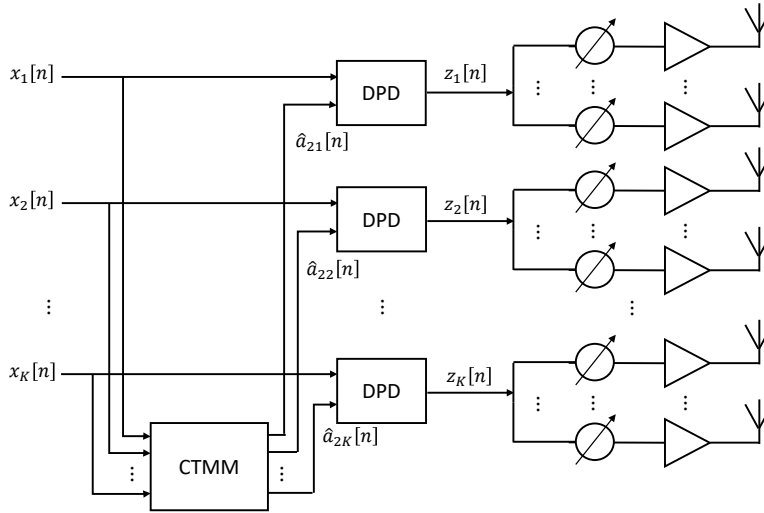
Figure 2.10: A hybrid MIMO system that employs a dual-input DPD architecture [54].

2.3 Downlink Precoding

2.3.1 System Model

One of the main DSP functions in a massive MIMO system is precoding. On the downlink, the basestation precodes the users' signals prior to transmission to counteract multi-user channel effects and ensure negligible interference levels at the user terminals. For this to be possible, the basestation must acquire the channel state information (CSI) beforehand. In this work, we assume the availability of CSI at the basestation and focus on the precoding problem. We only consider linear precoding schemes, in which the users' signals are multiplied by a precoding matrix. The precoding matrix can be chosen according to different criteria, as will be explained in the next subsection. Although more complex nonlinear precoding schemes can offer better performance [66], they are generally unfavorable as they require special processing at the receivers' side. In addition, the spectral efficiency attained with linear precoding schemes is close to that achieved with nonlinear ones, especially when the number of antennas is large [66].

In a narrowband single-carrier system, the free-space downlink channel can be considered frequency-independent. Hence, it can be represented as an $L \times K$ matrix $\mathbf{H}$, where $(\mathbf{H})_{l,k} = H_{l,k}$ represents the channel coefficient between the kth basestation antenna and the antenna of the lth user. Fig. 2.11 depicts the baseband-equivalent model of Fig. 2.1a in a single-carrier scenario. As in Fig. 2.1a, we omit the DSP modules that address hardware limitations for simplicity.
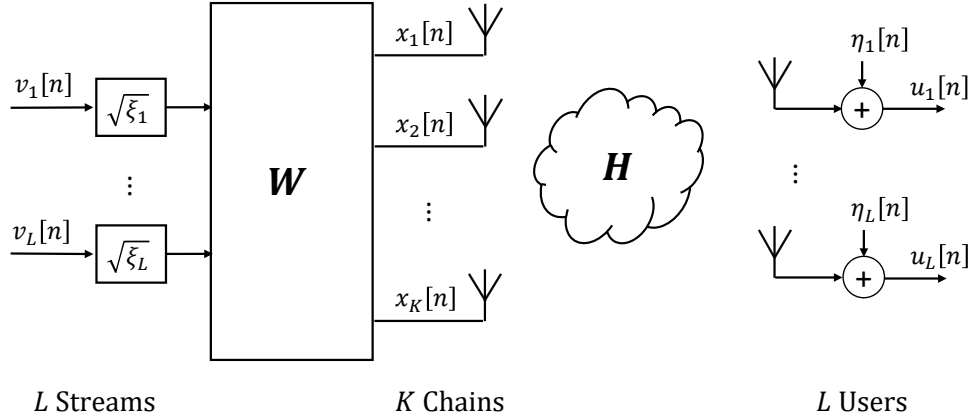
Figure 2.11: Linear precoding in a narrowband single-carrier system.

Let $\mathbf{v}[n] = [v_1[n], \ldots, v_L[n]]^T$ be the vector of user signal samples at the nth time instant. Without loss of generality, we assume that $\mathbb{E}[\mathbf{v}[\mathbf{n}]] = \mathbf{0}_{L \times 1}$ and $\mathbb{E}[\mathbf{v}[n]\mathbf{v}^H[n]] = \mathbf{I}_L$, i.e., the users' signals are uncorrelated and normalized to be of unit power each. The data streams are multiplied by the power control coefficients $\sqrt{\xi_1}, \ldots, \sqrt{\xi_L}$, which can be used to prioritize certain users over others, and the resultant $L \times 1$ vector is then multiplied by the $K \times L$ precoding matrix $\mathbf{W}$ to yield the $K \times 1$ vector of precoded signals

$$\mathbf{x}[n] = \mathbf{W}\boldsymbol{\Xi}^{\frac{1}{2}}\mathbf{v}[n], \tag{2.26}$$

where $\boldsymbol{\Xi} = \mathrm{diag}([\xi_1, \ldots, \xi_L])$. The average power transmitted by the kth chain is

$$P_k = \mathbb{E}\left[\left|\mathbf{e}_k^T\mathbf{W}\boldsymbol{\Xi}^{\frac{1}{2}}\mathbf{v}[n]\right|^2\right] = \mathbf{e}_k^T\mathbf{W}\,\boldsymbol{\Xi}\,\mathbf{W}^H\mathbf{e}_k = \underline{\mathbf{w}}_k\boldsymbol{\Xi}\underline{\mathbf{w}}_k^H = \sum_{l=1}^{L}\xi_l|W_{k,l}|^2, \tag{2.27}$$

where $\mathbf{e}_k$ is a $K \times 1$ unit vector with a one in the kth position and zeros in all other positions, and $\underline{\mathbf{w}}_k$ denotes the kth row of $\mathbf{W}$.

The received signals at the users' side can be arranged in an $L \times 1$ vector $\mathbf{u}[n] = [u_1[n], \ldots, u_L[n]]^T$. Assuming ideal transmitting and receiving hardware, this vector is

given by

$$\mathbf{u}[n] = \mathbf{HW\Xi}^{\frac{1}{2}}\mathbf{v}[n] + \boldsymbol{\eta}[n], \qquad (2.28)$$

where $\boldsymbol{\eta}[n]$ is an $L \times 1$ vector of circularly-symmetric zero-mean additive white Gaussian noise (AWGN) samples with variance σ^2, i.e., $\mathbb{E}\left[\boldsymbol{\eta}[n]\boldsymbol{\eta}^H[n]\right] = \sigma^2\mathbf{I}_L$.

In a wideband multi-carrier system, the channel cannot be assumed frequency-flat. The basestation then needs to estimate N channel matrices $\mathbf{H}_1, \ldots, \mathbf{H}_N$, where N is the number of subcarriers. Accordingly, N precoding matrices $\mathbf{W}_1, \ldots, \mathbf{W}_N$ (one for each subcarrier) are necessary. For reference, the conventional precoding configuration in an orthogonal frequency-division multiplexing (OFDM) system is depicted in Fig. 2.12.
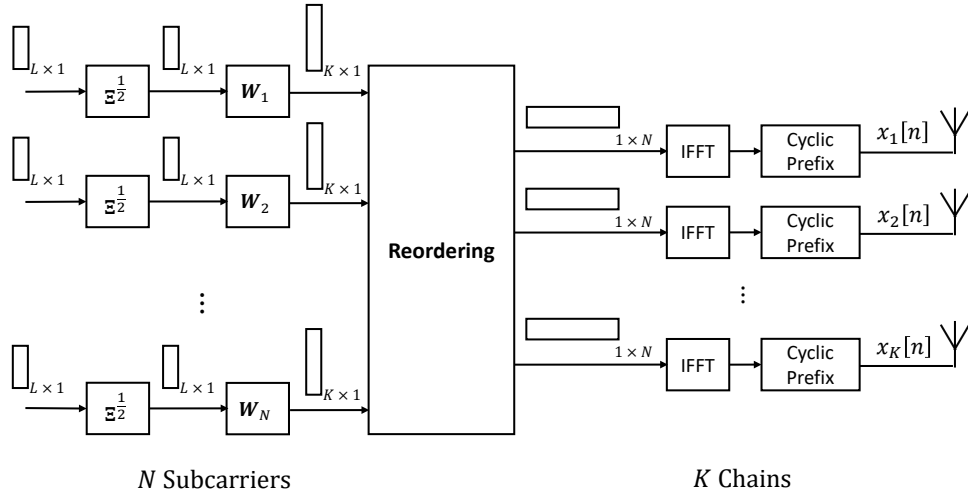
Figure 2.12: Linear Precoding in a MIMO-OFDM system.

2.3.2 Conventional Linear Precoders

In this work, we assume that the power control matrix $\mathbf{\Xi}$ is pre-determined and that the purpose of the precoder, $\mathbf{W}$, is to mitigate channel variations. In this scenario, the basestation updates the channel estimate $\hat{\mathbf{H}}$ every coherence interval (usually between 1 to 10 milliseconds [67]) and calculates the precoder accordingly (i.e., $\mathbf{W} = \mathbf{f}(\hat{\mathbf{H}})$), so that each user is provided with a consistent quality of service [6]. Many works (e.g., [68–73]) combine these matrices into one and perform a joint optimization to maximize a certain performance metric across all users (e.g., the sum spectral efficiency). The approaches therein vary the relative powers delivered to the users according to the instantaneous estimated channel,

which makes them inapplicable in the scenario assumed here. Below, we describe the three conventional linear precoding methods (namely, maximum-ratio transmission (MRT), zero-forcing (ZF), and minimum mean-square error (MMSE)) [74]. To simplify the notation below, the estimated channel matrix at the basestation $\hat{\mathbf{H}}$ is denoted simply as $\mathbf{H}$.

Maximum-Ratio Transmission

The MRT precoder amplifies the signal of interest at each user while disregarding inter-user interference. This is desirable when the noise power at the user terminals is comparable with the received power from the basestation. Given that the transmission coefficient of the desired signal component at the lth user is $(\mathbf{HW})_{l,l}$, the conventional MRT precoder minimizes the total transmit power needed to ensure that $(\mathbf{HW})_{l,l} = 1 \ \forall l \in \{1, \dots, L\}$, i.e.,

$$\mathbf{W}_{\mathrm{MRT}} = \underset{\mathbf{W} \in \mathbb{C}^{K \times L}}{\operatorname{argmin}} \sum_{k=1}^{K} P_k \qquad \text{s.t. } (\mathbf{HW})_{l,l} = 1 \quad \forall l. \tag{2.29}$$

Using the Cauchy-Schwarz inequality [75], it can be shown that the solution to this optimization problem is

$$\mathbf{W}_{\mathrm{MRT}} = \mathbf{H}^H \operatorname{diag}\left(\left[1/\|\underline{\mathbf{h}}_1\|^2, \dots, 1/\|\underline{\mathbf{h}}_L\|^2\right]\right), \tag{2.30}$$

where $\underline{\mathbf{h}}_l$ denotes the lth row of $\mathbf{H}$.

Zero-Forcing

On the other hand, ZF precoding suppresses inter-user interference while not necessarily maximizing the desired signal components at the users. This is because part of the available transmit power is used to nullify inter-user interference, which is achieved by enforcing the condition $\mathbf{HW} = \mathbf{I}_L$. Since $L < K$, an infinite number of matrices satisfy this condition. The conventional ZF precoder is that which minimizes the total transmit power, i.e.,

$$\mathbf{W}_{\mathrm{ZF}} = \underset{\mathbf{W} \in \mathbb{C}^{K \times L}}{\operatorname{argmin}} \sum_{k=1}^{K} P_k \qquad \text{s.t. } \mathbf{HW} = \mathbf{I}_L. \tag{2.31}$$

The solution to this problem is $\mathbf{W}_{\mathrm{ZF}} = \mathbf{H}^\dagger$ [75]. If $\mathbf{H}$ has full rank, which is almost surely true since its elements are drawn from a continuous distribution, the solution simplifies to the well-known formula

$$\mathbf{W}_{\mathrm{ZF}} = \mathbf{H}^H \left(\mathbf{HH}^H\right)^{-1}. \tag{2.32}$$

MMSE Precoding

Instead of minimizing the total transmit power required to ensure a given performance metric is met (e.g., $\mathbf{HW} = \mathbf{I}_L$), one could fix the transmit power and optimize for performance. In this sense, the MMSE precoder is the one that achieves the optimal trade-off between interference suppression and noise mitigation [74]. In order to maintain the relative quality of service dictated by $\mathbf{\Xi}$, the desired signal component at the lth user should be proportional to the square-root of its allocated power (i.e., $\sqrt{\xi_l}$). Assuming that simple one-tap equalizers are utilized, the mean-square error (MSE) at the lth user is then $\mathbb{E}\left[\left|v_l[n] - (\beta\sqrt{\xi_l})^{-1}u_l[n]\right|^2\right]$, where $\beta \in \mathbb{R}_+$ is a constant to be determined. For a fixed total transmit power P_{tot}, the MMSE precoder is that which minimizes the average MSE across all users, i.e.,

$$\{\mathbf{W}_{\mathrm{MMSE}}, \beta_{\mathrm{MMSE}}\} = \underset{\mathbf{W}\in\mathbb{C}^{K\times L}, \beta\in\mathbb{R}_+}{\operatorname{argmin}} \mathbb{E}\left[\left\|\mathbf{v}[n] - \beta^{-1}\mathbf{\Xi}^{-\frac{1}{2}}\mathbf{u}[n]\right\|^2\right] \quad \text{s.t.} \sum_{k=1}^{K} P_k = P_{tot}. \quad (2.33)$$

The solution to the problem above is [74]

$$\mathbf{W}_{\mathrm{MMSE}} = \beta_{\mathrm{MMSE}}\,\mathbf{H}^H\mathbf{A}, \quad (2.34)$$

where

$$\beta_{\mathrm{MMSE}} = \sqrt{\frac{P_{tot}}{\operatorname{tr}\left(\mathbf{H}^H\mathbf{A}\mathbf{\Xi}\mathbf{A}\mathbf{H}\right)}}$$

$$\mathbf{A} = \left(\mathbf{HH}^H + \frac{\sigma^2\operatorname{tr}(\mathbf{\Xi}^{-1})}{P_{tot}}\mathbf{\Xi}\right)^{-1}.$$

Note that the expression above is slightly different from that in [74] due to the inclusion of the power control matrix $\mathbf{\Xi}$ in the system model. The MMSE precoder can be considered optimal under any signal-to-noise ratio (SNR); it converges to the ZF precoder as $(\sigma^2/P_{tot}) \to 0$ and to the MRT precoder as $(\sigma^2/P_{tot}) \to \infty$ [74]. If $\mathbf{\Xi} = \mathbf{I}_L$, the MMSE precoder can be considered as a special case of the regularized ZF precoder $\mathbf{W}_{\mathrm{RZF}} = \alpha\mathbf{H}^H\left(\mathbf{HH}^H + \lambda\mathbf{I}_L\right)^{-1}$, where α and λ are design parameters that can be heuristically optimized [76].

Chapter 3

Analysis and Mitigation of Crosstalk-Induced Load Modulation Effects

In Section 2.3.2, we reviewed the three basic precoding schemes in the literature, which are MRT, ZF, and MMSE precoding. These precoders are computationally efficient to implement, and are optimal under a total-transmit-power constraint. However, they result in channel-dependent disparities in the average-power levels across the different RF chains. These disparities could result in extreme crosstalk-induced load modulation behavior that cannot be handled by the dual-input DPD architecture in Section 2.2.3.

In this chapter, we analyze the combined effect of antenna crosstalk and precoding on the active impedances seen by the PAs in a MIMO transmitter, and propose a robust solution that mitigates these effects. The proposed solution comprises 1) a low-complexity algorithm that reduces the disparity in average-power levels arising from the conventional precoders, and 2) a load-dependent DPD architecture that ensures a consistent performance across all channel conditions.

3.1 Full Transmitter Model

Fig. 3.1 re-depicts the block diagram of the fully digital MIMO transmitter in Fig. 1.1. The figure now includes the linear precoding and power allocation models in Fig. 2.11, and the dual-input DPD architecture in Fig. 2.9. I/Q compensation modules were omitted from
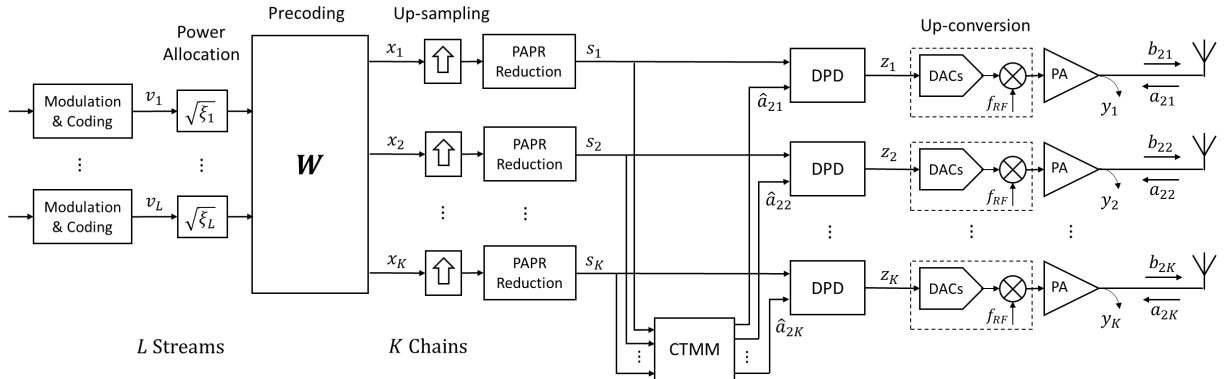
Figure 3.1: Detailed block diagram of an L-user K-chain massive MIMO transmitter that employs a dual-input DPD architecture.

the figure since a non-zero-IF transmitter architecture was employed for the experiments in this thesis. As the figure depicts, the L user signals are multiplied by the power control coefficients and the precoding matrix, yielding the K signals $x_1[n], \ldots, x_K[n]$. The precoded signals are up-sampled and fed to the PAPR reduction modules, resulting in the K signals $s_1[n], \ldots, s_K[n]$. These signals are processed by the dual-input DPD architecture, and the DPD outputs are up-converted to passband, fed to the PA array, and transmitted through the antennas. The output signal of each PA is sampled by a directional coupler and down-converted to baseband for use in DPD training. Note that time dependence has been omitted from the figure for better legibility, i.e., $x_k \triangleq x_k[n]$.

3.2 Analyzing the Effects of Antenna Crosstalk and Precoding on the PA Behavior

The efficiency, linearity, and output power of any PA are functions of the average power of its input signal as well as the active impedance at its output port. Because of antenna crosstalk, the average active impedance seen by each PA depends not only on its terminating antenna, but also on the signals transmitted by the neighboring PAs. Whenever the channel estimate is updated, a new precoding matrix is calculated, which changes the power levels and the cross-correlation properties of the signals fed to the PAs. This changes the relative strength of the crosstalk signal impinging on each PA output port and the extent to which it modulates the active impedance seen by that PA. Below, we analyze how the active impedances seen by the PAs depend on the precoding matrix and the antenna

28

array S-parameters. In this analysis, we ignore the pre-processing modules in Fig. 3.1 since they have no effect on the average-power levels.

Assume the L user signals to be continuous-wave (CW) tones at an arbitrary frequency f with unit amplitudes and arbitrary phases, i.e., $v_l[n] = e^{j2\pi f n + \theta_l} \, \forall l = 1, \ldots, L$. Since we are only interested in the reflection coefficients at the frequency of interest, we can omit time dependence to simplify notation, i.e., $v_l(f) = e^{j\theta_l}$. Given the precoding and power allocation matrices $\mathbf{W}$ and $\boldsymbol{\Xi}$, and assuming that all PAs have unity voltage gain at the frequency of interest, the incident wave vectors at the K antenna ports in Fig. 3.1 can then be calculated from (2.26) as

$$\mathbf{b}_2(f) = \begin{bmatrix} b_{21}(f) \\ \vdots \\ b_{2K}(f) \end{bmatrix} = \mathbf{W}\boldsymbol{\Xi}^{\frac{1}{2}}\boldsymbol{\Theta}(f), \tag{3.1}$$

where $\boldsymbol{\Theta}(f) = [e^{j\theta_1}, \ldots, e^{j\theta_L}]^T$. Given the antenna S-parameters matrix at the frequency of interest

$$\mathbf{S}(f) = \begin{bmatrix} S_{11}(f) & \cdots & S_{1K}(f) \\ \vdots & \ddots & \vdots \\ S_{K1}(f) & \cdots & S_{KK}(f) \end{bmatrix},$$

the active reflection coefficient at the kth antenna port is then

$$\Gamma_k(f) = \frac{a_{2k}(f)}{b_{2k}(f)} = \frac{\sum_{i=1}^{K} S_{ki}(f)\, b_{2i}(f)}{b_{2k}(f)}. \tag{3.2}$$

The above procedure gives the kth active reflection coefficient under one specific CW stimulus $[e^{j\theta_1}, \ldots, e^{j\theta_L}]^T$. With modulated signals, the input signal incident on each PA can be considered as a superposition of CW tones with continuously varying amplitudes and phases. The average active reflection coefficient at any frequency $\bar{\Gamma}_k(f)$ is that which minimizes the sum of squared errors to the active reflection coefficients across all possible input amplitudes and phases, i.e.,

$$\bar{\Gamma}_k(f) = \underset{\Gamma \in \mathbb{C}}{\operatorname{argmin}} \ \mathbb{E}\left[|a_{2k}(f) - \Gamma b_{2k}(f)|^2\right]$$

$$= \underset{\Gamma \in \mathbb{C}}{\operatorname{argmin}} \ \mathbb{E}\left[|a_{2k}(f)|^2 - \Gamma^* a_{2k}(f) b_{2k}^*(f) - \Gamma b_{2k}(f) a_{2k}^*(f) + |\Gamma|^2 |b_{2k}(f)|^2\right]. \tag{3.3}$$

The average active reflection coefficient $\bar{\Gamma}_k(f)$ is then obtained using Wirtinger calculus [41], i.e., differentiating with respect to Γ^* and treating Γ as a constant. Differentiating (3.3)

and setting the result to zero gives

$$-\mathbb{E}\big[a_{2k}(f)b_{2k}^*(f)\big] + \bar{\Gamma}_k(f)\mathbb{E}\big[|b_{2k}(f)|^2\big] = 0,$$

or equivalently,

$$\bar{\Gamma}_k(f) = \frac{\mathbb{E}\big[a_{2k}(f)b_{2k}^*(f)\big]}{\mathbb{E}\big[|b_{2k}(f)|^2\big]}. \tag{3.4}$$

Given $\mathbf{W}$, $\boldsymbol{\Xi}$, and $\boldsymbol{\Theta}(f)$, the incident and reflected waves at the kth antenna port can be expressed as

$$b_{2k}(f) = \underline{\mathbf{w}}_k \boldsymbol{\Xi}^{\frac{1}{2}} \boldsymbol{\Theta}(f)$$
$$a_{2k}(f) = \underline{\mathbf{s}}_k(f)\mathbf{b}_2(f) = \underline{\mathbf{s}}_k(f)\mathbf{W}\,\boldsymbol{\Xi}^{\frac{1}{2}} \boldsymbol{\Theta}(f), \tag{3.5}$$

where $\underline{\mathbf{s}}_k(f)$ denotes the kth row of $\mathbf{S}(f)$. Substituting (3.5) in (3.4) gives

$$\begin{aligned}\bar{\Gamma}_k(f) &= \frac{\mathbb{E}\left[\underline{\mathbf{s}}_k(f)\mathbf{W}\,\boldsymbol{\Xi}^{\frac{1}{2}}\boldsymbol{\Theta}(f)\boldsymbol{\Theta}^H(f)\boldsymbol{\Xi}^{\frac{1}{2}}\underline{\mathbf{w}}_k^H\right]}{\mathbb{E}\left[\underline{\mathbf{w}}_k\boldsymbol{\Xi}^{\frac{1}{2}}\boldsymbol{\Theta}(f)\boldsymbol{\Theta}^H(f)\boldsymbol{\Xi}^{\frac{1}{2}}\underline{\mathbf{w}}_k^H\right]} \\ &= \frac{\underline{\mathbf{s}}_k(f)\mathbf{W}\,\boldsymbol{\Xi}\underline{\mathbf{w}}_k^H}{\underline{\mathbf{w}}_k\boldsymbol{\Xi}\underline{\mathbf{w}}_k^H}, \end{aligned} \tag{3.6}$$

where the fact that $\mathbb{E}\big[\boldsymbol{\Theta}(f)\boldsymbol{\Theta}^H(f)\big] = \mathbf{I}_L$ was utilized. The average active reflection coefficient defined in (3.6) is a frequency-dependent metric that reduces to the kth antenna reflection coefficient $S_{kk}(f)$ if no crosstalk is present. This metric can also be expressed in impedance form as

$$\bar{Z}_k(f) = Z_0\,\frac{1 + \bar{\Gamma}_k(f)}{1 - \bar{\Gamma}_k(f)}, \tag{3.7}$$

where Z_0 is the reference impedance of the system. As will be experimentally shown in Section 3.5, evaluating $\bar{\Gamma}_k(f)$ at the center frequency of operation is sufficient for predicting the performance under wideband modulated signals.

Finally, it is important to emphasize that the active load modulation phenomenon described above only occurs because the input signals to the PAs are correlated (due to precoding). If the K input signals to the PAs were uncorrelated, the incident and reflected wave vectors would become $\mathbf{b}_2(f) = [e^{j\theta_1}, \ldots, e^{j\theta_K}]^T$ and $a_{2k}(f) = \underline{\mathbf{s}}_k(f)\mathbf{b}_2(f)$ respectively. Accordingly, $\mathbb{E}[b_{2i}(f)b_{2j}^*(f)] = 0 \ \forall\, i \neq j$. Substituting these in (3.4) yields

$$\bar{\Gamma}_k^{\text{unc.}}(f) = \frac{\mathbb{E}\big[\underline{\mathbf{s}}_k(f)\mathbf{b}_2(f)b_{2k}^*(f)\big]}{\mathbb{E}\big[|b_{2k}(f)|^2\big]} = S_{kk}(f). \tag{3.8}$$

Therefore, if the crosstalk signal affecting a given PA is uncorrelated with its driving stimulus, the instantaneous active impedance will vary equally in all directions around the nominal value $S_{kk}(f)$. In such case, crosstalk-induced instability is of no concern.
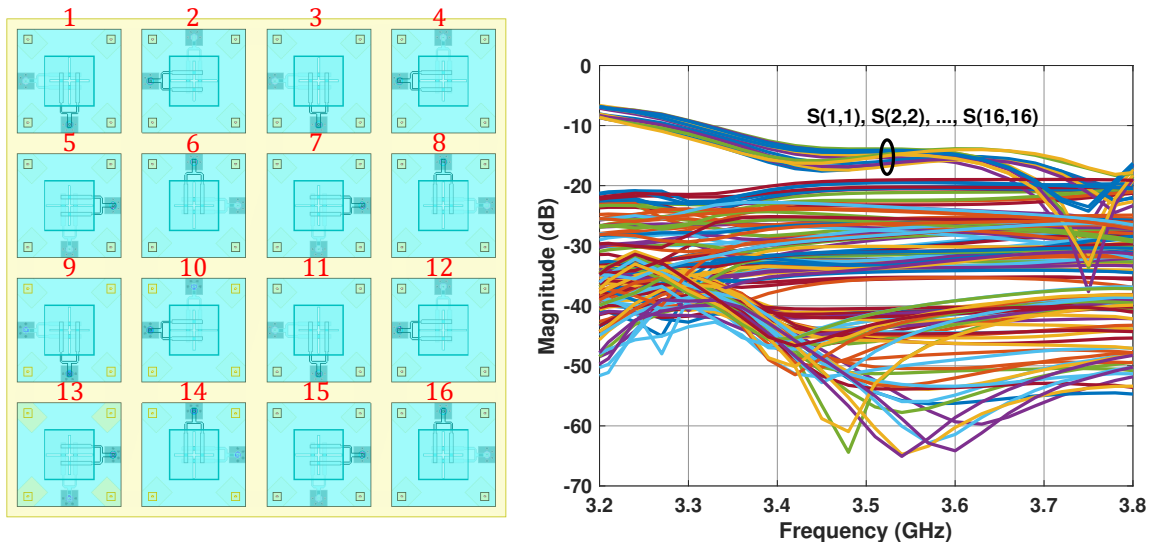
Figure 3.2: Layout of a 16-element antenna array and its S-parameters.

The conventional precoders introduced in Section 2.3.2 minimize the total transmitted power by the basestation but result in large disparities in the average-power levels across chains. These disparities correspond to significant variations in the average active impedances seen by the PAs (because the denominator of $\bar{\Gamma}_k(f)$ is $P_k = \underline{\mathbf{w}}_k \mathbf{\Xi} \underline{\mathbf{w}}_k^H$, so the magnitude of $\bar{\Gamma}_k(f)$ increases as P_k decreases relative to the other chains). To demonstrate this, we plot the average active impedances obtained with conventional ZF, across 10^7 channel realizations, for the 16-element antenna array layout shown in Fig. 3.2. These impedances were calculated at 3.5 GHz using (3.7). The number of users was $L = 4$, all users were allocated the same power (i.e., $\mathbf{\Xi} = \mathbf{I}_L$), and the channel matrices were generated according to a Rayleigh fading model, i.e., the elements of $\mathbf{H}$ were generated as independent, zero-mean, and unit-variance circularly-symmetric complex Gaussian random variables. Fig. 3.3 shows the results, where it can be seen that the extent of load modulation at any antenna port depends on its relative position in the array. This is because the antenna elements in the center are subject to more crosstalk than those at the corners. For the particular array in Fig. 3.2, coupling in the vertical direction (E-plane) is stronger than that in the horizontal direction (H-plane). Hence, an antenna at the top or bottom edges is subject to more crosstalk than one at the left or right edges.

31
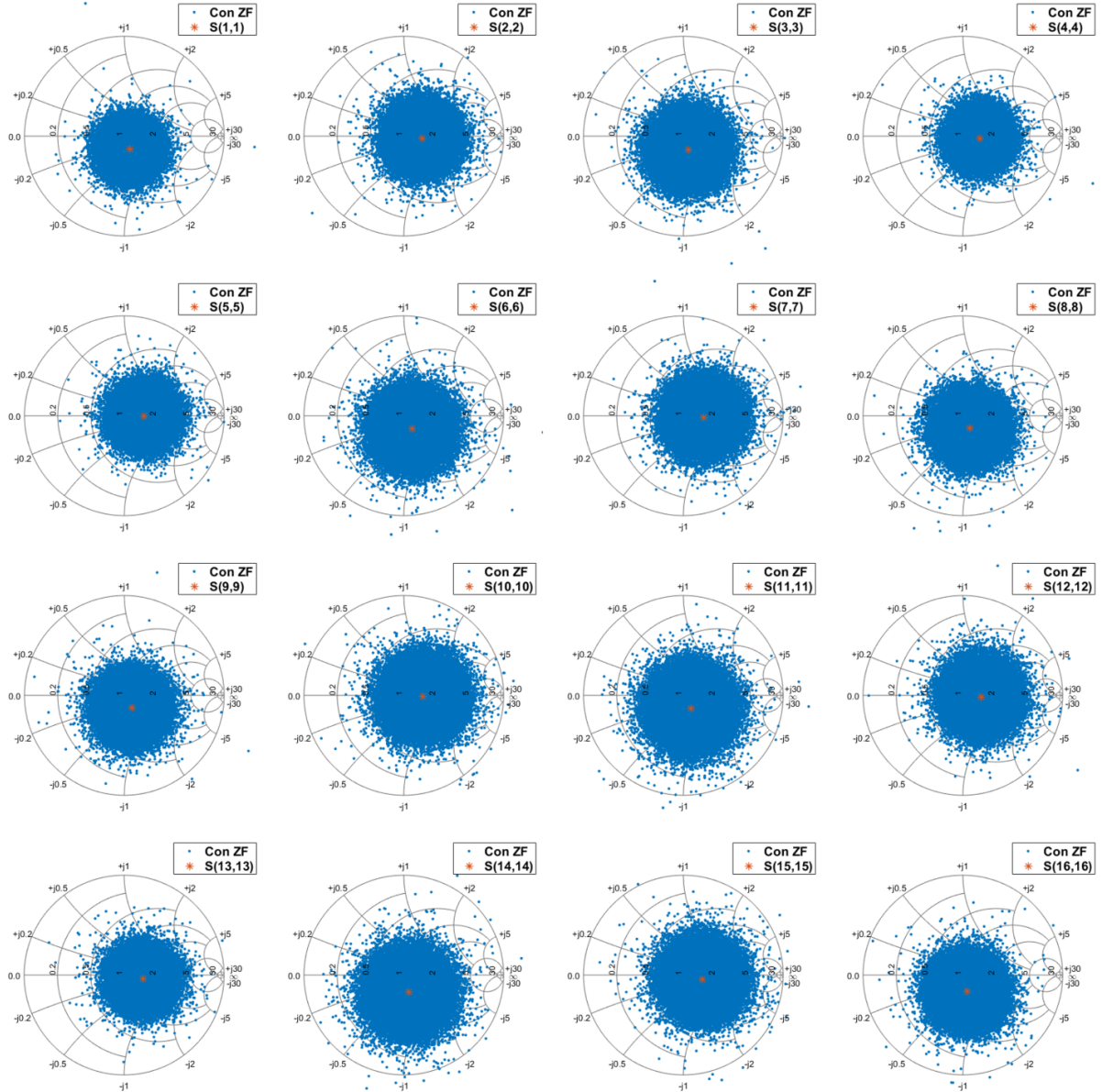
Figure 3.3: The average active impedances for the array in Fig. 3.2 with conventional ZF across 10^7 channel realizations. The red dots indicate the antenna reflection coefficients.

3.3 The Proposed Solution

Conventional precoders are computationally efficient to implement but give rise to substantial channel-dependent load modulation behavior, as Fig. 3.3 shows. In this section, we demonstrate how the performance of the conventional precoders can be improved, without a substantial increase in complexity.

3.3.1 Eliminating Extreme Cases

As Fig. 3.3 shows, conventional precoding may result in extreme loads that are outside the unit circle on the Smith chart, leading to potential instability. Such extreme cases arise when one PA is transmitting at a much lower average-power level than the neighboring PAs. These cases can be eliminated by modifying the conventional precoders using the following method. The method is first demonstrated on the ZF precoder before extending it to the two other precoders.

First, the conventional ZF precoder $\mathbf{W}_{\text{Con,ZF}}$ and the resulting average-power levels $P_1^{\text{Con}}, \ldots, P_K^{\text{Con}}$ are computed, from $\mathbf{H}$ and $\mathbf{\Xi}$, using (2.32) and (2.27) respectively. The objective is to increase the average-power levels in the chains with the lowest powers by perturbing the conventional precoder $\mathbf{W}_{\text{Con,ZF}}$ with $\alpha \mathbf{G}$ for some $\alpha \in \mathbb{R}$, where $\mathbf{G}$ is chosen such that the chains with the highest powers are unaffected. This reduces the disparity in average-power levels among the chains and eliminates extreme load modulation cases. We make use of the following lemma

Lemma. *Let $\mathbf{A}$ be an $L \times K$ matrix, where $K > L$. If $\mathbf{B}$ is a full-rank matrix constructed from $\mathbf{A}$ by replacing at most $K - L$ columns with zeros, then $\mathbf{AB}^\dagger = \mathbf{I}_L$. Moreover, if the kth column of $\mathbf{B}$ is an all-zero vector, the corresponding row in $\mathbf{B}^\dagger$ is all-zero as well.*

Proof. See [72], Lemma 1. □

Let Ω denote the set containing the indices of the R chains with the lowest average-power levels (the choice of R will be explained shortly). Also, let $\mathbf{H}_\Omega$ be obtained from $\mathbf{H}$ by keeping the R columns whose indices are in Ω and replacing the rest with zeros, i.e.,

$$\mathbf{H}_\Omega = \mathbf{H} \operatorname{diag}\left([\omega_1, \ldots, \omega_K]\right), \tag{3.9}$$

where $\omega_k = 1$ if $k \in \Omega$ and 0 otherwise. If $R \geq L$ and the elements of $\mathbf{H}$ are drawn from a continuous distribution, it is almost surely true that $\mathbf{H}_\Omega$ is of full rank. Accordingly, its pseudoinverse

$$\mathbf{G} = \mathbf{H}_\Omega^\dagger = \mathbf{H}_\Omega^H \left(\mathbf{H}_\Omega \mathbf{H}_\Omega^H\right)^{-1} \tag{3.10}$$

33

is well-defined. From the above lemma, $\mathbf{HG} = \mathbf{I}_L$ and the only non-zero rows in $\mathbf{G}$ are those whose indices are in Ω. Therefore, a new precoder defined as $\mathbf{W} = \mathbf{W}_{\mathrm{Con,ZF}} + \alpha \mathbf{G}$ preserves the ZF condition and allows increasing the average-power levels in the R chains with the lowest powers while keeping the rest intact. In this work, R is chosen as

$$R = \begin{cases} \max(B, L), & \text{if } B \neq 0 \\ \lfloor K/2 \rfloor, & \text{if } B = 0 \end{cases}, \tag{3.11}$$

where B is the number of chains whose average-power levels are less than one fourth of the maximum, i.e., $B = \mathrm{card}(\{k : P_k^{\mathrm{Con}} \leq P_{\max}^{\mathrm{Con}}/4\})$, where $P_{\max}^{\mathrm{Con}} = \max_k P_k^{\mathrm{Con}}$. The $1/4$ factor is heuristically chosen based on the worst-case scenario for the center patches in the array in Fig. 3.2. The above choice assumes that $\lfloor K/2 \rfloor \geq L$ (or $K \geq 2L$) since $\mathbf{G}$ is well-defined only if $R \geq L$. If $B = 0$, there will be no extreme load modulation cases, and the following procedure can be skipped altogether. Nevertheless, the RF performance can still be improved by reducing the disparity in average-power levels. As will be shown through numerical simulations below, setting $R = \lfloor K/2 \rfloor$ yields the best results on average.

For $k \in \Omega$, define $f_k(\alpha)$ as the difference between $P_{\max}^{\mathrm{Con}}$ and the average power in the kth chain when the precoding matrix is $\mathbf{W} = \mathbf{W}_{\mathrm{Con,ZF}} + \alpha \mathbf{G}$, i.e.,

$$\begin{aligned} f_k(\alpha) &= \left(\underline{\mathbf{w}}_{\mathrm{Con},k} + \alpha\,\underline{\mathbf{g}}_k\right) \mathbf{\Xi} \left(\underline{\mathbf{w}}_{\mathrm{Con},k} + \alpha\,\underline{\mathbf{g}}_k\right)^H - P_{\max}^{\mathrm{Con}} \\ &= \alpha^2\,\underline{\mathbf{g}}_k \mathbf{\Xi}\,\underline{\mathbf{g}}_k^H + 2\alpha\,\mathrm{Re}\{\underline{\mathbf{g}}_k \mathbf{\Xi}\,\underline{\mathbf{w}}_{\mathrm{Con},k}^H\} + P_k^{\mathrm{Con}} - P_{\max}^{\mathrm{Con}}, \end{aligned} \tag{3.12}$$

where $\underline{\mathbf{w}}_{\mathrm{Con},k}$ and $\underline{\mathbf{g}}_k$ denote the kth rows of $\mathbf{W}_{\mathrm{Con,ZF}}$ and $\mathbf{G}$ respectively, and the fact that $P_k^{\mathrm{Con}} = \underline{\mathbf{w}}_{\mathrm{Con},k} \mathbf{\Xi} \underline{\mathbf{w}}_{\mathrm{Con},k}^H$ was utilized. The function $f_k(\alpha)$ is quadratic in α with two roots $\alpha_k^{[1]}, \alpha_k^{[2]}$ that can be computed using the quadratic formula, i.e.,

$$\alpha_k^{[1,2]} = \frac{-\mathrm{Re}\{\underline{\mathbf{g}}_k \mathbf{\Xi}\,\underline{\mathbf{w}}_{\mathrm{Con},k}^H\} \mp \sqrt{\left(\mathrm{Re}\{\underline{\mathbf{g}}_k \mathbf{\Xi}\,\underline{\mathbf{w}}_{\mathrm{Con},k}^H\}\right)^2 + \underline{\mathbf{g}}_k \mathbf{\Xi}\,\underline{\mathbf{g}}_k^H \left(P_{\max}^{\mathrm{Con}} - P_k^{\mathrm{Con}}\right)}}{\underline{\mathbf{g}}_k \mathbf{\Xi}\,\underline{\mathbf{g}}_k^H}. \tag{3.13}$$

Note that the roots are real-valued since $\underline{\mathbf{g}}_k \mathbf{\Xi} \underline{\mathbf{g}}_k^H \in \mathbb{R}_+$ and $P_k^{\mathrm{Con}} < P_{\max}^{\mathrm{Con}} \,\forall\, k \in \Omega$ (i.e., the quantity under the square root is strictly positive). In addition, the two roots have opposite signs (i.e., $\alpha_k^{[1]} < 0 < \alpha_k^{[2]}$) since $f_k(0) < 0 \,\forall\, k \in \Omega$.

Given the roots of all R functions $\{f_k(\alpha), k, \in \Omega\}$, define α_{opt} as the root that has minimum absolute value, i.e.,

$$\alpha_{\mathrm{opt}} = \operatorname*{argmin}_{x \in \{\alpha_k^{[1]}, \alpha_k^{[2]}\}_{k \in \Omega}} |x|. \tag{3.14}$$

34

Since $f_k(\alpha)$ is quadratic, we have $f_k(\alpha) \leq 0 \; \forall \alpha_k^{[1]} \leq \alpha \leq \alpha_k^{[2]}$. Hence, with α_{opt} selected as in (3.14), all R chains in Ω will have average-power levels that are less than or equal $P_{\max}^{\mathrm{Con}}$ with at least one of them exactly equal to it. The proposed ZF precoder can then be constructed as

$$\mathbf{W}_{\mathrm{Prop}} = \big(\mathbf{W}_{\mathrm{Con,ZF}} + \alpha_{\mathrm{opt}}\mathbf{G}\big)/\big(1 + \alpha_{\mathrm{opt}}\big). \tag{3.15}$$

where the $1/(1 + \alpha_{\mathrm{opt}})$ factor is to ensure that $\mathbf{H}\mathbf{W}_{\mathrm{Prop}} = \mathbf{I}_L$. The above procedure for improving the conventional ZF precoder can also be applied to the MRT precoder since the $\mathbf{G}$ matrix in (3.10) satisfies the MRT condition in (2.29). The procedure can also be straightfarwardly extended to the MMSE case in (2.34) by replacing $\mathbf{G}$ with

$$\mathbf{H}_\Omega^H \left(\mathbf{H}_\Omega \mathbf{H}_\Omega^H + \frac{\sigma^2 \mathrm{tr}(\mathbf{\Xi}^{-1})}{P_{tot}} \mathbf{\Xi} \right)^{-1}.$$

In the proposed method, the $K - R$ rows of $\mathbf{W}_{\mathrm{Con}}$ with the highest powers are fixed while the rest are adjusted to increase their average-power levels, before normalizing by the factor $1/(1+\alpha_{\mathrm{opt}})$. This process can be repeated for a second time if needed, where the starting point becomes $\mathbf{W}_{\mathrm{Prop}}$ instead of $\mathbf{W}_{\mathrm{Con}}$. The method above can be considered as one modified iteration of the procedure in [72]. Therein, the conventional ZF precoder is modified through $K - L$ steps, where one row is fixed in the first step, two rows are fixed in the second step, and so on. If $B = 0$ (i.e., no extreme cases), choosing the optimal number of rows to fix is key to obtaining the highest performance gain with the least number of iterations. Fixing too many rows limits the degrees of freedom available, whereas fixing too few rows results in only minor adjustments. Fig. 3.4 shows the impact this choice has on the reduction in power disparity $\max_k P_k / \min_k P_k$ for $L = 4$, $K \geq 2L$ and $\mathbf{\Xi} = \mathbf{I}_L$ across 10^5 Rayleigh channel realizations. As the figure shows, fixing $\lceil K/2 \rceil$ rows (or equivalently, adjusting $\lfloor K/2 \rfloor$ rows) at a time yields the biggest reduction in power disparity.

To illustrate the effect of the proposed method on the power distribution across chains, numerical simulations for different settings of L and K were performed. Let P_k^{Prop} denote the average-power level of the kth chain after two iterations of the proposed ZF method. Three quantities were estimated and averaged across 10^5 Rayleigh channel realizations: 1) the reduction in maximum per-chain power $(\max_k P_k^{\mathrm{Con}} / \max_k P_k^{\mathrm{Prop}})$, 2) the reduction in power disparity $(\max_k P_k^{\mathrm{Con}} / \min_k P_k^{\mathrm{Con}}) / (\max_k P_k^{\mathrm{Prop}} / \min_k P_k^{\mathrm{Prop}})$, and 3) the increase in total power $(\sum_{k=1}^{K} P_k^{\mathrm{Prop}} / \sum_{k=1}^{K} P_k^{\mathrm{Con}})$. The three quantities are plotted in dB scale vs. the K/L ratio in Fig. 3.5 for $L = 2, 4$, and 6. As the figure shows, the proposed method reduces the maximum per-chain power and the disparity in transmitted powers among the different chains, at the expense of marginally increasing the total transmit power. Finally, Fig. 3.6 shows the average active impedances obtained after two iterations of the proposed

ZF method for the antenna array in Fig. 3.2, where it can be seen that no impedances are outside the unity circle.
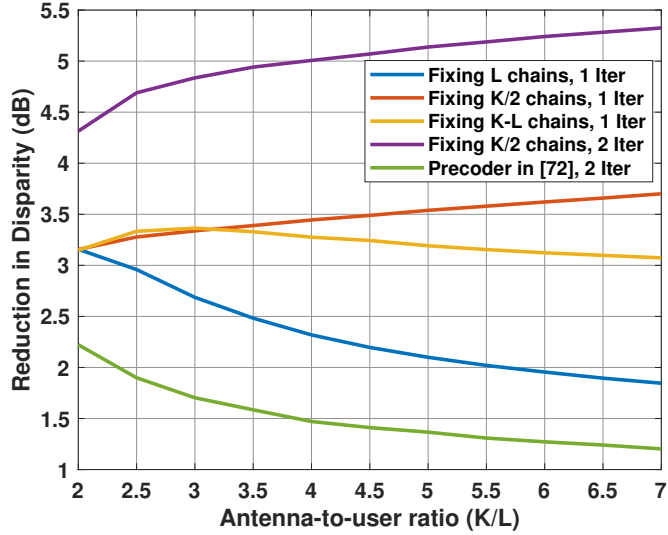
Figure 3.4: The average reduction in power disparity obtained with different settings for $L = 4$ and $\mathbf{\Xi} = \mathbf{I}_L$.
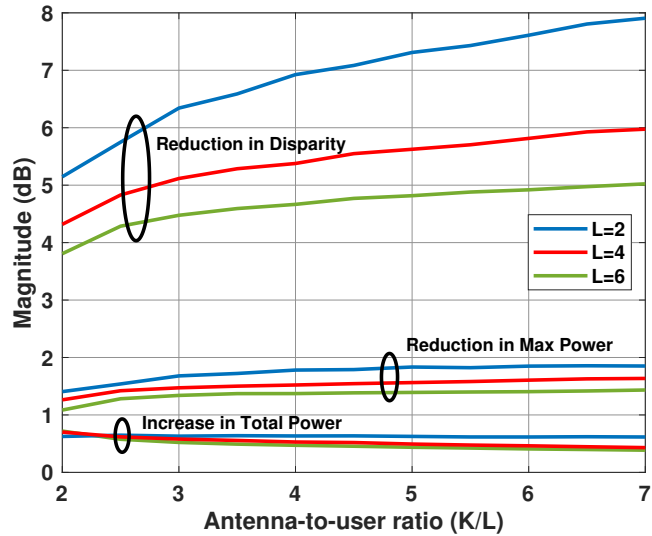

Figure 3.5: The differences in average-power levels when two iterations of the proposed method are applied to the conventional ZF precoder.
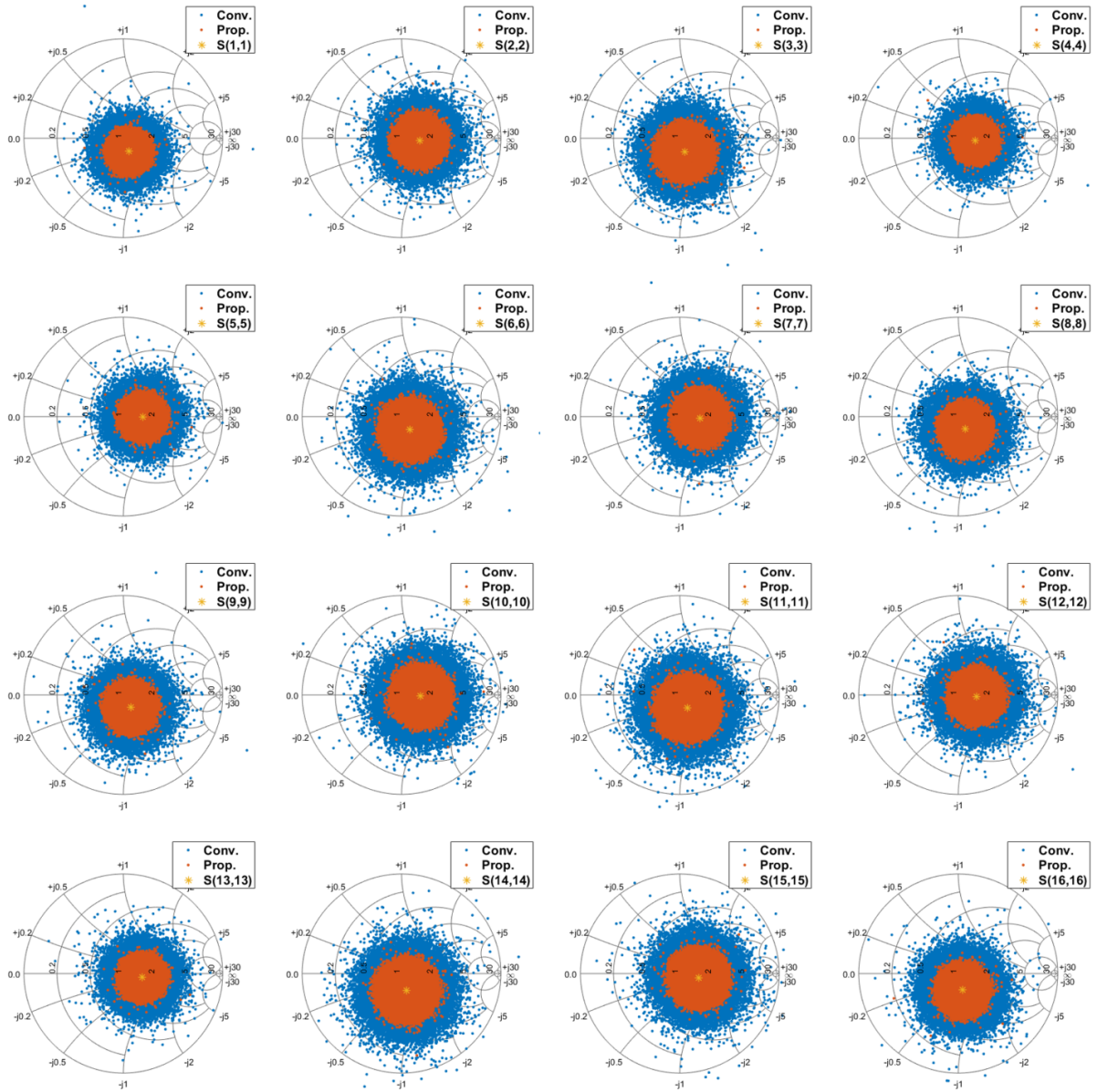
Figure 3.6: The average active impedances for the array in Fig. 3.2 with and without the proposed method applied to conventional ZF precoding.

3.3.2   Load-Dependent DPD Coefficient Sets

Eliminating extreme cases will not be sufficient in practice if the standard DPD architecture is employed. In [13], the precoding matrix $\mathbf{W}$ is bypassed during training and the DPD modules are fed with K independently generated (and hence, uncorrelated) signals $x_1[n], \ldots, x_K[n]$ (see Fig. 3.1). With uncorrelated stimuli, the synthesized average active impedances become equal to their nominal values, i.e., $\bar{\Gamma}_k(f) = S_{kk}(f) \, \forall \, k$, as (3.8) shows. Therefore, when precoding is subsequently employed, the trained DPD can perform poorly if the average active impedances are far from their nominal values. Although the proposed method in Section 3.3.1 significantly reduces the load modulation associated with conventional precoding techniques, the average active loads can still be somewhat far from the nominal values (see Fig. 3.6).

To maintain good linearity across all channel conditions at each PA output, we propose to utilize multiple average-load-dependent and power-dependent DPD coefficient sets. By training the DPD subsystem under multiple different channel conditions, each trained coefficient set would only cover a portion of the two-dimensional power-load space at each PA output. This improves the transmitter's resilience to variations in average powers and average active loads around the training points. With this arrangement, the dual-input DPD architecture can more effectively handle the instantaneous variations in powers and active loads.

For each PA, the Smith chart can be divided into regions according to the magnitude and phase of the average load deviation at the center frequency f_0

$$\Delta_k = \bar{\Gamma}_k(f_0) - S_{kk}(f_0) = \frac{\hat{\underline{\mathbf{s}}}_k(f_0)\mathbf{W}\,\boldsymbol{\Xi}\underline{\mathbf{w}}_k^H}{\underline{\mathbf{w}}_k\boldsymbol{\Xi}\underline{\mathbf{w}}_k^H}, \tag{3.16}$$

where $\hat{\underline{\mathbf{s}}}_k(f_0)$ is the kth row of $\mathbf{S}(f_0)$ with $S_{kk}(f_0)$ set to zero. One example of such division is shown in Fig. 3.7 with 5 regions. If the Smith chart is divided into N_Δ regions and the power range is divided into N_P intervals, $N_\Delta \times N_P$ coefficient sets per PA would be needed. The precoding matrix used for training a given set need not yield an average load that is exactly at the region centroid since the coefficient sets can be subsequently updated online.

In practice, the PAs' behavior may change with time due to changes in the surrounding environment (e.g., temperature, humidity,..) and/or operating conditions (e.g., center frequency, signal bandwidth,..). Hence, online training of the DPD modules is often necessary. The CTMM module in Fig. 3.1 can only be trained offline with uncorrelated signals, as will be shown in the next section. On the other hand, the DPD modules can be trained with any signals. Given the precoding and power allocation matrices within any coherence
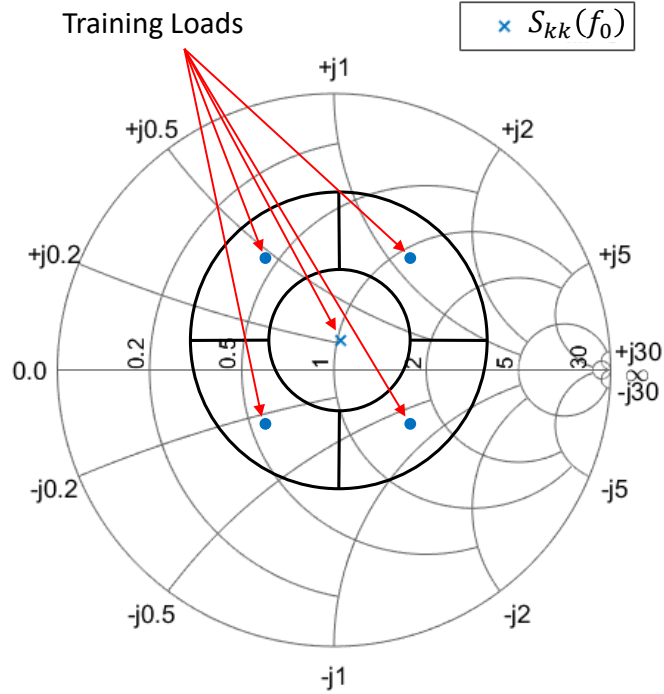
Figure 3.7: Dividing the Smith chart for each PA into regions.

interval, the K average load deviations $\Delta_1, \ldots, \Delta_K$ at the PAs' outputs and the average-power levels $P_1, \ldots, P_K$ can be calculated using (3.16) and (2.27) respectively. Then, for each PA, only one of the $N_\Delta \times N_P$ coefficient sets is updated, according to the intervals into which Δ_k and P_k fall, using the standard DPD update equation in (2.17).

With a sufficient number of load deviation regions, the DPD model used need not be complex. In this work, we use a simplified version of the DISO model in (2.24). Following the notation in Fig. 3.1, the DPD model in the kth chain is given by

$$
\begin{aligned}
z_k[n] = & \psi_k(\underline{\mathbf{s}}_k[n]) \\
& + \sum_{p=0}^{P-1} \sum_{m=0}^{M} \beta_{pm}^k \hat{a}_{2k}[n-m] \left| s_k[n-m] \right|^p \\
& + \sum_{p=0}^{P-3} \sum_{m=0}^{M} \gamma_{pm}^k \hat{a}_{2k}^*[n-m] s_k^2[n-m] \left| s_k[n-m] \right|^p,
\end{aligned}
\tag{3.17}
$$

where P is the non-linearity order, M is the memory depth, $\underline{\mathbf{s}}_k[n]$ is a row vector containing the samples of $s_k[n]$, and $\psi_k(.)$ is a conventional SISO DPD function that has no dependence

on the CTMM signal $\hat{a}_{2k}[n]$. The SISO function used in this work is a pruned combination of the models in [32] and [36], i.e.,

$$
\begin{aligned}
\psi_k(\underline{\mathbf{s}}_k[n]) = {} & \sum_{p=0}^{N-1} \sum_{m=0}^{M(p)} \tau_{pm}^k \, s_k[n-m] \, \big|s_k[n-m]\big|^p \\
& + \sum_{p=1}^{N-1} \sum_{m=1}^{M(p)} \epsilon_{pm}^k \, s_k[n-m] \, \big|s_k[n]\big|^p \\
& + s_k^2[n] \sum_{p=0}^{N-3} \sum_{m=1}^{M(p+2)} \vartheta_{pm}^k \, s_k^*[n-m] \, \big|s_k[n]\big|^p \\
& + s_k^*[n] \sum_{p=0}^{N-3} \sum_{m=1}^{M(p+2)} \varepsilon_{pm}^k \, s_k^2[n-m] \, \big|s_k[n]\big|^p .
\end{aligned}
\tag{3.18}
$$

where N is the SISO non-linearity order, M_S is the SISO memory depth, and $M(p) = \lfloor M_S(1 - \frac{p}{N-1}) \rfloor$ is the proposed memory-pruning function. Finally, the kth CTMM signal is computed, using Q-tap FIR filters, as

$$
\hat{a}_{2k}[n] = \sum_{i \neq k} \sum_{q=0}^{Q-1} \lambda'_{ki}[q] s_k[n-q],
\tag{3.19}
$$

where the terms corresponding to $i = k$ have been omitted from the original CTMM equation in (2.25) as they can be absorbed into the SISO function $\psi_k(\mathbf{s}_k[n])$. If the number of antennas is large, coupling between far-spaced antennas can be considered negligible. Hence, the summation on i in (3.19) need not be over all $K-1$ chains.

3.4 Estimating the Antenna S-Parameters

Calculating the coefficients of the CTMM module, as well as determining the average load deviations at the PA outputs using (3.16), requires knowledge of the antenna array S-parameters. If these are known in advance, the CTMM coefficients can be calculated using (2.21) with a slight modification. Since the baseband processing rate (i.e., F_s) is 3 to 5 times the modulation bandwidth, the input signals to the CTMM module $s_1[n], \ldots, s_K[n]$ do not span the whole baseband bandwidth $[-F_s/2, F_s/2]$. Accordingly, the calculated CTMM filters should favor the in-band portion of the baseband spectrum. This can be

achieved by multiplying both sides of (2.21) with a diagonal weighting matrix that assigns more weight to the in-band frequencies.

Alternatively, if the S-parameters are unknown, the CTMM coefficients can be estimated using the following procedure. This procedure is a generalization of that in [13], which is only valid for single-tap CTMM filters (i.e., $Q = 1$). As will be experimentally shown in Section 3.5, using multiple-tap CTMM filters is necessary to compensate for frequency-selective antenna behavior, especially with large modulation bandwidths.

The output signal of the kth PA can be modeled, as a function of the K input signals to the PAs $z_1[n], \ldots, z_K[n]$, using a simplified version of the dual-input PA model in (2.23) and (2.20), i.e.,

$$
\begin{aligned}
y_k[n] = {} & \psi_k(\underline{\mathbf{z}}_k[n]) \\
& + \sum_{p=0}^{P-1} \sum_{m=0}^{M} \eta_{pm}^k a_{2k}[n-m] \left| z_k[n-m] \right|^p \\
& + \sum_{p=0}^{P-3} \sum_{m=0}^{M} \mu_{pm}^k a_{2k}^*[n-m] z_k^2[n-m] \left| z_k[n-m] \right|^p,
\end{aligned}
\tag{3.20}
$$

where the crosstalk signal at the kth antenna port is

$$
a_{2k}[n] = \sum_{i \neq k} \sum_{q=0}^{Q-1} \lambda_{ki}[q] z_k[n-q].
\tag{3.21}
$$

The structure of the PA model used in this work is identical to that of the DPD model in (3.17)-(3.19), as is customary [13]. Note that the kth DPD output $z_k[n]$ is a function of the chain input $s_k[n]$ and the corresponding CTMM signal $\hat{a}_{2k}[n]$, while the kth PA output $y_k[n]$ is a function of the predistorted signal $z_k[n]$ and the corresponding crosstalk signal $a_{2k}[n]$. Because of the first-order approximations made in Section 2.2.3, the CTMM coefficients are linearly related to the antenna coefficients as $\lambda'_{ki}[q] = G\lambda_{ki}[q]$, where G is the PA gain. Hence, estimating the CTMM coefficients is equivalent to estimating the antenna coefficients.

The CTMM coefficients are estimated separately for each chain. For the kth chain, the objective is to estimate $K - 1$ coefficient vectors $\boldsymbol{\lambda}_{ki} = [\lambda_{ki}[0], \ldots, \lambda_{ki}[Q-1]]^T, i \neq k$. The first step is to LS fit the kth PA output signal $y_k[n]$ to a SISO model $\psi_k(\underline{\mathbf{z}}_k[n])$ then subtract the fitted model from it to obtain the following signal

$$
v_k[n] = y_k[n] - \psi_k(\underline{\mathbf{z}}_k[n]).
\tag{3.22}
$$

Step 0:

Known: $v_k[n] = y_k[n] - \psi_k(\underline{z}_k[n])$

Set: $\hat{\lambda}_{ki}[q] = \begin{cases} 1, & q = 0 \\ 0, & \text{otherwise} \end{cases}, \; \forall i \neq k$

Step 1:

Use $\hat{\boldsymbol{\lambda}}_k$ in (3.21) to compute $a_{2k}[n]$

Compute the basis matrix $\boldsymbol{A}_k$ in (3.24) and estimate $\hat{\boldsymbol{\eta}}_k, \hat{\boldsymbol{\mu}}_k$

Step 2:

Use $\hat{\boldsymbol{\eta}}_k, \hat{\boldsymbol{\mu}}_k$ to compute the basis matrices $\boldsymbol{B}_k, \boldsymbol{Y}_k$ in (3.26)

Estimate $\hat{\boldsymbol{\lambda}}_k$ from (3.27) and normalize

Accuracy ?

No

Yes

$\hat{\boldsymbol{\lambda}}_k, \hat{\boldsymbol{\eta}}_k, \hat{\boldsymbol{\mu}}_k$ found
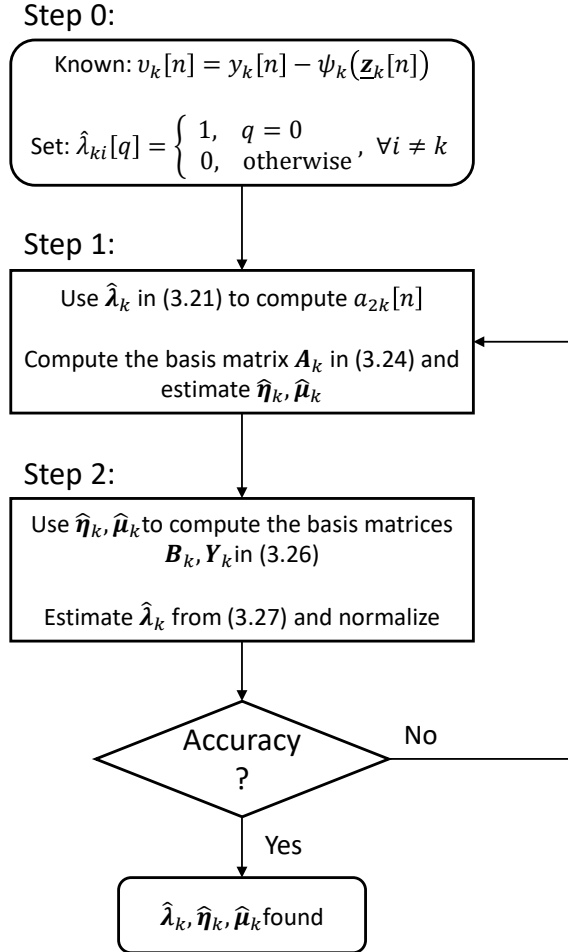
Figure 3.8: Flowchart for identifying the CTMM coefficients of the kth path.

The dual-input PA and antenna coefficients can then be obtained from this signal using the iterative procedure shown in Fig. 3.8. Note that this procedure is only possible if the K input signals are linearly independent i.e., the DPD and CTMM modules are bypassed and the PAs are fed with K uncorrelated signals. Therefore, this procedure can only be carried out offline (with no precoding or DPD employed).

The antenna coefficients are initially set to $\boldsymbol{\lambda}_{ki} = [1, 0, \ldots, 0]^T, \; \forall i \neq k$. In step 1 of the procedure, the antenna coefficients are used to compute the crosstalk signal using (3.21), and the dual-input coefficient vectors $\boldsymbol{\eta}_k = \{\eta_{pm}^k\}, \boldsymbol{\mu}_k = \{\mu_{pm}^k\}$ are estimated by fitting the

signal $\upsilon_k[n]$ to the dual-input bases in (3.20), i.e.,

$$\upsilon_k[n] = \sum_{p=0}^{P-1} \sum_{m=0}^{M} \eta_{pm}^k a_{2k}[n-m] \left| z_k[n-m] \right|^p$$
$$+ \sum_{p=0}^{P-3} \sum_{m=0}^{M} \mu_{pm}^k a_{2k}^*[n-m] z_k^2[n-m] \left| z_k[n-m] \right|^p. \tag{3.23}$$

In matrix form, the dual-input coefficient vectors $\boldsymbol{\eta}_k, \boldsymbol{\mu}_k$ can be estimated as

$$\begin{bmatrix} \hat{\boldsymbol{\eta}}_k \\ \hat{\boldsymbol{\mu}}_k \end{bmatrix} = \mathbf{A}_k^\dagger \boldsymbol{v}_k, \tag{3.24}$$

where $\boldsymbol{v}_k$ is a vector containing the samples of $\upsilon_k[n]$, and $\mathbf{A}_k$ is the basis matrix for the model in (3.23).

In Step 2, the antenna coefficients are re-estimated by fitting the signal $\upsilon_k[n]$ to the model below

$$\upsilon_k[n] = \sum_{i \neq k} \sum_{q=0}^{Q-1} \lambda_{ki}[q] \sum_{p=0}^{P-1} \sum_{m=0}^{M} \hat{\eta}_{pm}^k z_i[n-m-q] \left| z_k[n-m] \right|^p$$
$$+ \sum_{i \neq k} \sum_{q=0}^{Q-1} \lambda_{ki}^*[q] \sum_{p=0}^{P-3} \sum_{m=0}^{M} \hat{\mu}_{pm}^k z_i^*[n-m-q] z_k^2[n-m] \left| z_k[n-m] \right|^p, \tag{3.25}$$

whose basis are computed using the dual-input coefficient vectors $\hat{\boldsymbol{\eta}}_k, \hat{\boldsymbol{\mu}}_k$ estimated in the previous step. This relation can be expressed in a more compact form as

$$\boldsymbol{v}_k = \mathbf{B}_k \boldsymbol{\lambda}_k + \mathbf{Y}_k \boldsymbol{\lambda}_k^*, \tag{3.26}$$

where $\boldsymbol{\lambda}_k$ is a $Q(K-1) \times 1$ vector obtained by stacking all the $\boldsymbol{\lambda}_{ki}; i \neq k$ vectors, $\boldsymbol{v}_k$ is as above, and $\mathbf{B}_k, \mathbf{Y}_k$ are the basis matrices for the model in (3.25). The equation above can be solved for $\hat{\boldsymbol{\lambda}}_k$ by splitting it into its real and imaginary parts, yielding

$$\begin{bmatrix} \mathrm{Re}\{\hat{\boldsymbol{\lambda}}_k\} \\ \mathrm{Im}\{\hat{\boldsymbol{\lambda}}_k\} \end{bmatrix} = \begin{bmatrix} \mathrm{Re}\{\mathbf{B}_k + \mathbf{Y}_k\} & \mathrm{Im}\{\mathbf{Y}_k - \mathbf{B}_k\} \\ \mathrm{Im}\{\mathbf{B}_k + \mathbf{Y}_k\} & \mathrm{Re}\{\mathbf{B}_k - \mathbf{Y}_k\} \end{bmatrix}^\dagger \begin{bmatrix} \mathrm{Re}\{\boldsymbol{v}_k\} \\ \mathrm{Im}\{\boldsymbol{v}_k\} \end{bmatrix} \tag{3.27}$$

The two steps of the procedure above are iterated several times until convergence is observed. Finally, we note that the solution for the antenna coefficients $\hat{\boldsymbol{\lambda}}_k$ and the PA

coefficients $\hat{\boldsymbol{\eta}}_k, \hat{\boldsymbol{\mu}}_k$ is not unique, since multiplying one set by an arbitrary factor while reciprocally scaling the other will result in the same output. This ambiguity also carries over to the CTMM coefficients since they are linearly related to the antenna coefficients. To avoid this, we follow the same approach in [13]: After step 2, we normalize the $\hat{\boldsymbol{\lambda}}_k$ vector so that the maximum absolute of its entries is 1.

3.5 Experimental Results
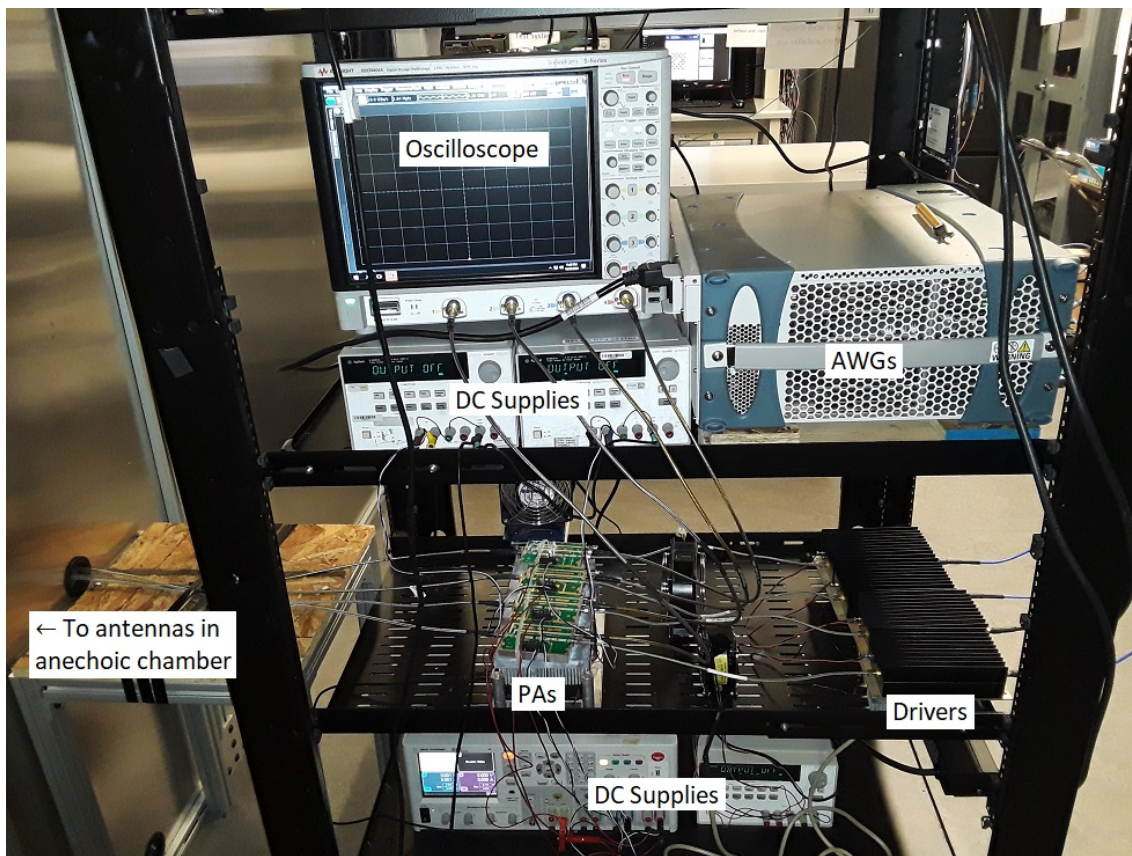
Figure 3.9: A photograph of the measurement setup.

The effectiveness of the proposed methods is now validated through measurements on a two-user four-chain fully digital prototype transmitter operating at a center frequency of 3.5 GHz. A photograph of the setup is shown in Fig. 3.9. The transmitter consists of two

Keysight M8190A dual-channel arbitrary waveform generator (AWG)s, four Minicircuits ZHL-42W driver amplifiers, four custom-designed PAs, and a four-element patch antenna array. The antenna array, shown in Fig. 3.10, is a 2x2 rectangular patch configuration with a worst-case crosstalk level of 20 dB. The PA module, shown in Fig. 3.11, is a class-AB design based on Wolfspeed's CGHV1F006 Gallium Nitride (GaN) transistor with a peak output power of 4 Watts. The PAs' outputs are sampled using four Anaren XC3500P-20S directional couplers and fed to a four-channel Keysight DSOS404A oscilloscope for signal monitoring and DPD training.

We begin by demonstrating the importance of utilizing multi-tap FIR filters in the CTMM module. For this, the DPD modules were trained using four independently generated (and hence, uncorrelated) 100-MHz OFDM signals with 8-dB PAPR and an up-sampling ratio of 5 (i.e., $F_s = 500$ MHz). This is the maximum expected bandwidth in sub-6 5G systems [44]. The dual-input DPD parameters in (3.17)-(3.19) were set to $P = 5$ and $M = 1$, and the SISO parameters were set to $N = 8$ and $M_S = 5$. This amounted to 69 coefficients in total (53 SISO + 16 dual-input). The length of the CTMM filters was set to both $Q = 3$ and $Q = 1$. Table 3.1 shows the RNMSE and lower/upper ACPR values at the individual PA outputs with both SISO and DISO DPD models, while Fig. 3.12 shows the resulting spectra. As expected, SISO DPD exhibits poor linearization performance because of the non-negligible antenna crosstalk. The table also shows that using one-tap CTMM filters yields unsatisfactory results because of the frequency-selectivity of the antenna S-parameters over the 100-MHz modulation bandwidth. For the antenna array used here, the minimum CTMM filter length for satisfactory linearization performance is $Q = 3$.

Table 3.1: RNMSE (%) and Lower/Upper ACPRs (dB) at the outputs of the four PAs with different DPD configurations.

DPD Type	PA 1	PA 2	PA 3	PA 4
None	8.4%	11.8%	8.9%	12.2%
	-36.2/-32.7	-34.9/-33.6	-37.3/-31.0	-35.0/-34.0
SISO	3.2%	3.2%	3.1%	2.8%
	-45.1/-46.4	-46.3/-46.8	-45.3/-44.6	-46.2/-46.9
DISO ($Q = 1$)	1.7%	1.5%	1.5%	1.4%
	-46.7/-48.0	-48.2/-48.5	-46.7/-46.6	-48.1/-48.5
DISO ($Q = 3$)	0.7%	0.7%	0.8%	0.8%
	-51.7/-51.3	-52.2/-51.4	-50.1/-50.0	-52.3/-51.9
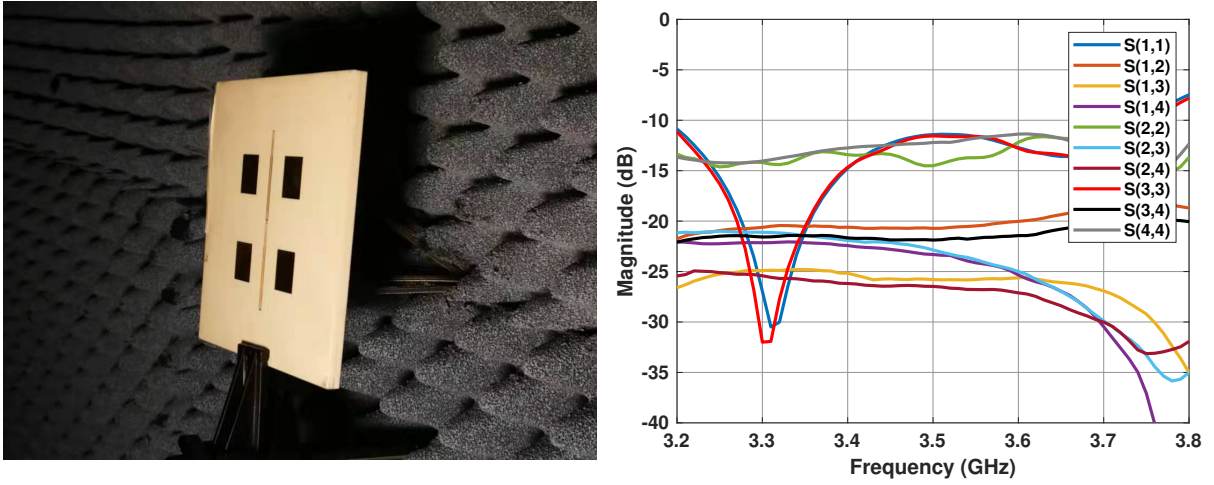
Figure 3.10: The antenna array in the anechoic chamber and its S-parameters.
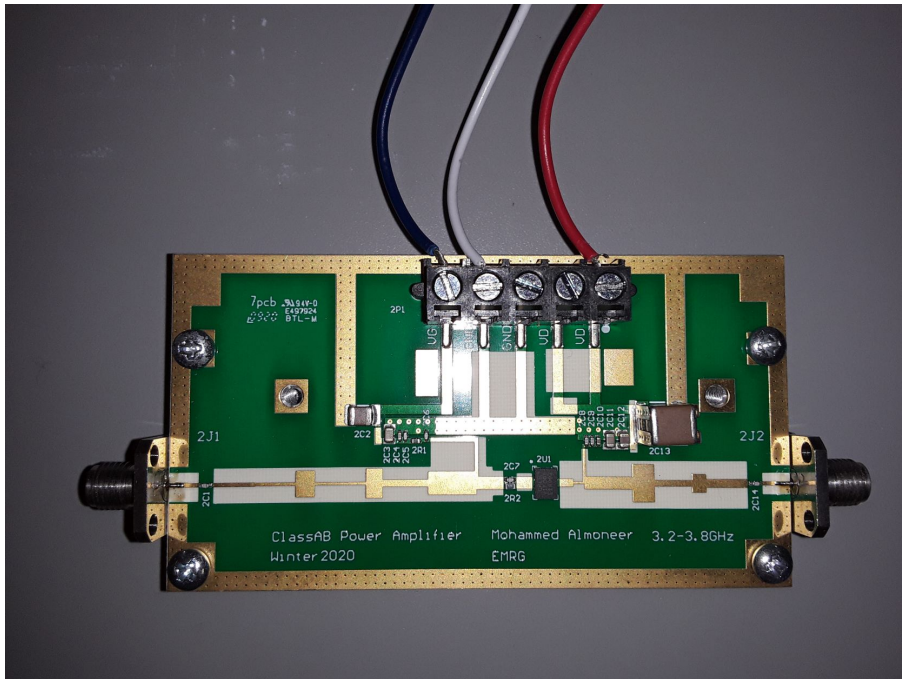
Figure 3.11: The PA module.
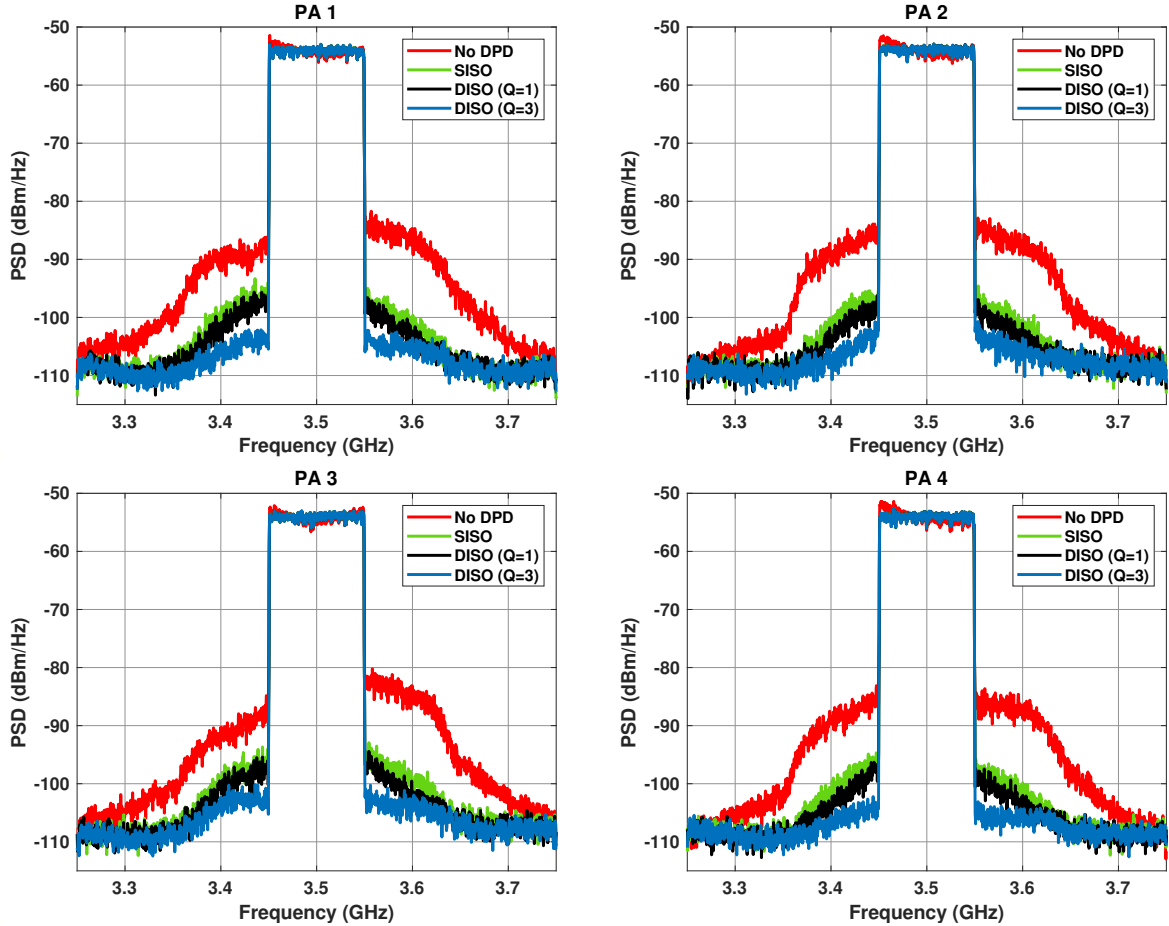
Figure 3.12: Spectra of the individual PA outputs with different DPD configurations.

Next, we demonstrate the need for the proposed schemes in Section 3.3. For each PA, the Smith chart was divided into $N_\Delta = 5$ regions, and the power range was divided into $N_P = 3$ intervals, resulting in 15 coefficient sets per PA. Fig. 3.13 shows the load deviation regions and the training loads for one of the four PAs. The CTMM module and the coefficient sets at the center load (at which $\bar{\Gamma}_k(f) = S_{kk}(f)$) were trained with 100-MHz uncorrelated OFDM signals. Five channel matrices that yield extreme loads at one PA were then picked, and the conventional ZF precoder was applied to each. Only one iteration of the proposed scheme in Section 3.3.1 was carried out, yielding the adjustments shown with the red arrows in Fig. 3.13. The five selected channels gave ordinary loads for the three other PAs, so their results are omitted for brevity.

47
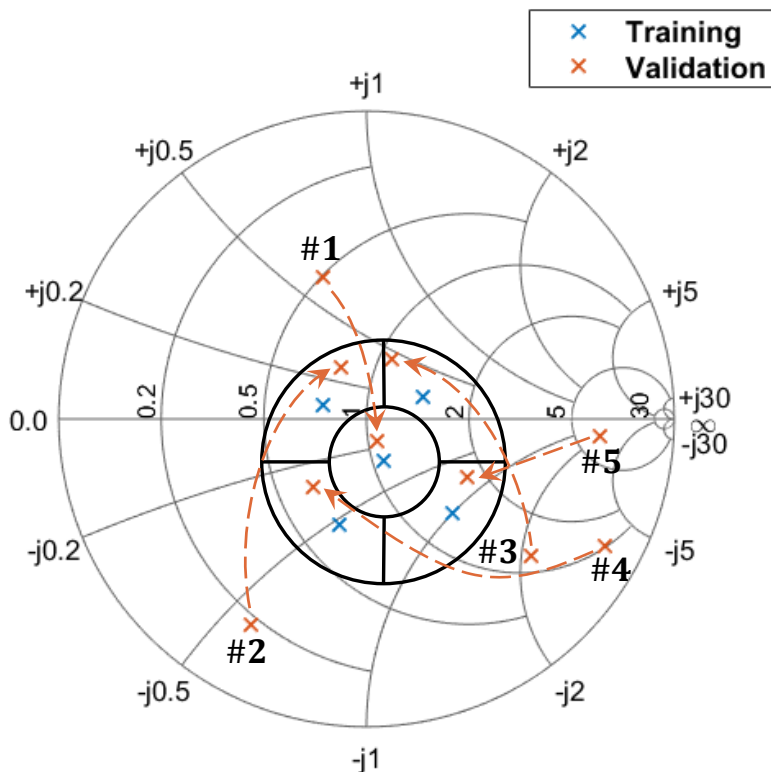
Figure 3.13: The training and verification loads for one of the four PAs.

Table 3.2 shows the RNMSE and lower/upper ACPR values obtained at the output of the designated PA, for the five selected channels, under three scenarios: i) conventional ZF precoding and DPD, ii) proposed ZF precoding and conventional DPD (single coefficient set trained with uncorrelated signals), and iii) proposed ZF precoding and load-dependent DPD. As expected, the proposed precoding technique substantially improves linearization performance by reducing the variations in average-power levels and active impedances. In addition, further improvements can be obtained by utilizing multiple coefficient sets per PA. The extent of these improvements, however, depends on the number of coefficient sets utilized (i.e., N_Δ and N_P) and the characteristics of the PA itself. Accordingly, better results can be obtained by utilizing smaller load deviation regions that are tailored to the specific PA nonlinearity. These regions need not be of the regular geometrical shapes depicted in Fig. 3.13. It is, therefore, crucial that the PAs be pre-characterized in order to determine the optimal load deviation regions and power intervals.

Table 3.2: RNMSE (%) and ACPR (dB) results for one of the four PAs under different precoding and DPD configurations.

Channel #	Con. precoding & con. DPD	Prop. precoding & con. DPD	Prop. precoding & prop. DPD
1	11.4%	0.8%	0.8%
	-45.9/-48.4	-51.6/-53.2	-51.6/-53.2
2	5.1%	5.3%	1.0%
	-43.8/-43.8	-49.0/-46.3	-50.2/-49.7
3	15.9%	2.1%	2.3%
	-42.6/-41.7	-48.6/-46.7	-51.2/-50.6
4	17.3%	3.5%	2.2%
	-42.3/-40.7	-50.5/-48.9	-52.5/-52.4
5	12.6%	7.2%	1.2%
	-41.8/-39.9	-47.8/-47.0	-49.5/-49.6

3.6 Summary

In this chapter, we presented a thorough analysis of the impact of precoding on the RF performance of massive MIMO transmitters exhibiting non-negligible antenna crosstalk. It was shown that the disparity in average-power levels arising from conventional precoding schemes (MRT, ZF, and MMSE) leads to substantial variations in the average active loads seen at the PA outputs. This load modulation behavior gives rise to channel-dependent variations in the RF performance and linearity of the PAs. Based on this analysis, a robust solution that mitigates such behavior was proposed. The proposed solution comprises a low-complexity technique that reduces the power disparity arising from the conventional precoders, and a load-dependent DPD architecture that mitigates the residual distortions. The proposed solution was experimentally validated on a prototype MIMO system with 100-MHz OFDM signals, where excellent linearization performance across all channel conditions was observed.

Chapter 4

Crosstalk-Aware Precoding

In Chapter 3, it was shown that conventional precoding schemes result in large channel-dependent disparities in average-power levels across the different RF chains, which can have adverse effects on the RF performance. Using the relatively low-complexity method in Section 3.3.1, these disparities can be somewhat, but not fully, mitigated. Consequently, maintaining a consistent performance across all channel conditions necessitates employing multiple load-dependent and power-dependent DPD coefficient sets, in conjunction with the method in Section 3.3.1. The disadvantages of this solution, however, are the increased DPD training duration and the need to pre-characterize the PAs' behavior.

In this chapter, an alternative solution to the problem is presented. We propose three linear precoding schemes that result in equal average-power levels across all RF chains, no matter what the channel conditions are. Computing the precoders proposed in this chapter is more computationally complex than modifying the conventional precoders using the scheme in Section 3.3.1. Nevertheless, the precoders proposed here fully eliminate the disparities in average-power levels, which means that only one DPD coefficient set per PA would be needed. In addition, forcing all RF chains to transmit the same average power simplifies the hardware design and pre-processing required. For instance, the clipping limits in all PAPR reduction modules can be set to the same value, which makes all signals have the same dynamic range. Consequently, the scaling settings of the DACs and the gain settings of the driver-stage amplifiers preceding the PAs can be set the same across all chains.

4.1 Equal-Average-Power Precoding

4.1.1 MRT

The conventional MRT precoder minimizes the total transmit power needed to ensure that $[\mathbf{HW}]_{l,l} = 1 \, \forall \, l = 1, \ldots, L$ but results in a significant disparity in the average transmitted powers across chains. Such disparity can be minimized by changing the objective function in (2.29) to be the maximum per-chain power, instead of the total transmit power. Accordingly, we define the minimax MRT precoder to be the solution to

$$\mathbf{W}_{\mathrm{Mm-MRT}} = \operatorname*{argmin}_{\mathbf{W} \in \mathbb{C}^{K \times L}} \, \max_{k \in \{1, \ldots, K\}} \, P_k \qquad \text{s.t.} \, (\mathbf{HW})_{l,l} = 1 \quad \forall \, l. \tag{4.1}$$

Unlike the conventional MRT precoder, the minimax precoder defined above does not posses a closed-form solution. Nevertheless, the optimization problem in (4.1) is a convex second-order cone program (SOCP) that can be solved efficiently using primal-dual interior-point methods [77].

Since the elements of $\mathbf{H}$ are drawn from a continuous distribution, it is almost surely true that $H_{l,k} \neq 0 \, \forall \, l, k$. As the following theorem shows, if this condition is satisfied, the minimax MRT precoder results in equal average-power levels across all chains. Thus, it is referred to, henceforth, as the equal-power (EP) MRT precoder.

Theorem. *If $H_{l,k} \neq 0 \, \forall \, l, k$, the precoder defined in (4.1) yields equal average-power levels across all chains.*

Proof. Since $H_{l,k} \neq 0 \, \forall \, l, k$, the constrained optimization over KL variables in (4.1) can be reduced to one over $(K-1)L$ variables by eliminating the L equality constraints $(\mathbf{HW})_{l,l} = \sum_{k=1}^{K} H_{l,k} W_{k,l} = 1$ for $l = 1, \ldots, L$. Without loss of generality, we eliminate the L variables in the mth-row $W_{m,1}, \ldots, W_{m,L}$ by substituting for the equality constraints in the expression of P_m. Using the element form of (2.27), the optimization problem above can be rewritten as

$$\min_{\{W_{k,l}\}_{k \neq m}^{l=1, \ldots, L}} \, \max_{k \in \{1, \ldots, K\}} \, P_k \tag{4.2}$$

where, $\forall \, k \in \{1, \ldots, K\}$,

$$P_k = \begin{cases} \sum_{l=1}^{L} \xi_l \left| (1 - \sum_{s \neq m} H_{l,s} W_{s,l})/H_{l,m} \right|^2, & k = m \\ \sum_{l=1}^{L} \xi_l |W_{k,l}|^2, & k \neq m. \end{cases}$$

51

As evident from (4.2), the choice of the nth-row precoding coefficients $W_{n,1}, \ldots, W_{n,L}$, where $n \in \{1, \ldots, K\}, n \neq m$, affects only P_m and P_n. Either P_m or P_n can be made equal to zero by appropriately choosing the nth-row coefficients while keeping those in all the other rows fixed, i.e., setting $W_{n,l} = 0 \; \forall l$ yields $P_n = 0$ while setting $W_{n,l} = (1 - \sum_{s \neq m,n} H_{l,s} W_{s,l})/H_{l,n} \; \forall l$ yields $P_m = 0$.

Therefore, an optimal solution to the problem in (4.2) must result in $P_n = P_m \; \forall m, n \in \{1, \ldots, K\}$. Suppose a claimed solution results in $m = \text{argmax}_k P_k$ (i.e., $P_m = \max_k P_k$) with $P_n \neq P_m$ for some n. Then, the nth-row coefficients can be altered so that $P_n < P_n^{\text{new}} = P_m^{\text{new}} < P_m$. This is because P_m and P_n are both continuous functions of $W_{n,1}, \ldots, W_{n,L}$. If $P_s < P_m \; \forall s \neq m, n$, then a better solution has been obtained since $P_m^{\text{new}} < P_m$. Otherwise, the same process can be repeated again $\forall s; P_s = P_m$, where each time $P_s^{\text{new}} < \max(P_s, P_m^{\text{new}})$. $\qquad \square$

To illustrate the differences between the conventional and EP MRT precoders, numerical simulations for different settings of L and K were performed. All users were allocated the same power (i.e., $\boldsymbol{\Xi} = \mathbf{I}_L$) and the channel matrices were generated according to a Rayleigh fading model. Let P_k^{EP} and P_k^{Con} denote the average-power levels of the kth chain under EP and conventional MRT precoding respectively. Three quantities were estimated and averaged across 10^5 realizations: 1) the reduction in maximum per-chain power $(\max_k P_k^{\text{Con}}/\max_k P_k^{\text{EP}})$, 2) the reduction in power disparity $(\max_k P_k^{\text{Con}}/\min_k P_k^{\text{Con}})$ $/(\max_k P_k^{\text{EP}}/\min_k P_k^{\text{EP}})$, and 3) the increase in total power $(\sum_{k=1}^K P_k^{\text{EP}}/\sum_{k=1}^K P_k^{\text{Con}})$. The three quantities are plotted in dB scale vs. the K/L ratio in Fig. 4.1 for $L = 2, 4$, and 6. From the figure, it can be seen that the EP precoder appreciably reduces the maximum per-chain power, at the expense of marginally increasing the total transmit power. More importantly, the disparity in transmitted powers among the different chains is significantly reduced.

4.1.2 Regularized ZF

Similarly, the minimax ZF precoder can be defined as the solution to the following SOCP

$$\mathbf{W}_{\text{Mm-ZF}} = \underset{\mathbf{W} \in \mathbb{C}^{K \times L}}{\text{argmin}} \; \underset{k \in \{1, \ldots, K\}}{\max} \; P_k \qquad \text{s.t. } \mathbf{HW} = \mathbf{I}_L. \qquad (4.3)$$

This precoder was first proposed in [69]. It is also similar to that in [78], which minimizes the maximum per-chain power subject to individual signal-to-interference-and-noise ratio (SINR) constraints at each user.
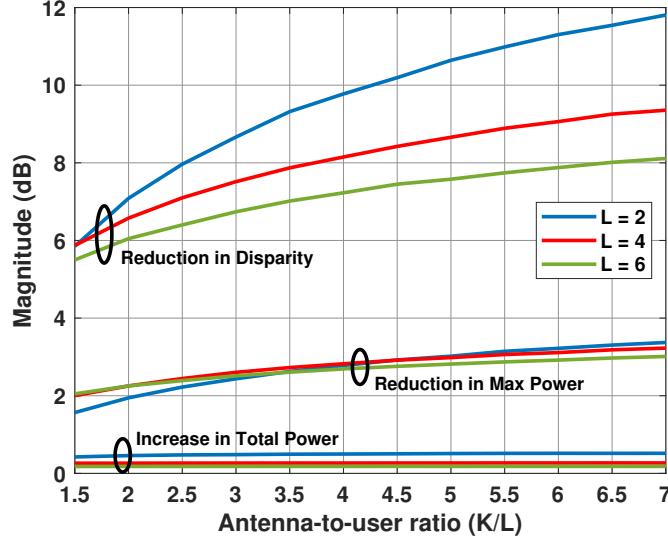
Figure 4.1: The differences in average-power levels due to utilizing the EP-MRT precoder instead of the conventional MRT precoder.

In the majority of cases, especially for large K/L ratios, the minimax ZF precoder results in equal average-power levels across all chains, but may not always do so. Equal average-power levels can be enforced by regularizing the ZF condition. Accordingly, an EP regularized zero-forcing (RZF) precoder can be defined as

$$\{\mathbf{W}_{\text{EP-RZF}}, t_{\text{EP-RZF}}\} = \underset{\mathbf{W} \in \mathbb{C}^{K \times L}, t \in \mathbb{R}_+}{\operatorname{argmin}} \|\mathbf{H}\mathbf{W} - \mathbf{I}_L\|_F^2 + \lambda t \qquad \text{s.t. } P_k = t \ \forall k. \qquad (4.4)$$

where $\lambda \in \mathbb{R}_+$ is a regularization parameter. Obtaining near-ZF performance requires choosing a small λ, but not too small that it causes numerical instability. Unlike the problem in (4.3), the problem defined above is non-convex because of the quadratic equality constraints. Nevertheless, it can be solved using the method of Lagrange multipliers [79]. The Lagrangian function is given by

$$\mathcal{L}(\mathbf{W}, t, \mu_1, \ldots, \mu_K) = \|\mathbf{H}\mathbf{W} - \mathbf{I}_L\|_F^2 + \lambda t + \sum_{k=1}^{K} \mu_k (\mathbf{e}_k^T \mathbf{W} \, \mathbf{\Xi} \, \mathbf{W}^H \mathbf{e}_k - t), \qquad (4.5)$$

where the matrix form of (2.27) was utilized. Using the following identities [80]

$$\|\mathbf{H}\mathbf{W} - \mathbf{I}_L\|_F^2 = \|\mathbf{C}\mathbf{w} - \text{vec}(\mathbf{I}_L)\|^2$$
$$\mathbf{e}_k^T \mathbf{W} \, \mathbf{\Xi} \, \mathbf{W}^H \mathbf{e}_k = \mathbf{w}^H \mathbf{B}_k \mathbf{w}, \qquad (4.6)$$

53

where

$$\mathbf{w} = \mathrm{vec}(\mathbf{W})$$
$$\mathbf{C} = \mathbf{I}_L \otimes \mathbf{H}$$
$$\mathbf{B}_k = \mathbf{\Xi} \otimes \mathbf{e}_k \mathbf{e}_k^T \ \forall k,$$

the Lagrangian in (4.5) can be rewritten as

$$\mathcal{L}(\mathbf{w}, t, \mu_1, \ldots, \mu_K) = \|\mathbf{C}\mathbf{w} - \mathrm{vec}(\mathbf{I}_L)\|^2 + \lambda t + \sum_{k=1}^K \mu_k(\mathbf{w}^H \mathbf{B}_k \mathbf{w} - t). \qquad (4.7)$$

Note that quadratic forms $\mathbf{w}^H \mathbf{B}_k \mathbf{w} \ \forall k$ possess no imaginary part since the $\mathbf{B}_k$ matrices are real-valued. The Lagrangian function can be expressed in terms of only real-valued parameters as

$$\mathcal{L}(\mathbf{w}_R, \mathbf{w}_I, t, \mu_1, \ldots, \mu_K) = \|\mathbf{C}_R \mathbf{w}_R - \mathbf{C}_I \mathbf{w}_I - \mathrm{vec}(\mathbf{I}_L)\|^2 + \|\mathbf{C}_I \mathbf{w}_R + \mathbf{C}_R \mathbf{w}_I\|^2 + \lambda t$$

$$+ \sum_{k=1}^K \mu_k(\mathbf{w}_R^T \mathbf{B}_k \mathbf{w}_R + \mathbf{w}_I^T \mathbf{B}_k \mathbf{w}_I - t), \qquad (4.8)$$

where

$$\mathbf{w}_R = \mathrm{Re}\{\mathbf{w}\}, \quad \mathbf{w}_I = \mathrm{Im}\{\mathbf{w}\},$$
$$\mathbf{C}_R = \mathrm{Re}\{\mathbf{C}\}, \quad \mathbf{C}_I = \mathrm{Im}\{\mathbf{C}\}.$$

A stationary point of the Lagrangian can then be found by setting its derivatives to zero and solving the resultant system of equations:

$$\frac{1}{2}\frac{\partial \mathcal{L}}{\partial \mathbf{w}_R} = \mathbf{C}_R^T(\mathbf{C}_R \mathbf{w}_R - \mathbf{C}_I \mathbf{w}_I - \mathrm{vec}(\mathbf{I}_L)) + \mathbf{C}_I^T(\mathbf{C}_I \mathbf{w}_R + \mathbf{C}_R \mathbf{w}_I)$$

$$+ \sum_{k=1}^K \mu_k \mathbf{B}_k \mathbf{w}_R = \mathbf{0}_{(KL) \times 1}$$

$$\frac{1}{2}\frac{\partial \mathcal{L}}{\partial \mathbf{w}_I} = -\mathbf{C}_I^T(\mathbf{C}_R \mathbf{w}_R - \mathbf{C}_I \mathbf{w}_I - \mathrm{vec}(\mathbf{I}_L)) + \mathbf{C}_R^T(\mathbf{C}_I \mathbf{w}_R + \mathbf{C}_R \mathbf{w}_I)$$

$$+ \sum_{k=1}^K \mu_k \mathbf{B}_k \mathbf{w}_I = \mathbf{0}_{(KL) \times 1}$$

$$\frac{\partial \mathcal{L}}{\partial t} = \lambda - \sum_{k=1}^K \mu_k = 0$$

$$\frac{\partial \mathcal{L}}{\partial \mu_k} = \mathbf{w}_R^T \mathbf{B}_k \mathbf{w}_R + \mathbf{w}_I^T \mathbf{B}_k \mathbf{w}_I - t = 0 \quad \forall k. \qquad (4.9)$$

Note that standard vector differentiation rules were utilized [80].

The set of $2KL + K + 1$ nonlinear equations in (4.9) can be iteratively solved for the variables $(\mathbf{w}_R, \mathbf{w}_I, t, \mu_1, \ldots, \mu_K)$ using Newton's trust-region methods [79]. For this, we define the set of functions $f_i(\mathbf{w}_R, \mathbf{w}_I, t, \mu_1, \ldots, \mu_K), i = 1 \ldots, 2KL + K + 1$ as

$$\begin{bmatrix} f_1(.) \\ \vdots \\ f_{KL}(.) \end{bmatrix} = \frac{1}{2} \frac{\partial L}{\partial \mathbf{w}_R}$$

$$\begin{bmatrix} f_{KL+1}(.) \\ \vdots \\ f_{2KL}(.) \end{bmatrix} = \frac{1}{2} \frac{\partial L}{\partial \mathbf{w}_I}$$

$$f_{2KL+1}(.) = \frac{\partial L}{\partial t}$$

$$\begin{bmatrix} f_{2KL+2}(.) \\ \vdots \\ f_{2KL+K+1}(.) \end{bmatrix} = \begin{bmatrix} \dfrac{\partial L}{\partial \mu_1} \\ \vdots \\ \dfrac{\partial L}{\partial \mu_K} \end{bmatrix}. \tag{4.10}$$

Finding the solution to the system of equations $f_i(.) = 0, i = 1 \ldots, 2KL + K + 1$ requires evaluating the Jacobian matrix of derivatives [79]. In Appendix B, we show that the Jacobian matrix for the set of functions in (4.10) is given by

$$\mathbf{J}(.) = \begin{bmatrix} \dfrac{\partial f_1}{\partial \mathbf{w}_R^T} & \dfrac{\partial f_1}{\partial \mathbf{w}_I^T} & \dfrac{\partial f_1}{\partial t} & \dfrac{\partial f_1}{\partial \mu_1} & \cdots & \dfrac{\partial f_1}{\partial \mu_K} \\ \vdots & \vdots & \vdots & \vdots & & \vdots \\ \dfrac{\partial f_{2KL+K+1}}{\partial \mathbf{w}_R^T} & \dfrac{\partial f_{2KL+K+1}}{\partial \mathbf{w}_I^T} & \dfrac{\partial f_{2KL+K+1}}{\partial t} & \dfrac{\partial f_{2KL+K+1}}{\partial \mu_1} & \cdots & \dfrac{\partial f_{2KL+K+1}}{\partial \mu_K} \end{bmatrix}$$

$$= \begin{bmatrix} \mathbf{C}_R^T \mathbf{C}_R + \mathbf{C}_I^T \mathbf{C}_I + \mathbf{A} & -\mathbf{C}_R^T \mathbf{C}_I + \mathbf{C}_I^T \mathbf{C}_R & \mathbf{0}_{(KL) \times 1} & \mathbf{B}_1 \mathbf{w}_R & \ldots & \mathbf{B}_K \mathbf{w}_R \\ -\mathbf{C}_I^T \mathbf{C}_R + \mathbf{C}_R^T \mathbf{C}_I & \mathbf{C}_I^T \mathbf{C}_I + \mathbf{C}_R^T \mathbf{C}_R + \mathbf{A} & \mathbf{0}_{(KL) \times 1} & \mathbf{B}_1 \mathbf{w}_I & \ldots & \mathbf{B}_K \mathbf{w}_I \\ \mathbf{0}_{1 \times (KL)} & \mathbf{0}_{1 \times (KL)} & 0 & -1 & \ldots & -1 \\ 2\, \mathbf{w}_R^T \mathbf{B}_1 & 2\, \mathbf{w}_I^T \mathbf{B}_1 & -1 & 0 & \ldots & 0 \\ \vdots & \vdots & \vdots & \vdots & \ddots & \vdots \\ 2\, \mathbf{w}_R^T \mathbf{B}_K & 2\, \mathbf{w}_I^T \mathbf{B}_K & -1 & 0 & \ldots & 0 \end{bmatrix}, \tag{4.11}$$

where

$$\mathbf{A} = \sum_{k=1}^{K} \mu_k \mathbf{B}_k = \sum_{k=1}^{K} \mu_k(\boldsymbol{\Xi} \otimes \mathbf{e}_k \mathbf{e}_k^T) = \boldsymbol{\Xi} \otimes \mathrm{diag}\left(\begin{bmatrix} \mu_1 & \dots & \mu_K \end{bmatrix}\right).$$

The system of equations in (4.10), and its Jacobian in (4.11), are used to iteratively compute the EP-RZF precoder. Finally, an initial guess at the solution can be obtained by dropping the equality constraints in (4.4), i.e.,

$$\mathbf{W}^0 = \underset{\mathbf{W} \in \mathbb{C}^{K \times L}}{\mathrm{argmin}} \left(\|\mathbf{HW} - \mathbf{I}_L\|_F^2 + \frac{\lambda}{K} \|\mathbf{W}\|_F^2 \right)$$

$$= \mathbf{H}^H \left(\mathbf{HH}^H + \frac{\lambda}{K} \mathbf{I}_L \right)^{-1}. \tag{4.12}$$

The solution to the optimization problem in (4.12) can be found in [75, Section 6.1.4]. The initial estimates of the parameters $(\mathbf{w}_R, \mathbf{w}_I, t, \mu_1, \dots, \mu_K)$ are then

$$\mathbf{w}_R^0 = \mathrm{Re}\left\{\mathrm{vec}(\mathbf{W}^0)\right\}, \qquad\qquad t^0 = \frac{\|\mathbf{W}^0\|_F^2}{K},$$

$$\mathbf{w}_I^0 = \mathrm{Im}\left\{\mathrm{vec}(\mathbf{W}^0)\right\}, \qquad\qquad \mu_k^0 = \frac{\lambda}{K} \ \forall k, \tag{4.13}$$

where the estimates of $\mu_1, \dots, \mu_K$ were obtained from the definition of $\partial \mathcal{L}/\partial t$ in (4.9).

Using the same simulation settings in the previous subsection and $\lambda = 10^{-4}$, the power distribution differences between the EP-RZF and conventional ZF precoders were simulated and averaged across 10^5 channel realizations. The results, depicted in Fig. 4.2, show a similar trend to the MRT results in Fig 4.1. In addition, the average ZF error $\frac{1}{L^2}\|\mathbf{HW}_{\mathrm{EP-RZF}} - \mathbf{I}_L\|_F^2$ was evaluated, and is displayed in Fig. 4.3. The figure shows that the performance loss associated with regularization is negligible for $K/L \geq 2$.

4.1.3 MMSE

Under a fixed per-chain power level τ, an EP-MMSE precoder can be defined by modifying the MMSE precoding problem in (2.33), i.e.,

$$\{\mathbf{W}_{\mathrm{EP-MMSE}}, \beta_{\mathrm{EP-MMSE}}\} = \underset{\mathbf{W} \in \mathbb{C}^{K \times L}, \beta \in \mathbb{R}_+}{\mathrm{argmin}} \quad \mathbb{E}\left[\left\|\mathbf{v}[n] - \beta^{-1}\boldsymbol{\Xi}^{-\frac{1}{2}}\mathbf{u}[n]\right\|^2\right]$$

$$\text{s.t.} \qquad P_k = \tau \ \forall k. \tag{4.14}$$
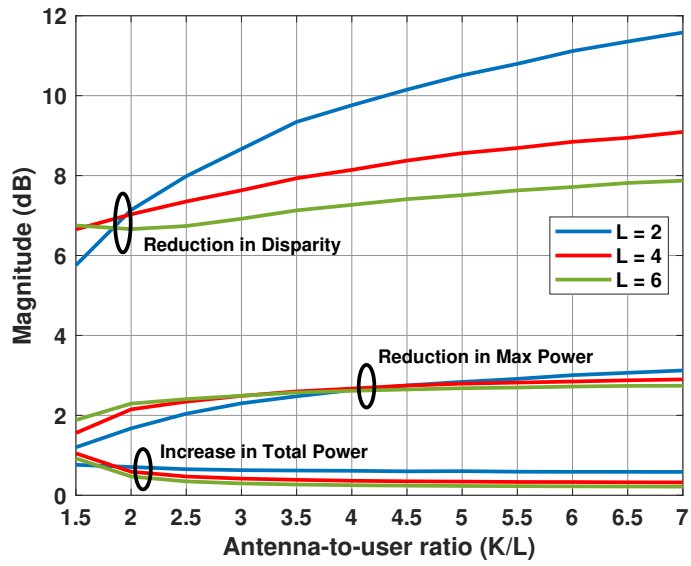
Figure 4.2: The differences in average-power levels due to utilizing the EP-RZF precoder instead of the conventional ZF precoder.
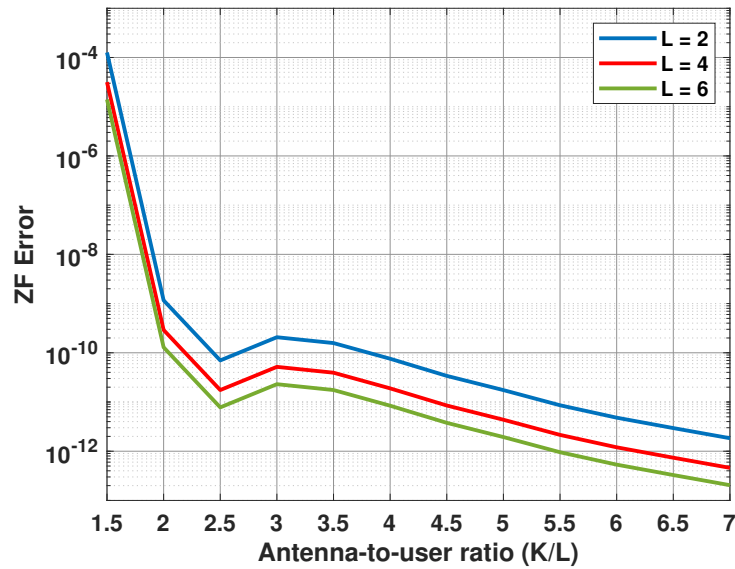

Figure 4.3: The average ZF error due to the utilization of the EP-RZF precoder.

The objective function in (4.14) can be simplified as follows

$$\mathbb{E}\left[\left\|\mathbf{v}[n] - \beta^{-1}\boldsymbol{\Xi}^{-\frac{1}{2}}\mathbf{u}[n]\right\|^2\right]$$

$$= \mathbb{E}\left[\left\|\mathbf{v}[n] - \beta^{-1}\boldsymbol{\Xi}^{-\frac{1}{2}}(\mathbf{HW}\boldsymbol{\Xi}^{\frac{1}{2}}\mathbf{v}[n] + \boldsymbol{\eta}[n])\right\|^2\right]$$

$$= \mathbb{E}\left[\mathrm{tr}\left(\mathbf{v}[n]\mathbf{v}^H[n] - 2\,\beta^{-1}\mathrm{Re}\left\{\boldsymbol{\Xi}^{-\frac{1}{2}}\mathbf{HW}\boldsymbol{\Xi}^{\frac{1}{2}}\mathbf{v}[n]\mathbf{v}^H[n]\right\}\right.\right.$$

$$\left.\left.+ \beta^{-2}\left[\boldsymbol{\Xi}^{-\frac{1}{2}}\mathbf{HW}\boldsymbol{\Xi}^{\frac{1}{2}}\mathbf{v}[n]\mathbf{v}^H[n]\boldsymbol{\Xi}^{\frac{1}{2}}\mathbf{W}^H\mathbf{H}^H\boldsymbol{\Xi}^{-\frac{1}{2}} + \boldsymbol{\Xi}^{-\frac{1}{2}}\boldsymbol{\eta}[n]\boldsymbol{\eta}^H[n]\boldsymbol{\Xi}^{-\frac{1}{2}}\right]\right)\right]$$

$$= L + \beta^{-1}\mathrm{tr}\left(\beta^{-1}\left[\boldsymbol{\Xi}^{-1}\mathbf{HW}\,\boldsymbol{\Xi}\,\mathbf{W}^H\mathbf{H}^H + \sigma^2\boldsymbol{\Xi}^{-1}\right] - 2\,\mathrm{Re}\{\mathbf{HW}\}\right), \qquad (4.15)$$

where we have utilized the facts $\mathbb{E}\left[\mathbf{v}[n]\mathbf{v}^H[n]\right] = \mathbf{I}_L$ and $\mathbb{E}\left[\boldsymbol{\eta}[n]\boldsymbol{\eta}^H[n]\right] = \sigma^2\mathbf{I}_L$, and the cyclic properties of the trace operator. Using (4.15) and the matrix form of (2.27), the Lagrangian function of the problem in (4.14) is then

$$\mathcal{L}(\mathbf{W}, \beta, \mu_1, \ldots, \mu_K) = L + \beta^{-1}\mathrm{tr}\left(\beta^{-1}\left[\boldsymbol{\Xi}^{-1}\mathbf{HW}\,\boldsymbol{\Xi}\,\mathbf{W}^H\mathbf{H}^H + \sigma^2\boldsymbol{\Xi}^{-1}\right] - 2\,\mathrm{Re}\{\mathbf{HW}\}\right)$$

$$+ \sum_{k=1}^{K}\mu_k(\mathbf{e}_k^T\mathbf{W}\,\boldsymbol{\Xi}\,\mathbf{W}^H\mathbf{e}_k - \tau). \qquad (4.16)$$

Using the following identities [80]

$$\mathrm{tr}(\boldsymbol{\Xi}^{-1}\mathbf{HW}\,\boldsymbol{\Xi}\,\mathbf{W}^H\mathbf{H}^H) = \mathbf{w}^H\mathbf{Q}\mathbf{w}$$
$$\mathbf{e}_k^T\mathbf{W}\,\boldsymbol{\Xi}\,\mathbf{W}^H\mathbf{e}_k = \mathbf{w}^H\mathbf{B}_k\mathbf{w}$$
$$\mathrm{tr}(\mathbf{HW}) = \mathbf{h}^T\mathbf{w}, \qquad (4.17)$$

where

$$\mathbf{w} = \mathrm{vec}(\mathbf{W}), \qquad\qquad \mathbf{Q} = \boldsymbol{\Xi} \otimes (\mathbf{H}^H\boldsymbol{\Xi}^{-1}\mathbf{H}),$$
$$\mathbf{h} = \mathrm{vec}(\mathbf{H}^T), \qquad\qquad \mathbf{B}_k = \boldsymbol{\Xi} \otimes \mathbf{e}_k\mathbf{e}_k^T \quad \forall k,$$

the Lagrangian in (4.16) can be rewritten as

$$\mathcal{L}(\mathbf{w}, \beta, \mu_1, \ldots, \mu_K) = L + \beta^{-2}(\mathbf{w}^H\mathbf{Q}\mathbf{w} + \sigma^2\mathrm{tr}(\boldsymbol{\Xi}^{-1})) - 2\beta^{-1}\mathrm{Re}\{\mathbf{h}^T\mathbf{w}\}$$

$$+ \sum_{k=1}^{K}\mu_k(\mathbf{w}^H\mathbf{B}_k\mathbf{w} - \gamma). \qquad (4.18)$$

Note that quadratic form $\mathbf{w}^H\mathbf{Q}\mathbf{w}$ is real-valued since $\mathbf{Q}$ is Hermitian (i.e., $\mathbf{Q}^H = \mathbf{Q}$). The Lagrangian function can be expressed in terms of only real-valued parameters as

$$\mathcal{L}(\mathbf{w}_R, \mathbf{w}_I, \beta, \mu_1, \ldots, \mu_K) = L + \beta^{-2}\left(\mathbf{w}_R^T\mathbf{Q}_R\mathbf{w}_R + \mathbf{w}_I^T\mathbf{Q}_R\mathbf{w}_I + 2\mathbf{w}_I^T\mathbf{Q}_I\mathbf{w}_R + \sigma^2\mathrm{tr}(\mathbf{\Xi}^{-1})\right)$$

$$- 2\beta^{-1}(\mathbf{h}_R^T\mathbf{w}_R - \mathbf{h}_I^T\mathbf{w}_I) + \sum_{k=1}^{K}\mu_k(\mathbf{w}_R^T\mathbf{B}_k\mathbf{w}_R + \mathbf{w}_I^T\mathbf{B}_k\mathbf{w}_I - \tau),$$

$$(4.19)$$

where

$$\mathbf{w}_R = \mathrm{Re}\{\mathbf{w}\}, \quad \mathbf{w}_I = \mathrm{Im}\{\mathbf{w}\},$$
$$\mathbf{h}_R = \mathrm{Re}\{\mathbf{h}\}, \quad \mathbf{h}_I = \mathrm{Im}\{\mathbf{h}\},$$
$$\mathbf{Q}_R = \mathrm{Re}\{\mathbf{Q}\}, \quad \mathbf{Q}_I = \mathrm{Im}\{\mathbf{Q}\}.$$

Note that, since $\mathbf{Q}^H = \mathbf{Q}$, we have $\mathbf{Q}_R^T = \mathbf{Q}_R$ and $\mathbf{Q}_I^T = -\mathbf{Q}_I$. A stationary point of the Lagrangian can be found by setting its derivatives to zero and solving the resultant system of equations:

$$\frac{1}{2}\beta^2\frac{\partial\mathcal{L}}{\partial\mathbf{w}_R} = \mathbf{Q}_R\mathbf{w}_R - \mathbf{Q}_I\mathbf{w}_I - \beta\,\mathbf{h}_R + \beta^2\sum_{k=1}^{K}\mu_k\mathbf{B}_k\mathbf{w}_R = \mathbf{0}_{(KL)\times 1}$$

$$\frac{1}{2}\beta^2\frac{\partial\mathcal{L}}{\partial\mathbf{w}_I} = \mathbf{Q}_R\mathbf{w}_I + \mathbf{Q}_I\mathbf{w}_R + \beta\,\mathbf{h}_I + \beta^2\sum_{k=1}^{K}\mu_k\mathbf{B}_k\mathbf{w}_I = \mathbf{0}_{(KL)\times 1}$$

$$\frac{1}{2}\beta^3\frac{\partial\mathcal{L}}{\partial\beta} = \beta(\mathbf{h}_R^T\mathbf{w}_R - \mathbf{h}_I^T\mathbf{w}_I) - \mathbf{w}_R^T\mathbf{Q}_R\mathbf{w}_R + \mathbf{w}_I^T\mathbf{Q}_R\mathbf{w}_I + 2\mathbf{w}_I^T\mathbf{Q}_I\mathbf{w}_R + \sigma^2\mathrm{tr}(\mathbf{\Xi}^{-1}) = 0$$

$$\frac{\partial\mathcal{L}}{\partial\mu_k} = \mathbf{w}_R^T\mathbf{B}_k\mathbf{w}_R + \mathbf{w}_I^T\mathbf{B}_k\mathbf{w}_I - \gamma = 0 \quad \forall k. \tag{4.20}$$

To compute the EP-MMSE precoder, the set of $2KL + K + 1$ nonlinear equations in (4.20) need to be iteratively solved for the optimal variables using Newton's trust-region methods. For this, we define the set of functions $f_i(\mathbf{w}_R, \mathbf{w}_I, \beta, \mu_1, \ldots, \mu_K), i =$

$1 \ldots, 2KL + K + 1$ as

$$\begin{bmatrix} f_1(.) \\ \vdots \\ f_{KL}(.) \end{bmatrix} = \frac{1}{2}\beta^2 \frac{\partial L}{\partial \mathbf{w}_R}$$

$$\begin{bmatrix} f_{KL+1}(.) \\ \vdots \\ f_{2KL}(.) \end{bmatrix} = \frac{1}{2}\beta^2 \frac{\partial L}{\partial \mathbf{w}_I}$$

$$f_{2KL+1}(.) = \frac{1}{2}\beta^3 \frac{\partial L}{\partial \beta}$$

$$\begin{bmatrix} f_{2KL+2}(.) \\ \vdots \\ f_{2KL+K+1}(.) \end{bmatrix} = \begin{bmatrix} \dfrac{\partial L}{\partial \mu_1} \\ \vdots \\ \dfrac{\partial L}{\partial \mu_K} \end{bmatrix} \qquad (4.21)$$

In Appendix B, we show that the Jacobian matrix for the set of functions $f_i(.) = 0, i = 1 \ldots, 2KL + K + 1$ in (4.21) is given by

$$\mathbf{J}(.) = \begin{bmatrix} \dfrac{\partial f_1}{\partial \mathbf{w}_R^T} & \dfrac{\partial f_1}{\partial \mathbf{w}_I^T} & \dfrac{\partial f_1}{\partial \beta} & \dfrac{\partial f_1}{\partial \mu_1} & \cdots & \dfrac{\partial f_1}{\partial \mu_K} \\ \vdots & \vdots & \vdots & \vdots & & \vdots \\ \dfrac{\partial f_{2KL+K+1}}{\partial \mathbf{w}_R^T} & \dfrac{\partial f_{2KL+K+1}}{\partial \mathbf{w}_I^T} & \dfrac{\partial f_{2KL+K+1}}{\partial \beta} & \dfrac{\partial f_{2KL+K+1}}{\partial \mu_1} & \cdots & \dfrac{\partial f_{2KL+K+1}}{\partial \mu_K} \end{bmatrix}$$

$$= \begin{bmatrix} \mathbf{Q}_R + \beta^2 \mathbf{A} & -\mathbf{Q}_I & -\mathbf{h}_R + 2\beta \mathbf{A}\mathbf{w}_R & \beta^2 \mathbf{B}_1 \mathbf{w}_R & \cdots & \beta^2 \mathbf{B}_K \mathbf{w}_R \\ \mathbf{Q}_I & \mathbf{Q}_R + \beta^2 \mathbf{A} & \mathbf{h}_I + 2\beta \mathbf{A}\mathbf{w}_I & \beta^2 \mathbf{B}_1 \mathbf{w}_I & \cdots & \beta^2 \mathbf{B}_K \mathbf{w}_I \\ \beta \, \mathbf{h}_R^T - 2\,\mathbf{w}_R^T \mathbf{Q}_R - 2\,\mathbf{w}_I^T \mathbf{Q}_I & -\beta \, \mathbf{h}_I^T - 2\,\mathbf{w}_I^T \mathbf{Q}_R + 2\,\mathbf{w}_R^T \mathbf{Q}_I & \mathbf{h}_R^T \mathbf{w}_R - \mathbf{h}_I^T \mathbf{w}_I & 0 & \cdots & 0 \\ 2\,\mathbf{w}_R^T \mathbf{B}_1 & 2\,\mathbf{w}_I^T \mathbf{B}_1 & 0 & 0 & \cdots & 0 \\ \vdots & \vdots & \vdots & \vdots & \ddots & \vdots \\ 2\,\mathbf{w}_R^T \mathbf{B}_K & 2\,\mathbf{w}_I^T \mathbf{B}_K & 0 & 0 & \cdots & 0 \end{bmatrix}$$

$$(4.22)$$

where

$$\mathbf{A} = \sum_{k=1}^{K} \mu_k \mathbf{B}_k = \sum_{k=1}^{K} \mu_k (\mathbf{\Xi} \otimes \mathbf{e}_k \mathbf{e}_k^T) = \mathbf{\Xi} \otimes \mathrm{diag}\left(\begin{bmatrix} \mu_1 & \cdots & \mu_K \end{bmatrix}\right).$$

The conventional MMSE precoder in (2.34) with $P_{tot} = K\tau$ can be used as an initial guess at the solution and the Lagrangian multipliers can initially be set to zero, i.e., $\mu_k^0 = 0 \; \forall k$.

The power distribution differences between the EP and conventional MMSE precoders are similar to those shown in Figs. 4.1 and 4.2. Finally, it is worthwhile comparing the performance of the three proposed EP precoders under a fixed maximum per-chain power level τ. Note that the EP-MRT and EP-RZF precoders are not defined under a fixed power level. Hence, they must be scaled to ensure that $P_k = \tau \; \forall k$. The performance of the different precoders is assessed by evaluating the average SINR at the users' side. Given the precoding and channel matrices $\mathbf{W}, \mathbf{H}$, the SINR at the lth user (in dB) is given by

$$10 \log_{10} \left(\frac{\xi_l \left| (\mathbf{HW})_{l,l} \right|^2}{\sum_{m \neq l} \xi_m \left| (\mathbf{HW})_{l,m} \right|^2 + \sigma^2} \right).$$

The average user's SINR is plotted in Fig. 4.4 versus the ratio of the total basestation power to the noise power, i.e., $K\tau/\sigma^2$, for $L = 4, K = 12, \boldsymbol{\Xi} = \mathbf{I}_L$ and $\lambda = 10^{-4}$. As expected, the MMSE precoder has the best performance under any SNR scenario. Furthermore, since the K/L ratio is large and λ is close to zero, the EP-RZF precoder is indistinguishable from the minimax ZF precoder.
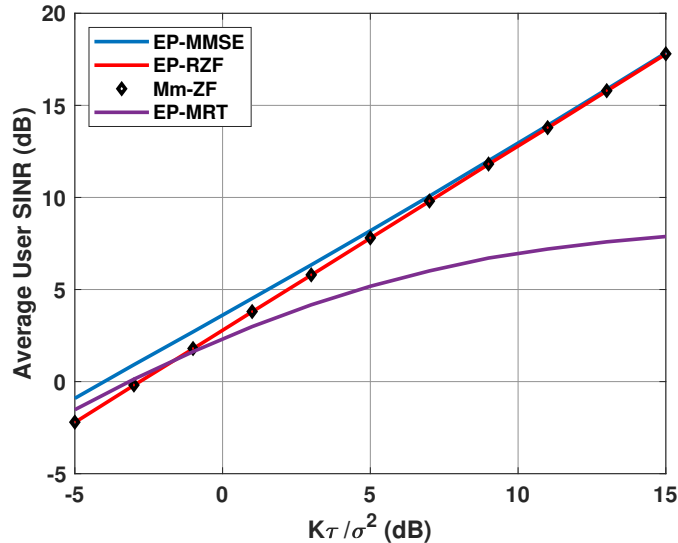

Figure 4.4: Comparison between the proposed EP precoders given a fixed maximum per-chain power level τ for $L = 4, K = 12$, and $\boldsymbol{\Xi} = \mathbf{I}_L$.

4.2 The Average Active Impedances under EP Precoding

If all chains are transmitting the same average power, the crosstalk-induced load deviation becomes restricted within a circular boundary on the Smith chart. The maximum load deviation at the kth antenna port at any frequency can be calculated by rearranging the formula for the average active reflection coefficient in (3.6) as

$$\bar{\Gamma}_k^{\mathrm{EP}}(f) - S_{kk}(f) = \frac{\sum_{i \neq k} S_{ki}(f) \, \underline{\mathbf{w}}_i \mathbf{\Xi} \underline{\mathbf{w}}_k^H}{\underline{\mathbf{w}}_k \mathbf{\Xi} \underline{\mathbf{w}}_k^H} \tag{4.23}$$

Taking the absolute value of both sides yields

$$
\begin{aligned}
\left| \bar{\Gamma}_k^{\mathrm{EP}}(f) - S_{kk}(f) \right| &= \left| \frac{\sum_{i \neq k} S_{ki}(f) \, \underline{\mathbf{w}}_i \mathbf{\Xi} \underline{\mathbf{w}}_k^H}{\underline{\mathbf{w}}_k \mathbf{\Xi} \underline{\mathbf{w}}_k^H} \right| \\
&\overset{(a)}{\leq} \frac{\sum_{i \neq k} |S_{ki}(f)| \, \left| \underline{\mathbf{w}}_i \mathbf{\Xi} \underline{\mathbf{w}}_k^H \right|}{\left| \underline{\mathbf{w}}_k \mathbf{\Xi} \underline{\mathbf{w}}_k^H \right|} \\
&\overset{(b)}{\leq} \frac{\sum_{i \neq k} |S_{ki}(f)| \, \sqrt{\left| \underline{\mathbf{w}}_i \mathbf{\Xi} \underline{\mathbf{w}}_i^H \right| \left| \underline{\mathbf{w}}_k \mathbf{\Xi} \underline{\mathbf{w}}_k^H \right|}}{\left| \underline{\mathbf{w}}_k \mathbf{\Xi} \underline{\mathbf{w}}_k^H \right|} \\
&\overset{(c)}{=} \frac{\sum_{i \neq k} |S_{ki}(f)| \, \sqrt{P_i P_k}}{P_k} \\
&\overset{(d)}{=} \sum_{i \neq k} |S_{ki}(f)|, \tag{4.24}
\end{aligned}
$$

where (a) follows from the triangle inequality, (b) from the Cauchy-Schwarz inequality, (c) from (2.27), and (d) from the fact that $P_i = P_k \ \forall \, i, k$ under EP precoding. This limit corresponds to a circle of radius $\sum_{i \neq k} |S_{ki}(f)|$ around the nominal reflection coefficient value $S_{kk}(f)$.

Using the same simulation settings and channel realizations in Section 3.2, the average active impedances for the array in Fig. 3.2 under both conventional ZF and the proposed EP-RZF precoding were evaluated and plotted as the blue and red crosses in Fig. 4.5 respectively. The red circles in the figure indicate the maximum load deviation under EP precoding as given by (4.24). As the results show, EP precoding significantly reduces the extent of load modulation through forcing all chains to transmit the same average power.
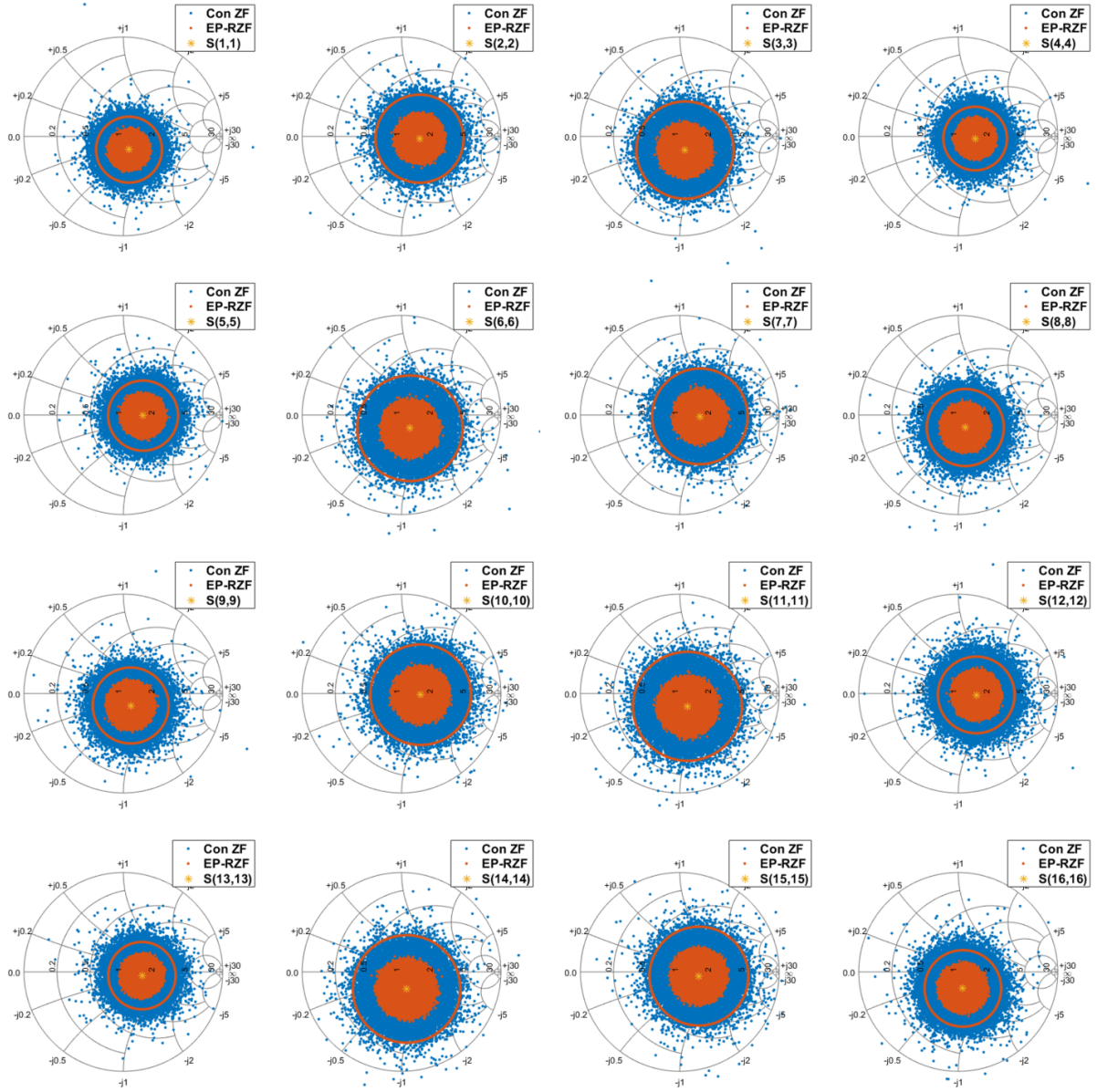
Figure 4.5: The average active impedances for the array in Fig. 3.2 under both conventional ZF and the proposed EP-RZF precoder. The red circles indicate the maximum load deviation under EP precoding as per (4.24).

4.3 Experimental Validation

The effectiveness of the proposed EP precoders is now validated through measurements on the 2-user 4-chain setup used in Section 3.5. In a 2-user 4-chain system, the EP-RZF precoder requires, on average, about 1.7 dB less maximum per-chain power than the conventional ZF precoder does to deliver the same power to the users (see Fig. 4.2). In order to fully utilize the PAs' transmission capability, the EP-RZF precoder can be normalized so that the per-chain power level is the same as the max level required by the conventional ZF precoder. This increases the power delivered to the users at the expense of operating the PAs in a more nonlinear region. Nevertheless, as will be shown below, the proposed EP precoders improve the performance of the DPD subsystem and consequently, enable higher power delivery without violating signal quality requirements.

The DPD modules were trained using four independently generated 100-MHz OFDM signals with 9-dB PAPR, resulting in only one coefficient set per PA. The dual-input DPD parameters in (3.17)-(3.19) were set to $P = 5$, $M = 1$, and $Q = 3$, and the SISO parameters were set to $N = 8$ and $M_S = 6$. Once DPD training had been performed, the full setup was run 200 times. Each time, two 100-MHz OFDM signals and a Rayleigh channel matrix were randomly generated, and both conventional ZF and normalized EP-RZF precoding were applied to the two user signals. Fig. 4.6 shows the RNMSE and upper-side ACPR values obtained in the four chains at each measurement run, and Fig. 4.7 shows the average active impedances at the center frequency (3.5 GHz) across these runs. Because of the large number of channel realizations plotted in Fig. 4.7, it is not possible to label all loads with their corresponding measurement indices. Hence, only a few interesting cases were labeled. The red circles in the figure indicate the maximum load deviation limits under EP precoding, which were calculated using (4.24).

When compared with the conventional precoders, the proposed ones can significantly reduce load modulation effects since they eliminate the relative variation in average-power levels across chains. As shown in Fig. 4.6, the EP-RZF precoder reduced the ACPR and RNMSE in each chain by up to 10 dB and 12% respectively, all while delivering 1.7 dB more power to the users on average. Fig. 4.8 shows the RNMSE at the two user terminals, where it can be seen that the EP-RZF precoder reduced the RNMSE experienced by users 1 and 2 by up to 3% and 7% respectively. It is worthy of note that the RNMSE reductions brought by the EP precoder at the user side are less significant than those at the individual PA outputs. This is because the signal at any user terminal is a linear combination of the PA output signals and not all PAs experience RNMSE degradation at the same time. Nevertheless, the proposed EP precoders ensure that user-side signal quality requirements are met across all channel conditions. More importantly, the proposed

64

precoders stabilize the transmitter's RF performance and guard against crosstalk-induced PA instability, which could result in uncontrollable oscillations. Furthermore, the proposed precoders reduce the required maximum per-chain power level (see Figs. 4.1 and 4.2), which enables the use of smaller PAs and improves the energy efficiency of the MIMO transmitter.

4.4 Discussion

The improvements in power distribution obtained with EP precoding are substantially bigger than those obtained with the low-complexity method in Section 3.3.1, as evident from comparing Figs. 4.2 and 3.5. However, this comes at the expense of a substantial increase
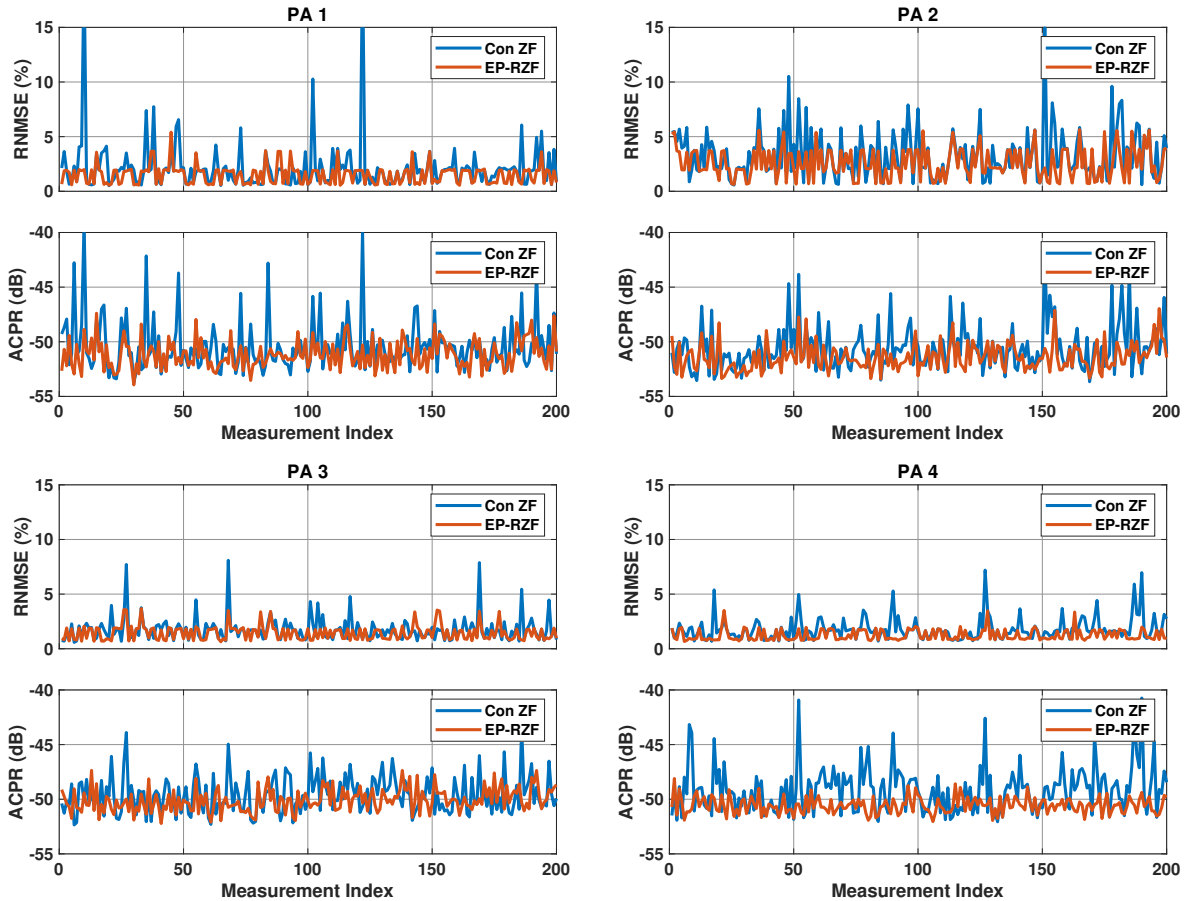
Figure 4.6: The measured RNMSE and ACPR values across 200 channel realizations.

in complexity since computing any of the EP precoders entails solving a system of nonlinear equations. For instance, the EP-RZF precoder can be computed by iteratively solving the system in (4.10), where each iteration involves obtaining an approximate solution to $\mathbf{J}(.)\mathbf{x} = -\mathbf{f}(.)$ using Steihaug's conjugate gradient method [79]. Since the Jacobian matrix
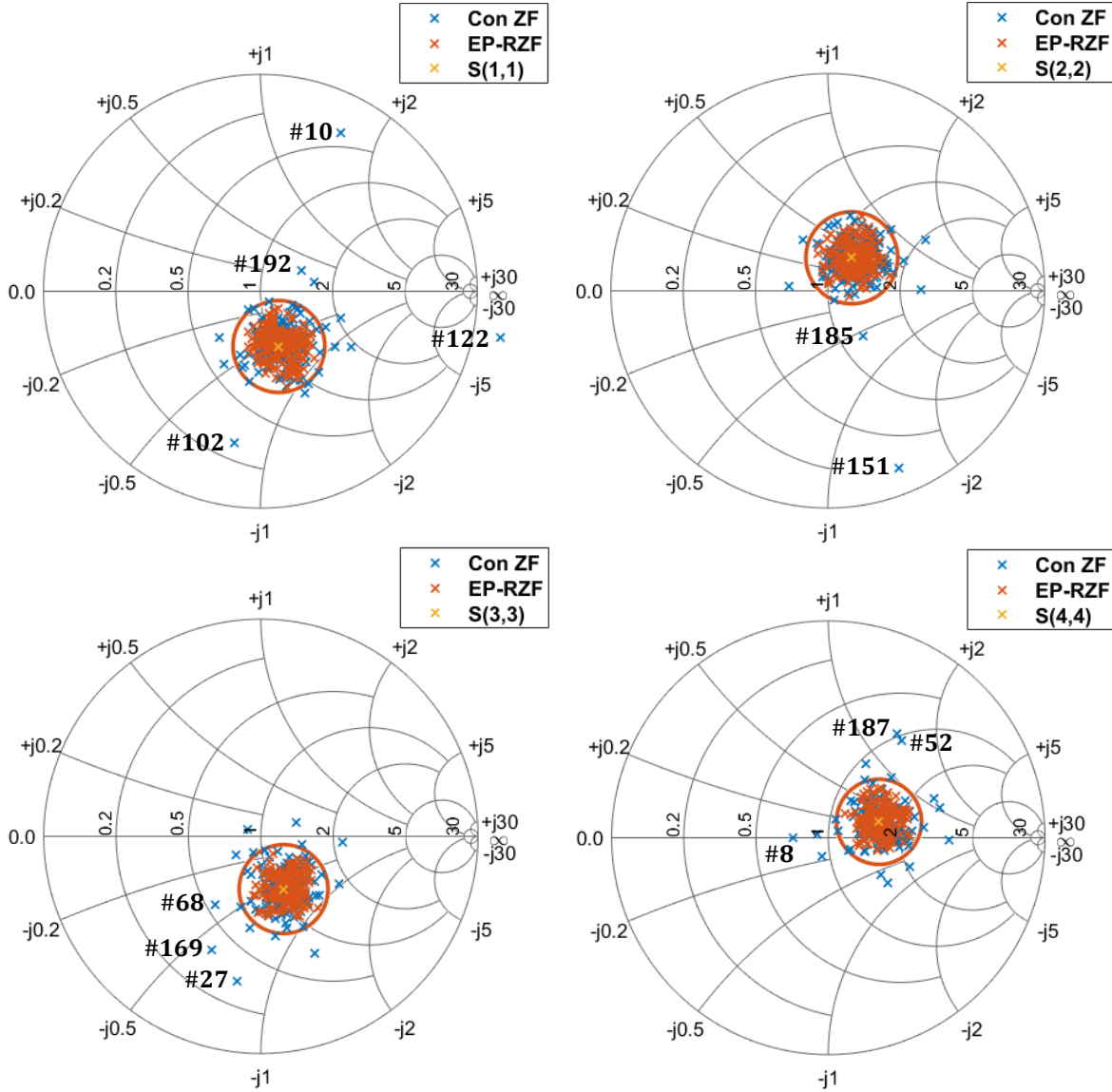
Figure 4.7: The average active impedances at the PA outputs across the 200 channel realizations. The red circles indicate the maximum load deviation under EP precoding.
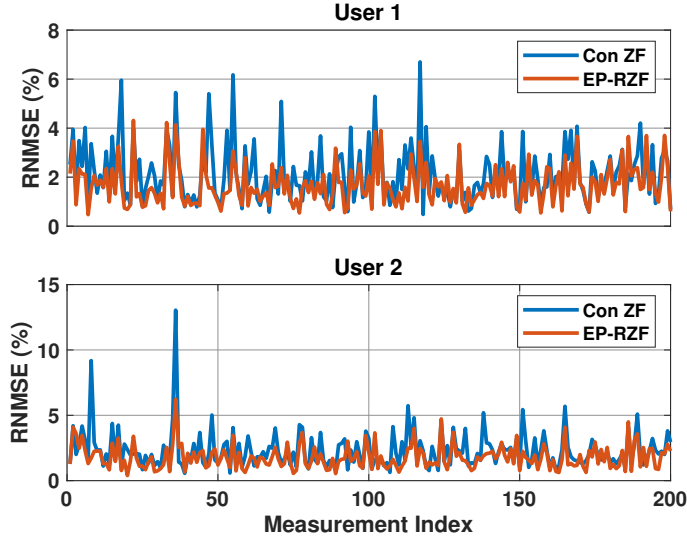
Figure 4.8: The RNMSE values at the two users across the 200 channel realizations.

$\mathbf{J}(.)$ in (4.11) is sparse (around 80% of its elements are zeros when $K/L = 4$) and only an approximate solution is needed, one could roughly estimate the cost of each iteration to be 2.5-3 times the cost of the conventional ZF precoder. Given that around 7 iterations are needed on average (the exact number depends on the channel realization), the EP-RZF precoder is roughly 15-20 times more computationally complex than the conventional ZF one. The same rough estimate applies to the EP-MRT and EP-MMSE precoders as well. On the other hand, the method in Section 3.3.1 requires only one or two iterations, where each iteration involves solving a system of linear equations that is of the same size as the system required for computing the corresponding conventional precoder. The additional cost incurred in (3.13)-(3.15) is all but offset by the fact that multiple columns of $\mathbf{H}_\Omega$ are zeroed in (3.9). Thus, the modified precoders in Section 3.3.1 are only about 2-3 times more computationally complex than the conventional ones.

Nevertheless, the EP precoders proposed in this chapter represent a more robust solution to the problem at hand. With EP precoding, there is no need for multiple DPD coefficient sets nor pre-characterizing the PAs' behavior. Furthermore, as evident from comparing Figs. 4.2 and 3.5, EP precoding yields more reduction in the maximum per-chain power level than that obtained with the method in Section 3.3.1, which enables the use of smaller PAs. Finally, forcing all RF chains to transmit the same average power simplifies the hardware design of the driver-stage amplifiers preceding the PAs and the pre-processing required (since all signals will have the same dynamic range).

4.5 Summary

In this chapter, we proposed three linear precoding schemes that serve as hardware-friendly, albeit more computationally complex, substitutes to the three basic precoders (MRT, ZF, and MMSE). The proposed precoders result in equal average-power levels across all RF chains, independently of the channel conditions. With these precoders employed, the extent of crosstalk-induced load modulation at the PAs' outputs is significantly reduced, and only one DPD coefficient set per PA is needed. In addition, the proposed precoders simplify the control and scaling settings of the DACs and driver-stage amplifiers preceding the PAs. Numerical simulations and experiments showed that the proposed precoders substantially improve the transmitter's resilience to variations in channel conditions.

Chapter 5

Reducing the Computational Complexity of the DPD Subsystem

The energy efficiency of the DPD subsystem can be improved in two ways. The first is reducing the power consumption of the TOR needed to train the DPD modules. This can be achieved by operating the TOR ADC below the Nyquist rate, which yields no loss in performance as recent works have shown. The second approach to improving energy efficiency is to reduce the power consumption of the real-time DPD engine. This entails employing low-computationally-complex DPD models and minimizing the hardware resources utilized in the DSP logic circuits.

In this chapter, we address these two approaches and propose new techniques that reduce the computational and power overheads incurred in prior works. Specifically, we devise a computationally efficient algorithm to estimate the delay and phase offsets between the transmitter and the sub-Nyquist TOR. The proposed algorithm improves upon the exhaustive search methods employed in prior works. In addition, we propose a piece-wise-based DPD model that requires less hardware resources to implement and introduces less latency when compared with similar works in the literature.

5.1 Low-Complexity Synchronization in Sub-Nyquist TOR Architectures

Recent works on DPD have explored the use of under-sampling (or sub-Nyquist) ADCs. The rationale behind earlier works [40, 81–84] was to band-limit the feedback signal, so as

to prevent aliasing when sampling it with low-rate ADCs. This approach, however, limits the extent to which out-of-band emissions can be reduced because the band-limiting filter biases the DPD coefficients towards eliminating the distortion within the captured portion of the PA output spectrum, with no direct control over that in the omitted segments. Later works [85, 86] demonstrated that excellent out-of-band performance can be achieved using ADCs with arbitrarily low sampling rates, as long as their analog bandwidth covers the whole PA output spectrum and no band-limiting filters are inserted. Nevertheless, the works in [85, 86] utilized the direct-conversion architecture in Fig. 2.6a, which is prone to I/Q imbalance. This problem was circumvented in [87, 88], where it was shown that only one branch of the I/Q demodulator and one sub-Nyquist ADC are sufficient. The authors of [89, 90] took this concept one step further, and showed that the sub-Nyquist ADC can also be used in a non-zero-IF configuration.

The main problem with the works in [89, 90] is the reliance on exhaustive search methods for estimating the delay and phase offsets between the sub-Nyquist TOR and the transmitter. In what follows, we propose a computationally efficient algorithm for estimating these offsets. The proposed algorithm substantially reduces the DPD training duration by minimizing the time required for synchronization.

5.1.1 Updating the DPD Coefficients

We start by reviewing the DPD training architecture in [89, 90], albeit in a more rigorous fashion. The sub-Nyquist TOR architecture is shown in Fig. 5.1, in which the ADC sampling rate is a sub-multiple of the baseband processing rate, i.e., $F_{ADC} = F_s/D$ where D is a positive integer. Unlike the conventional non-zero-IF architecture in Fig. 2.6b, the sub-Nyquist architecture places no restrictions on f_{IF} or F_{ADC} (i.e., both can be arbitrarily low), and no DDC is performed. Nevertheless, the analog bandwidth of the ADC must still cover the whole spectrum of the feedback signal $f \in [f_{IF} - F_s/2, f_{IF} + F_s/2]$. Note that setting $f_{IF} = 0$ yields the architecture in [87, 88].
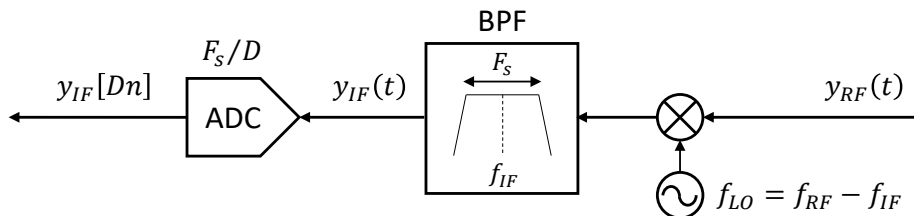

Figure 5.1: The sub-Nyquist TOR architecture.

The DPD update equation in (2.17) can be rewritten in the following form

$$\mathbf{w}^l = \mathbf{w}^{l-1} - \tau \Delta \mathbf{w}, \tag{5.1}$$

where $\Delta \mathbf{w}$ is the LS solution to

$$\mathbf{\Phi} \Delta \mathbf{w} = \left(\frac{\mathbf{y}}{G} e^{-j\hat{\theta}} - \mathbf{x} \right). \tag{5.2}$$

Since DDC is not possible with arbitrarily low f_{IF} and F_{ADC}, the objective is to express the DPD update vector $\Delta \mathbf{w}$ in (5.2) in terms of the passband feedback samples $y_{IF}[n]$, rather than their unobtainable baseband equivalents $y[n]$.

The passband signal $y_{IF}(t)$ and its baseband equivalent $y(t)$ are related by $y_{IF}(t) = \text{Re}\{y(t)e^{j2\pi f_{IF}t}\}$. If the ADC sampling frequency is the same as the baseband processing rate (i.e., $D = 1$) then

$$y_{IF}[n] = \text{Re}\{y(nT_s)e^{j2\pi f_{IF}(nT_s)}\} = \text{Re}\{y[n]e^{j2\pi\Omega n}\}, \tag{5.3}$$

where $T_s = 1/F_s$, and $\Omega = f_{IF}/F_s$. Define the following diagonal matrix

$$\mathbf{T} = e^{j\hat{\theta}} \text{diag}\left(\begin{bmatrix} e^{j2\pi\Omega(M)} & \cdots & e^{j2\pi\Omega(N-1)} \end{bmatrix} \right), \tag{5.4}$$

where M is the memory depth of the DPD model. The LS solution to the system of equations in (5.2) is unaltered if we multiply both sides by $\mathbf{T}$ since $\mathbf{T}$ is a unitary matrix, i.e., $\mathbf{T}^H \mathbf{T} = \mathbf{I}$ [42]. Multiplying both sides of (5.2) by $\mathbf{T}$ then taking the real part gives

$$\text{Re}\{\mathbf{T}\mathbf{\Phi}\} \text{Re}\{\Delta \mathbf{w}\} - \text{Im}\{\mathbf{T}\mathbf{\Phi}\} \text{Im}\{\Delta \mathbf{w}\} = \text{Re}\left\{ \mathbf{T} \left(\frac{\mathbf{y}}{G} e^{-j\hat{\theta}} - \mathbf{x} \right) \right\},$$

or equivalently [89, 90],

$$\mathbf{\Upsilon} \begin{bmatrix} \text{Re}\{\Delta \mathbf{w}\} \\ \text{Im}\{\Delta \mathbf{w}\} \end{bmatrix} = \left(\frac{\mathbf{y}_{IF}}{G} - \mathbf{x}_{IF} \right), \tag{5.5}$$

where $\mathbf{y}_{IF} = \text{Re}\{\mathbf{T}\mathbf{y}e^{-j\hat{\theta}}\} = [y_{IF}[M], \dots, y_{IF}[N-1]]^T$ is the vector of passband feedback samples and

$$\mathbf{\Upsilon} = \begin{bmatrix} \text{Re}\{\mathbf{T}\mathbf{\Phi}\} & -\text{Im}\{\mathbf{T}\mathbf{\Phi}\} \end{bmatrix}$$
$$\mathbf{x}_{IF} = \text{Re}\{\mathbf{T}\mathbf{x}\}.$$

Note that (5.3) was utilized. Equation (5.5) expresses the real and imaginary parts of the update vector $\Delta \mathbf{w}$ in terms of the passband feedback $y_{IF}[n]$ and the baseband input $x[n]$,

71

as desired. As before (see Section 2.2.1), the explicit matrix inversion $\left(\boldsymbol{\Upsilon}^T\boldsymbol{\Upsilon}\right)^{-1}$ need not be evaluated, as the RLS algorithm can be used to compute a regularized solution.

Now, if the ADC operates at a rate of F_s/D, where D is a positive integer, the received passband samples are $y_{IF}[Dn] = y_{IF}(DnT_s)$, which corresponds to sampling only every D^{th} entry of the $\mathbf{y}_{IF}$ vector in (5.5). By keeping the corresponding rows of $\boldsymbol{\Upsilon}, \mathbf{x}_{IF}$ and dropping the rest, the reduced system of equations can be solved for the real and imaginary parts of $\Delta\mathbf{w}$. Since the full-rate input signal $x[n]$ is known, the preserved rows of $\boldsymbol{\Upsilon}$ can be fully computed, and the number of columns is unchanged. Therefore, under-sampling introduces no loss in performance, as long as enough rows are kept. In theory, there is no limit to how large the under-sampling factor D can be but in practice, some hardware constraints (e.g., clock jitter) may impose an upper bound on D.

It is worthwhile emphasizing that this architecture does not violate the Nyquist –Shannon sampling theorem. As the well-known theorem dictates, the full-rate feedback signal $y_{IF}[n]$ cannot be reconstructed from the sub-sampled one due to aliasing. Nevertheless, we are not interested in obtaining the missing samples, but rather in estimating a finite set of parameters that characterize the PA's nonlinear behavior. Equation (5.5) represents a system of linear equations in $2P$ unknowns (where P is the number of DPD coefficients) that are to be estimated from the feedback samples. Solving this system of equations requires at least $2P$ feedback samples, and the quality of the obtained solution (in the sense that it properly linearizes the PA) improves with increasing the number of samples. These samples can be obtained at any rate and even at irregular intervals.

5.1.2 Estimating Delay and Phase Offsets

A critical component of the DPD training routine is the delay and phase alignment algorithm. Below, the optimal ML algorithm for estimating the delay and phase offsets between $z[n]$ and $y_{IF}[n]$ is derived.

ML Derivation

Using (5.3) and (2.9), the passband feedback signal $y_{IF}(t)$ can be expressed in terms of the I and Q components of the baseband predistorted signal $z(t) = z_I(t) + jz_Q(t)$, in the

presence of real-valued AWGN $\eta(t)$, as

$$
\begin{aligned}
y_{IF}(t) &\approx \mathrm{Re}\{h_0\, z(t - t_0)e^{j(2\pi f_{IF}(t-t_0)+\theta)}\} + \eta(t) \\
&= h_0\, z_I(t - t_0)\cos(2\pi f_{IF}(t - t_0) + \theta) \\
&\quad - h_0\, z_Q(t - t_0)\sin(2\pi f_{IF}(t - t_0) + \theta) + \eta(t),
\end{aligned}
\tag{5.6}
$$

where t_0 is the system delay, h_0 is the channel gain, and θ is the combined phase offset due to transmitter circuitry and phase incoherence. Note that h_0 is restricted to being a positive real value as the phase of the system response is absorbed into θ. The equation above represents a good approximation if the PA is weakly nonlinear.

The full-rate case is when the passband signal is sampled at the same rate as the transmitter DACs, i.e., $D = 1$ in Fig. 5.1. If this rate is F_s, the received samples can be expressed as

$$
\begin{aligned}
y_{IF}[n] &= h_0\, z_I[n - n_0]\cos(2\pi\Omega(n - n_0) + \theta) \\
&\quad - h_0\, z_Q[n - n_0]\sin(2\pi\Omega(n - n_0) + \theta) + \eta[n],
\end{aligned}
\tag{5.7}
$$

where $\Omega = f_{IF}/F_s$ and $n_0 = t_0 F_s = t_0/T_s$. Note that $y_{IF}[n] = y_{IF}(nT_s)$ and the same applies for $z_I[n], z_Q[n]$, and $\eta[n]$.

Let N be the number of signal-containing samples of $z_k[n] = z_I[n] + jz_Q[n]$ and $M > N$ be the total number of received samples of $y_{IF}[n]$ where the extra $M - N$ samples contain no signal component, i.e., only AWGN. Assume, for now, that n_0 is an integer and define the following two signals

$$
\begin{aligned}
r[n] &= z_I[n]\cos(2\pi\Omega n) - z_Q[n]\sin(2\pi\Omega n) \\
s[n] &= -z_I[n]\sin(2\pi\Omega n) - z_Q[n]\cos(2\pi\Omega n).
\end{aligned}
\tag{5.8}
$$

It follows that (5.7) can be expressed as

$$
y_{IF}[n] = \eta[n] + \begin{cases} 0, & 0 \le n < n_0 \\ \alpha_1 r[n - n_0] + \alpha_2 s[n - n_0], & n_0 \le n < n_0 + N \ , \\ 0, & n_0 + N \le n < M \end{cases}
\tag{5.9}
$$

where $\alpha_1 = h_0 \cos\theta$ and $\alpha_2 = h_0 \sin\theta$. Since $\eta[n]$ is AWGN, the likelihood function is [91]

$$p(\mathbf{y}_{IF}; \alpha_1, \alpha_2, n_0) = \frac{1}{\left(\sqrt{2\pi\sigma^2}\right)^M} \prod_{n=0}^{n_0-1} \exp\left(\frac{-y_{IF}^2[n]}{2\sigma^2}\right)$$

$$\cdot \prod_{n=n_0}^{n_0+N-1} \exp\left(\frac{-1}{2\sigma^2}\big(y_{IF}[n] - \alpha_1 r[n-n_0] - \alpha_2 s[n-n_0]\big)^2\right)$$

$$\cdot \prod_{n=n_0+N}^{M-1} \exp\left(\frac{-y_{IF}^2[n]}{2\sigma^2}\right), \tag{5.10}$$

where σ^2 is the noise power. The negative of the logarithm of the likelihood function, after omitting constant factors, can be expressed as

$$C(\alpha_1, \alpha_2, n_0) = \sum_{n=0}^{n_0-1} y_{IF}^2[n] + \sum_{n=n_0+N}^{M-1} y_{IF}^2[n]$$

$$+ \sum_{n=n_0}^{n_0+N-1} \big(y_{IF}[n] - \alpha_1 r[n-n_0] - \alpha_2 s[n-n_0]\big)^2 \tag{5.11}$$

Changing the summation index of the last term gives

$$C(\alpha_1, \alpha_2, n_0) = \sum_{n=0}^{n_0-1} y_{IF}^2[n] + \sum_{n=n_0+N}^{M-1} y_{IF}^2[n] + \sum_{n=0}^{N-1} \big(y_{IF}[n+n_0] - \alpha_1 r[n] - \alpha_2 s[n]\big)^2$$

$$= \sum_{n=0}^{n_0-1} y_{IF}^2[n] + \sum_{n=n_0+N}^{M-1} y_{IF}^2[n] + \big(\mathbf{y}_{IF}(n_0) - \mathbf{H}\boldsymbol{\alpha}\big)^T \big(\mathbf{y}_{IF}(n_0) - \mathbf{H}\boldsymbol{\alpha}\big), \tag{5.12}$$

where $\mathbf{y}_{IF}(n_0) = [y_{IF}[n_0], \ldots, y_{IF}[n_0 + N - 1]]^T$, $\mathbf{H} = [\mathbf{r}\quad \mathbf{s}]$, $\mathbf{r} = [r[0], \ldots, r[N-1]]^T$, $\mathbf{s} = [s[0], \ldots, s[N-1]]^T$, and $\boldsymbol{\alpha} = [\alpha_1, \alpha_2]^T$. The ML estimates of the three parameters $(\alpha_1, \alpha_2, n_0)$ are obtained by maximizing the likelihood function in (5.10), or equivalently, minimizing $C(\alpha_1, \alpha_2, n_0)$. For any n_0, the $C(\alpha_1, \alpha_2, n_0)$ is quadratic in $\boldsymbol{\alpha}$ and is minimized by [91]

$$\hat{\boldsymbol{\alpha}} = \big(\mathbf{H}^T\mathbf{H}\big)^{-1}\mathbf{H}^T\mathbf{y}_{IF}(n_0). \tag{5.13}$$

Substituting this back in (5.12) yields

$$C(\hat{\alpha}_1, \hat{\alpha}_2, n_0) = \sum_{n=0}^{n_0-1} y_{IF}^2[n] + \sum_{n=n_0+N}^{M-1} y_{IF}^2[n]$$
$$+ \left(\left[\mathbf{I} - \mathbf{H}(\mathbf{H}^T\mathbf{H})^{-1}\mathbf{H}^T\right]\mathbf{y}_{IF}(n_0)\right)^T \cdot \left(\left[\mathbf{I} - \mathbf{H}(\mathbf{H}^T\mathbf{H})^{-1}\mathbf{H}^T\right]\mathbf{y}_{IF}(n_0)\right)$$
$$= \sum_{n=0}^{n_0-1} y_{IF}^2[n] + \sum_{n=n_0+N}^{M-1} y_{IF}^2[n] + \mathbf{y}_{IF}^T(n_0)\left(\mathbf{I} - \mathbf{H}(\mathbf{H}^T\mathbf{H})^{-1}\mathbf{H}^T\right)\mathbf{y}_{IF}(n_0)$$
$$= \sum_{n=0}^{M-1} y_{IF}^2[n] - \mathbf{y}_{IF}^T(n_0)\mathbf{H}(\mathbf{H}^T\mathbf{H})^{-1}\mathbf{H}^T\mathbf{y}_{IF}(n_0), \tag{5.14}$$

where the fact that $\mathbf{y}_{IF}^T(n_0)\mathbf{y}_{IF}(n_0) = \sum_{n=0}^{N-1} y_{IF}^2[n+n_0] = \sum_{n=n_0}^{n_0+N-1} y_{IF}^2[n]$ was used. Since the first term is not a function of n_0, the ML estimate of n_0 is simply obtained by maximizing

$$\mathbf{y}_{IF}^T(n_0)\mathbf{H}(\mathbf{H}^T\mathbf{H})^{-1}\mathbf{H}^T\mathbf{y}_{IF}(n_0). \tag{5.15}$$

Now, if the passband signal is sampled at a rate of F_s/D, where $D \in \mathbb{Z}_+, D > 1$, the received samples are $y_D[m] = y_{IF}[Dm]$, $m = 0, \ldots, M_D - 1$. Assuming $DM_D > N$ (i.e., enough samples are collected), the negative of the logarithm of the likelihood function now becomes

$$C(\alpha_1, \alpha_2, n_0) = \sum_{m=0}^{\lceil \frac{n_0}{D} \rceil - 1} y_D^2[m] + \sum_{m=\lfloor \frac{n_0+N-1}{D} \rfloor + 1}^{M_D-1} y_D^2[m]$$
$$+ \sum_{m=\lceil \frac{n_0}{D} \rceil}^{\lfloor \frac{n_0+N-1}{D} \rfloor} \left(y_D[m] - \alpha_1 r[Dm - n_0] - \alpha_2 s[Dm - n_0]\right)^2 \tag{5.16}$$

Unlike the case where $D = 1$, the indices of the involved samples of $r[Dm - n_0]$ and $s[Dm - n_0]$ in the last term now depend upon the remainder of the division of n_0 by D, which we denote by l, i.e., $l = n_0 \bmod D$. Assuming that N is divisible by D, then if $l = 0$, the involved indices are $n = Dm$, $m = 0, \ldots, N/D - 1$, while if $l \neq 0$, they become $n = Dm + (D - l)$, $m = 0, \ldots, N/D - 1$. A concise way of writing this is $n = Dm + p(n_0)$, where $p(n_0) = (-n_0) \bmod D$.

Therefore, the $\mathbf{H}$ matrix is split into D matrices of N/D rows each: $\mathbf{H}_0, \ldots, \mathbf{H}_{D-1}$, where $\mathbf{H}_p$ is the matrix formed by selecting the rows with indices $Dm+p$, $m = 0, \ldots, N/D-$

1. The ML estimate of n_0 is then obtained by maximizing

$$\mathbf{y}_D^T(n_0)\mathbf{H}_{p(n_0)}\big(\mathbf{H}_{p(n_0)}^T\mathbf{H}_{p(n_0)}\big)^{-1}\mathbf{H}_{p(n_0)}^T\mathbf{y}_D(n_0), \tag{5.17}$$

where $\mathbf{y}_D(n_0) = [y_D[\lceil \frac{n_0}{D}\rceil], \ldots, y_D[\lfloor \frac{n_0+N-1}{D}\rfloor]]^T$, and $p(n_0)$ is as above.

Algorithm Steps for $D = 1$

Let $g_{IF}[n], n = 0, \ldots, M-1$ be the M passband samples captured at a rate of F_s. Without loss of generality, we assume that $M > N$, where N is the number of transmitted samples. First, compute $\mathbf{H} = [\mathbf{r} \quad \mathbf{s}]$, where $\mathbf{r} = [r[0], \ldots, r[N-1]]^T$, $\mathbf{s} = [s[0], \ldots, s[N-1]]^T$, and

$$r[n] = \text{Re}\{z[n]\,e^{j2\pi\Omega n}\}$$
$$s[n] = -\text{Im}\{z[n]\,e^{j2\pi\Omega n}\}. \tag{5.18}$$

From which, compute the 2×2 weighting matrix $\mathbf{W} = (\mathbf{H}^T\mathbf{H})^{-1}$. Next, for all integers $d = 0, \ldots, M-N$, compute

$$\mathbf{v}(d) = \mathbf{H}^T\mathbf{g}_{IF}(d) = \begin{bmatrix} \sum_{n=0}^{N-1} r[n]\,g_{IF}[n+d] \\ \sum_{n=0}^{N-1} s[n]\,g_{IF}[n+d] \end{bmatrix}, \tag{5.19}$$

where $\mathbf{g}_{IF}(d) = [g_{IF}[d], \ldots, g_{IF}[d+N-1]]^T$. The integer part of the delay is then estimated as

$$\hat{d}_0 = \underset{d\in[0,M-N]}{\text{argmax}}\ \mathbf{v}^T(d)\,\mathbf{W}\,\mathbf{v}(d). \tag{5.20}$$

Simply put, the integer part of the delay is found through cross-correlating the feedback signal with two transformed variants of $z[n]$, then weighting the result by the pre-computed matrix $\mathbf{W}$. The remaining fractional delay $\zeta \in (-0.5, 0.5)$ can be estimated by interpolating the integral-argument likelihood function $L(d) = \mathbf{v}^T(d)\,\mathbf{W}\,\mathbf{v}(d)$ around $\hat{d}_0$ and finding the maximum. It can then be compensated for using fractional delay filters [92]. Note that the fractional part of the delay should not be applied to $g_{IF}[n]$ as the signal is aliased. In all further computations, it is to be applied to the full-rate signal involved ($x[n], z[n]$, or the columns of $\mathbf{H}$). Finally, the nominal amplifier gain h_0 and phase offset θ are estimated from $\mathbf{g}_{IF}(\hat{d}_0)$ and the fractionally-delayed $\mathbf{H}$ as

$$\begin{bmatrix} \hat{\alpha}_1 \\ \hat{\alpha}_2 \end{bmatrix} = \mathbf{W}\mathbf{H}^T\mathbf{g}_{IF}(\hat{d}_0)$$

$$\hat{h}_0\,e^{j\hat{\theta}} = \hat{\alpha}_1 + j\hat{\alpha}_2. \tag{5.21}$$

If the TOR has a high SNR, it suffices to perform the operations above using $B < N$ samples.

Algorithm Steps for $D > 1$

Let $g_D[n] = g_{IF}[Dn], n = 0, \ldots, M_D - 1$ be the M_D passband samples captured at a rate of F_s/D, where $D \in \mathbb{Z}_+$. The captured signal is first up-sampled by inserting $D-1$ zeros after every sample to form the signal $q_{IF}[n], n = 0, \ldots, DM_D - 1$. Note that no interpolation is employed. Without loss of generality, we assume that $DM_D > N$ and that N is divisible by D. As before, the signals $r[n], s[n]$, and the $\mathbf{H}$ matrix are to be computed first.

The main difference from the case where $D = 1$ is that D weighting matrices are computed, instead of one. The N-rows $\mathbf{H}$ matrix is split into D matrices: $\mathbf{H}_0, \ldots, \mathbf{H}_{D-1}$ of N/D rows each, where $\mathbf{H}_p$ is the matrix formed by selecting the rows with indices $Dm + p, m = 0, \ldots, N/D - 1$. The pth weighting matrix is then $\mathbf{W}_p = (\mathbf{H}_p^T \mathbf{H}_p)^{-1}, p = 0, \ldots, D - 1$. For all integers $d = 0, \ldots, DM_D - N$, compute

$$\mathbf{v}(d) = \mathbf{H}^T \mathbf{q}_{IF}(d) = \begin{bmatrix} \sum_{n=0}^{N-1} r[n]\, q_{IF}[n + d] \\ \sum_{n=0}^{N-1} s[n]\, q_{IF}[n + d] \end{bmatrix}$$

$$p(d) = (-d) \bmod D, \tag{5.22}$$

where $\mathbf{q}_{IF}(d) = [q_{IF}[d], \ldots, q_{IF}[d + N - 1]]^T$. The integer part of the delay is then estimated as

$$\hat{d}_0 = \underset{d \in [0, M-N]}{\operatorname{argmax}} \; \mathbf{v}^T(d)\, \mathbf{W}_{p(d)}\, \mathbf{v}(d). \tag{5.23}$$

As before, the remaining fractional delay can be estimated by interpolating the likelihood function and finding the maximum. The nominal amplifier gain and phase offset are then estimated as

$$p_0 = (-\hat{d}_0) \bmod D$$

$$\begin{bmatrix} \hat{\alpha}_1 \\ \hat{\alpha}_2 \end{bmatrix} = \mathbf{W}_{p_0} \mathbf{H}_{p_0}^T \mathbf{q}_D(\hat{d}_0)$$

$$\hat{h}_0\, e^{j\hat{\theta}} = \hat{\alpha}_1 + j\hat{\alpha}_2, \tag{5.24}$$

where $\mathbf{q}_D(\hat{d}_0)$ denotes the vector obtained from $\mathbf{q}_{IF}(\hat{d}_0)$ by omitting the zeros that were inserted in the beginning. The indices of the zeros that were removed from $\mathbf{q}_{IF}(\hat{d}_0)$ indicate the indices of the rows that are to be removed from the matrix equation in (5.5).

Finally, we compare the proposed alignment algorithm to those in prior works [87–90]. If i) all weighting matrices are identical (i.e., $\mathbf{W}_p = \mathbf{W}_0 \; \forall p \in \{1, \ldots, D-1\}$), ii) the I and Q components of $z[n]$ are uncorrelated, and iii) $f_{IF} = 0$, then the proposed algorithm reduces

77

to that in [88]. Since the first two conditions are not necessarily satisfied in practice, the method in [88] (which is only valid for $f_{IF} = 0$) will not always yield accurate estimates. Furthermore, the proposed algorithm is much more efficient than the two-dimensional search methods in [87,89,90] as it requires only a one-dimensional search (cross-correlation) to estimate the delay offset. The phase offset is directly estimated afterwards, using (5.24), with no additional search.

5.1.3   Experimental Validation

The 4-chain measurement setup in Section 3.5 was used to validate the sub-Nyquist training architecture. The DPD modules were trained using four independently-generated 100-MHz OFDM signals with 8-dB PAPR. The up-sampling factor was set to 5, thereby making $F_s = 500$ MHz. Since the analog bandwidth of the used oscilloscope covers the spectrum of the RF signal around 3.5 GHz, no external down-conversion was employed, i.e., $f_{IF} = f_{RF} = 3.5$ GHz. The dual-input DPD parameters in (3.17)-(3.19) were set to $P = 5$, $M = 1$ and $Q = 3$, and the SISO parameters were set to $N = 8$ and $M_S = 5$.

In sub-Nyquist mode, it is not possible to evaluate the conventional RNMSE and ACPR metrics since the full-rate baseband output samples $y[n]$ cannot be obtained from the undersampled passband ones $y_{IF}[Dn]$. Nevertheless, an alternative form of the RNMSE metric in (2.18) can be computed by comparing the time-aligned vector of received passband samples $\mathbf{q}_D(\hat{d}_0)$ with $\mathbf{x}_D$, which is an up-converted, down-sampled, and amplitude-adjusted version of the baseband input vector $\mathbf{x}$. This vector is obtained as

$$\mathbf{x}_D = \mathbf{B}_{p_0}(\mathbf{B}_{p_0}^T\mathbf{B}_{p_0})^{-1}\mathbf{B}_{p_0}^T\mathbf{q}_D(\hat{d}_0), \tag{5.25}$$

where $\mathbf{B}_{p_0}$ is computed the same way $\mathbf{H}_{p_0}$ is in (5.24), but with $z[n]$ replaced by $x[n]$.

Since the oscilloscope used here can be operated at speeds higher than the Nyquist rate of the captured signals, we opted to utilize the conventional RNMSE and ACPR metrics to characterize the DPD performance. The DPD modules were first trained with the oscilloscope operating in sub-Nyquist mode and the alternative RNMSE metric in (5.25) was used to monitor the performance. After convergence had been observed, the output signals were then captured at the Nyquist rate to calculate the conventional performance metrics. Table 5.1 shows the results obtained with four different sub-sampling factors $D = 1, 2, 5$, and 10, which correspond to setting F_{ADC} to $500, 250, 100$ and 50 MSPS respectively. The results in Table 5.1 are very similar across all settings, which confirms the efficacy of the sub-Nyquist training architecture and the accuracy of the proposed algorithm. The small variations are likely attributable to measurement noise.

Table 5.1: RNMSE (%) and lower/upper ACPR (dB) at the outputs of the four PAs with different sub-sampling factors D.

DPD Type	PA 1	PA 2	PA 3	PA 4
None	8.4%	11.8%	8.9%	12.2%
	-36.2/-32.7	-34.9/-33.6	-37.3/-31.0	-35.0/-34.0
$D = 1$	1.1%	1.0%	1.2%	1.3%
	-51.5/-51.1	-51.1/-51.0	-49.9/-49.9	-51.7/-51.6
$D = 2$	1.1%	0.9%	1.0%	1.0%
	-50.9/-51.0	-50.8/-50.3	-49.9/-49.9	-51.8/-51.7
$D = 5$	1.2%	1.0%	1.0%	1.0%
	-51.1/-51.0	-52.2/-51.7	-50.0/-50.0	-51.9/-51.7
$D = 10$	1.1%	1.0%	1.1%	1.0%
	-50.4/-50.3	-51.1/-50.6	-49.7/-49.8	-51.4/-51.4

5.2 Hardware-Efficient Implementation of the DPD Engine

The power consumption of the DPD engine can be substantially reduced by employing piece-wise models instead of the conventional ones based on global polynomials (e.g., [32, 35–38]). Piece-wise models comprise multiple sub-models that cover non-overlapping regions of the input signal range, where the sub-model used at a given instant depends on the magnitude of the input signal at that instant. The associated savings in hardware resources stem from the fact that the sub-models need only cover a limited range of the overall PA response. Consequently, they can have fewer coefficients and be of lower order than a conventional polynomial model. Among the numerous piece-wise-based DPD models in the literature (e.g., [93–99]), the model in [94] seems to hold the most promise since it enforces continuity between the different sub-regions using a low-complexity technique.

The main drawback of the model in [94] is the need for the square-root function, which is difficult to implement efficiently in practice. In the following, we alleviate this requirement by redefining the piece-wise DPD model in terms of the squared magnitude of the input signal and utilizing sub-regions with unequal lengths. In addition, we propose a parallelization architecture that improves upon the one in [100].

5.2.1 Linear Interpolation and Extrapolation with Unequal Segments

Let $f(x; \boldsymbol{\alpha}, \boldsymbol{\Phi})$ be a complex-valued piece-wise linear (PWL) function of the positive real-valued argument x, where $\boldsymbol{\alpha} = [\alpha_0, \ldots, \alpha_N] \in \mathbb{R}_+^{N+1}$ and $\boldsymbol{\Phi} = [\phi_0, \ldots, \phi_N] \in \mathbb{C}^{N+1}$. The region over which the function is defined is split into N segments of unequal lengths according to the thresholds vector $\boldsymbol{\alpha}$, where $\alpha_0 = 0$. The function values at the thresholds are given by the vector $\boldsymbol{\Phi}$, i.e., $f(\alpha_k; \boldsymbol{\alpha}, \boldsymbol{\Phi}) = \phi_k$. In each interval $[\alpha_k, \alpha_{k+1}]$, the function is defined as a straight line between points (α_k, ϕ_k) and $(\alpha_{k+1}, \phi_{k+1})$, that is,

$$f(x; \boldsymbol{\alpha}, \boldsymbol{\Phi}) = \phi_k + \left(\frac{\phi_{k+1} - \phi_k}{\alpha_{k+1} - \alpha_k} \right)(x - \alpha_k), \qquad \alpha_k \leq x \leq \alpha_{k+1} \tag{5.26}$$

This can be rewritten to highlight the contribution of ϕ_k and ϕ_{k+1} to the PWL as

$$f(x; \boldsymbol{\alpha}, \boldsymbol{\Phi}) = \left(1 - \frac{x - \alpha_k}{\alpha_{k+1} - \alpha_k} \right)\phi_k + \left(1 + \frac{x - \alpha_{k+1}}{\alpha_{k+1} - \alpha_k} \right)\phi_{k+1}, \qquad \alpha_k \leq x \leq \alpha_{k+1}. \tag{5.27}$$

Similarly, in the interval $[\alpha_{k-1}, \alpha_k]$, the function is defined as a straight line between points $(\alpha_{k-1}, \phi_{k-1})$ and (α_k, ϕ_k), i.e.,

$$f(x; \boldsymbol{\alpha}, \boldsymbol{\Phi}) = \left(1 - \frac{x - \alpha_{k-1}}{\alpha_k - \alpha_{k-1}} \right)\phi_{k-1} + \left(1 + \frac{x - \alpha_k}{\alpha_k - \alpha_{k-1}} \right)\phi_k, \qquad \alpha_{k-1} \leq x \leq \alpha_k. \tag{5.28}$$

Since these are the only two regions where point (α_k, ϕ_k) contributes to $f(x; \boldsymbol{\alpha}, \boldsymbol{\Phi})$, its contribution over the entire region $[0, \alpha_N]$ is $\phi_k \Lambda_k(x)$, where

$$\Lambda_0(x) = \begin{cases} 1 - \dfrac{x}{\alpha_1}, & 0 \leq x \leq \alpha_1 \\ 0, & \text{otherwise.} \end{cases}$$

$$\Lambda_k(x) = \begin{cases} 1 + \dfrac{x - \alpha_k}{\alpha_k - \alpha_{k-1}}, & \alpha_{k-1} \leq x \leq \alpha_k \\ 1 - \dfrac{x - \alpha_k}{\alpha_{k+1} - \alpha_k}, & \alpha_k \leq x \leq \alpha_{k+1} \\ 0, & \text{otherwise.} \end{cases}$$

$$\Lambda_N(x) = \begin{cases} 1 + \dfrac{x - \alpha_N}{\alpha_N - \alpha_{N-1}}, & \alpha_{N-1} \leq x \leq \alpha_N \\ 0, & \text{otherwise.} \end{cases} \tag{5.29}$$

Note that, since α_{-1} and α_{N+1} are undefined, the upper segment is omitted for $\Lambda_0(x)$ and the lower one is omitted for $\Lambda_N(x)$. The overall PWL can then be expressed as a linear combination of the $N+1$ basis functions as

$$f(x; \boldsymbol{\alpha}, \boldsymbol{\Phi}) = \sum_{k=0}^{N} \phi_k \Lambda_k(x). \tag{5.30}$$

The PWL in (5.30) is non-zero only over the region $0 \leq x \leq \alpha_N$, which is adequate if the input argument x does not exceed the maximum threshold α_N. Nevertheless, in the event that $x \geq \alpha_N$, the last PWL segment defined over $[\alpha_{N-1}, \alpha_N]$ must be extrapolated. In other words,

$$f(x; \boldsymbol{\alpha}, \boldsymbol{\Phi}) = \left(1 - \frac{x - \alpha_{N-1}}{\alpha_N - \alpha_{N-1}}\right)\phi_{N-1} + \left(1 + \frac{x - \alpha_N}{\alpha_N - \alpha_{N-1}}\right)\phi_N, \qquad x \geq \alpha_{N-1}. \tag{5.31}$$

As seen from (5.31), both points $(\alpha_{N-1}, \phi_{N-1})$ and (α_N, ϕ_N) contribute to the extrapolated region. Thus, the basis functions associated with these two points must be redefined as

$$\Lambda_{N-1}(x) = \begin{cases} 1 + \dfrac{x - \alpha_{N-1}}{\alpha_{N-1} - \alpha_{N-2}}, & \alpha_{N-2} \leq x \leq \alpha_{N-1} \\ 1 - \dfrac{x - \alpha_{N-1}}{\alpha_N - \alpha_{N-1}}, & x \geq \alpha_{N-1} \\ 0, & \text{otherwise.} \end{cases}$$

$$\Lambda_N(x) = \begin{cases} 1 + \dfrac{x - \alpha_N}{\alpha_N - \alpha_{N-1}}, & x \geq \alpha_{N-1} \\ 0, & \text{otherwise.} \end{cases} \tag{5.32}$$

All other basis functions $\Lambda_0(x), \ldots, \Lambda_{N-2}(x)$ are those given by (5.29). The PWL function defined here is a generalization of the one with equal segments in [94].

5.2.2 PWL-Based DPD Model

The DISO DPD model used in this section is derived from the one in (3.17)-(3.19) by replacing the polynomials with PWL functions and setting the memory-pruning function to $M(p) = M_S$. Following the notation in Fig. 3.1, the DPD model in each chain is given

by

$$z[n] = \sum_{m=0}^{M_S} s[n-m] \, f\big(\big|s[n-m]\big|^2; \, \boldsymbol{\alpha}, \boldsymbol{\beta^m}\big)$$

$$+ \sum_{m=1}^{M_S} s[n-m] \, f\big(\big|s[n]\big|^2; \, \boldsymbol{\alpha}, \boldsymbol{\gamma^m}\big)$$

$$+ s^2[n] \sum_{m=1}^{M_S} s^*[n-m] \, f\big(\big|s[n]\big|^2; \, \boldsymbol{\alpha}, \boldsymbol{\zeta^m}\big)$$

$$+ s^*[n] \sum_{m=1}^{M_S} s^2[n-m] \, f\big(\big|s[n]\big|^2; \, \boldsymbol{\alpha}, \boldsymbol{\eta^m}\big)$$

$$+ \sum_{m=0}^{M} \hat{a}_2[n-m] \, f\big(\big|s[n-m]\big|^2; \, \boldsymbol{\alpha}, \boldsymbol{\tau^m}\big)$$

$$+ \sum_{m=0}^{M} \hat{a}_2^*[n-m] \, s^2[n-m] \, f\big(\big|s[n-m]\big|^2; \, \boldsymbol{\alpha}, \boldsymbol{\vartheta^m}\big), \tag{5.33}$$

where $\boldsymbol{\beta^m}, \boldsymbol{\gamma^m}, \boldsymbol{\zeta^m}, \boldsymbol{\eta^m}, \boldsymbol{\tau^m}, \boldsymbol{\vartheta^m}$ are the model coefficients, M_S and M are the SISO and DISO memory depths respectively, and the CTMM signal $\hat{a}_2[n]$ is computed using (3.19). Note that the subscript indicating the chain index was removed to improve clarity, i.e., $z[n] \triangleq z_k[n], s[n] \triangleq s_k[n]$, and $\hat{a}_2[n] \triangleq \hat{a}_{2k}[n]$.

During training, each PWL function in (5.33) is replaced by its equivalent form in (5.30). If the PWL thresholds $\alpha_1, \ldots, \alpha_N$ are pre-selected in advance, the model becomes linear in the coefficients $\{\beta_k^m, \gamma_k^m, \zeta_k^m, \eta_k^m, \tau_k^m, \vartheta_k^m\}$ and training can be carried out using conventional methods. Otherwise, both the model coefficients and PWL thresholds can be jointly optimized using a similar procedure to those in [98, 101]. Once the coefficients are determined, a PWL function such as $f(x; \boldsymbol{\alpha}, \boldsymbol{\Phi})$ is implemented by first determining the interval $[\alpha_k, \alpha_{k+1})$ in which its argument x lies using comparators. Then ,the result is used to look-up the appropriate slope A_k and offset B_k of the linear function $A_k x + B_k$ that describes $f(x; \boldsymbol{\alpha}, \boldsymbol{\Phi})$ in that interval. From (5.26), the coefficients A_k, B_k in the kth interval can be expressed as

$$A_k = \frac{\phi_{k+1} - \phi_k}{\alpha_{k+1} - \alpha_k}, \qquad B_k = \phi_k - \alpha_k A_k. \tag{5.34}$$

In this work, we pre-select the thresholds as $\alpha_k = k^2 \Gamma / N^2$ for $k = 0, \ldots, N$, where $\Gamma = \max(|s[n]|^2)$. Since the PWLs are functions of $|s[n]|^2$, rather than $|s[n]|$, this choice

82

of thresholds corresponds to dividing the amplitude-modulation to amplitude-modulation (AM/AM) curve of the PA into equal segments as in [94] (see Fig. 5.2a). If the thresholds were chosen as $\alpha_k = k\Gamma/N$ to give equal-length PWL segments, the AM/AM curve would be split unequally as in Fig. 5.2b. The latter choice would result in intervals with very few input samples, which might result in numerical instability during training. This equal-segment splitting is a compromise between having enough PWL segments in the most nonlinear region of the AM/AM curve, and having enough samples in each of them.
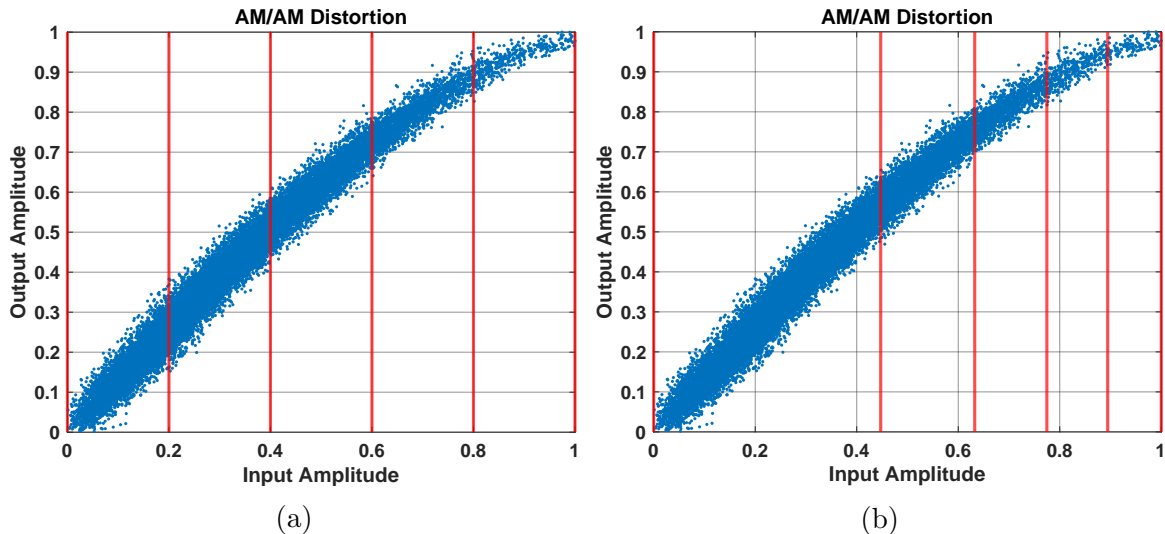
Figure 5.2: Selecting the PWL thresholds as: (a) $\alpha_k = k^2/N^2$; (b) $\alpha_k = k/N$.

5.2.3 Parallelizing the DPD Engine

Modern RF-DACs run at speeds of several GSPS. These speeds far exceed the maximum clock rate possible in commercially available DSP hardware, such as field-programmable gate array (FPGA)s. This mismatch in data rates is handled by parallelizing the functions implemented in the FPGA logic cores into multiple streams that can then be combined by the DAC, as shown in Fig. 5.3. Below, a simple approach to parallelizing the DPD engine is propsoed. For illustration purposes, the approach is demonstrated on a simplified SISO DPD function given by

$$z[n] = \alpha s^3[n] + \beta s^3[n-1],$$

where $s[n]$ is assumed real-valued. Extending the following approach to the DISO DPD model in (5.33) is straightforward.
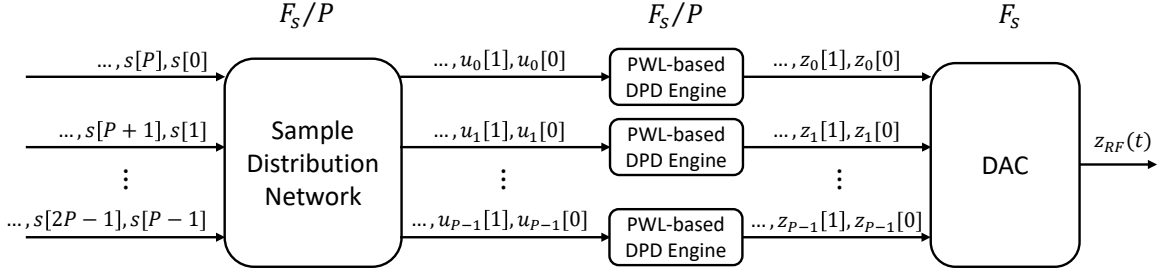
Figure 5.3: Block diagram of a parallelized DPD engine.

The input signal to the DPD system $s[n]$ is split into P lanes $s_0[n], \ldots, s_{P-1}[n]$, where the signal in the pth lane is $s_p[n] = s[p + Pn], n = 0, 1, \ldots$. The objective is to redistribute the input samples so that it is possible to implement P parallel DPD engines that compute the P lanes of the predistorted signal $z_0[n], \ldots, z_{P-1}[n]$, where each DPD engine operates at $1/P$ of the total rate. The proposed parallelization architecture is demonstrated in Fig. 5.4 with $P = 3$. The sample distribution network is comprised of a set of serial-in parallel-out shift registers. The number of buffer stages is $D = \lceil M/P \rceil + d_{\text{pipe}}$, where M is the memory depth and d_{pipe} is the number of pipelining stages needed to compute the nonlinear function that is multiplied with $u[n]$. In this simplified example, $M = 1$, $P = 3$, and the nonlinear function is $u^2[n]$, which can be computed in one clock cycle; hence, $D = \lceil 1/3 \rceil + 1 = 2$. For the PWL functions in (5.33) and complex-valued input, a fully pipelined implementation requires $d_{\text{pipe}} = 5$ clock cycles.

The samples of the P input signals $s_0[n], \ldots, s_{P-1}[n]$ are redistributed to form the signals $u_0[n], \ldots, u_{P-1}[n]$ using the formula

$$u_p[n - m] = s_r[n + c - D], \tag{5.35}$$

where

$$r = (M + p - m) \bmod P$$
$$c = \lfloor (M + p - m)/P \rfloor.$$

As shown in Fig. 5.4, this rearrangement makes it possible to employ a DPD module in each branch since all M samples $u_p[n - 1], \ldots, u_p[n - M]$ are now available at the pth branch. Note that that all multiplication and addition operations in Fig. 5.4 should be pipelined for maximum throughput, but post-distribution pipelining was omitted from the figure to improve clarity.

Since the sample distribution network is placed at the input stage, the signals $u_p[n]$ and $u_p^2[n]$ are available to compute all sorts of cross-products (e.g., $\sum_m u_p[n-m]u_p^2[n-m]$,
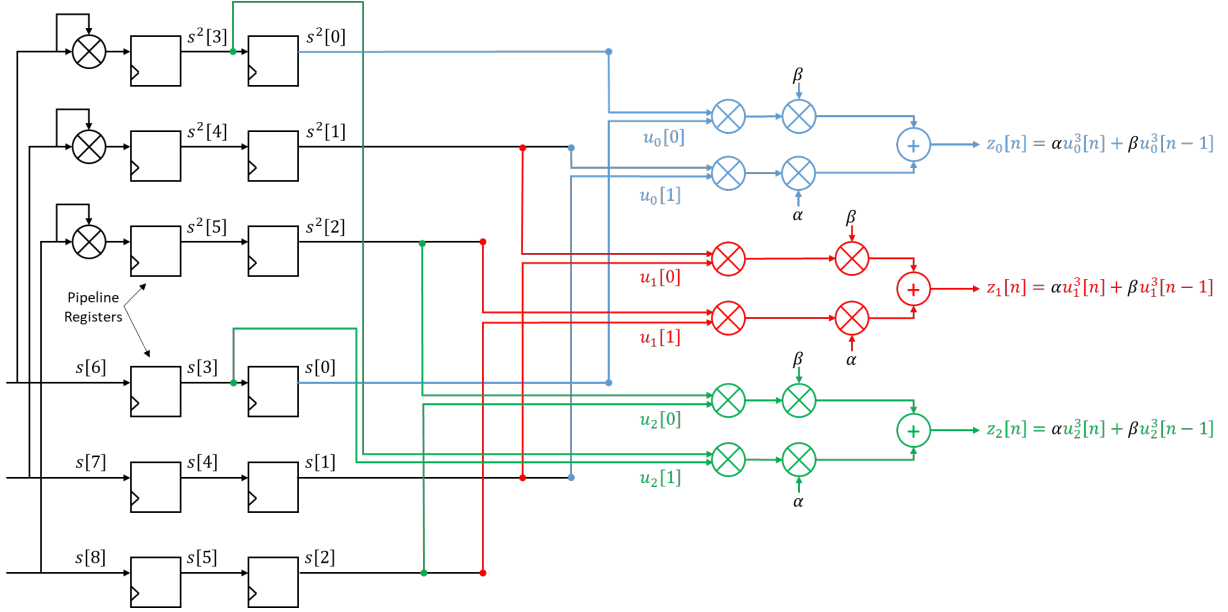
Figure 5.4: Illustrating the parallelization architecture using a simple DPD model: $z[n] = \alpha s^3[n] + \beta s^3[n-1]$ with $P = 3$. Each color corresponds to a different path.

$\sum_m u_p[n-m]u_p^2[n],\dots$) with no additional wiring. This is in contrast to the architecture in [100], in which a different sample distribution network is needed for every type of cross-product term. Although both architectures utilize the same number of multipliers and adders, the proposed one can considerably reduce the number of inter-connections and buffer registers, which relaxes the timing constraints associated with on-chip routing.

5.2.4 Experimental Validation

The first experiment compares the PWL-based DPD model proposed in this section with both the conventional model in (3.18) and the PWL-based one in [94]. The PA used for this experiment was an 8-Watt Doherty GaN design and the test signal was an 8-dB PAPR 100-MHz OFDM signal up-sampled by a factor of 5. The AWG and oscilloscope shown in Fig. 3.9 were used to generate the input signal and capture the PA output signal respectively. Since this experiment involves only one PA, the dual-input terms in (5.33)

were omitted, i.e.,

$$z[n] = \sum_{m=0}^{M_S} s[n-m] \, f\left(\left|s[n-m]\right|^2; \, \boldsymbol{\alpha}, \boldsymbol{\beta^m}\right)$$

$$+ \sum_{m=1}^{M_S} s[n-m] \, f\left(\left|s[n]\right|^2; \, \boldsymbol{\alpha}, \boldsymbol{\gamma^m}\right)$$

$$+ s^2[n] \sum_{m=1}^{M_S} s^*[n-m] \, f\left(\left|s[n]\right|^2; \, \boldsymbol{\alpha}, \boldsymbol{\zeta^m}\right)$$

$$+ s^*[n] \sum_{m=1}^{M_S} s^2[n-m] \, f\left(\left|s[n]\right|^2; \, \boldsymbol{\alpha}, \boldsymbol{\eta^m}\right) \qquad (5.36)$$

The memory depth was set to $M_S = 6$ for both PWL-based and conventional models in (5.36) and (3.18) respectively. The number of segments in (5.36) was set to $N = 5$ while the nonlinearity order in (3.18) was set to $N = 8$. Table 5.2 shows the RNMSE and lower/upper ACPR results obtained with both DPD models, and Fig. 5.5 shows the resulting spectra. The table and figure also show the results when the proposed PWL functions (i.e., unequal segments of $|s[n]|^2$) are replaced by those in [94] (i.e., equal segments of $|s[n]|$).

In Table 5.2, the computational complexity of each of the three DPD models is assessed by counting the number of real-valued floating-point operation (RFLOP)s per input sample. Real-valued addition, multiplication, and comparison, are counted as 1 RFLOP each, while the square-root operation is counted as 6 RFLOPs (as is customary). The results show that PWL-based models deliver better performance than that obtained with conventional polynomial models, while being less complex to implement. This is because utilizing multiple low-order sub-models, instead of a global high-order one, allows for a more accurate representation of amplitude-dependent physical phenomena in PA transistors.

Table 5.2: Comparison between PWL-based and conventional DPD models.

| DPD Model	RFLOPs per sample	RNMSE (%)	ACPR (dB)
None	-	17.3	-28.1/-31.0
Polynomial	455	0.91	-48.5/-48.2
With PWL in [94]	450	0.81	-50.3/-49.5
With proposed PWL	408	0.82	-50.2/-49.5
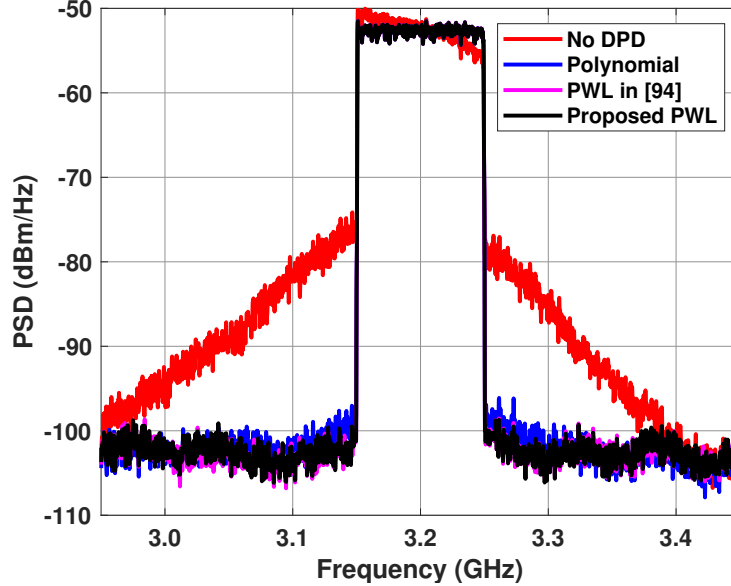
Figure 5.5: Output spectrum of an 8-Watt Doherty PA with both PWL-based and conventional DPD models.

In all experiments presented so far, a computer running MATLAB was used to compute the predistorted signals. For the next experiment, the proposed DPD model was implemented on a commercially available FPGA in order to more accurately assess its run-time complexity. The model in (5.36) with $N = 6$ and $M_S = 4$ was implemented on a Xilinx Ultrascale+ MPSoC ZCU102 evaluation board, where the fourth set of terms (i.e., $s^*[n] \sum_{m=1}^{M_S} s^2[n-m] f(|s[n]|^2; \boldsymbol{\alpha}, \boldsymbol{\eta^m})$) were omitted to reduce the model complexity. The test signal was an 8-dB PAPR 200-MHz OFDM signal over-sampled by a factor of 5, yielding a total bandwidth of 1 GHz. This bandwidth exceeds the MPSoC maximum clock rate, so the DPD model was implemented with a parallelization factor of $P = 4$, i.e., the core clock frequency was 250 MHz. The predistorted signal was up-sampled and up-converted to a center frequency of 2.5 GHz by an AD9162 DAC from Analog Devices. The up-converted signal was fed to a 15-Watt Wolfspeed CGH27015-TB PA and its output was captured with a Keysight DSOS404A oscilloscope, as shown in Fig. 5.6.

The input signal to the DPD engine is represented in fixed-point format to minimize the hardware resources utilized. Hence, with each numerical operation, the bit-width of the signal increases and those extra bits must be truncated before the next numerical operation. Consequently, it is crucial to optimize all numerical operations for the specific

87
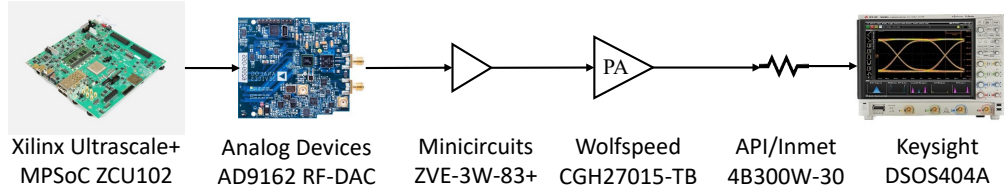
Figure 5.6: Measurement setup for the FPGA-based experiment.

device in use. Fig. 5.7 shows the block diagram of the DSP slice in the MPSoC FPGA. This slice features a pre-adder, a 27×18 asymmetric multiplier and a post-accumulator unit, along with other logic functions. As an example of the device-specific optimizations implemented, the PWL coefficients were represented in 27 bits while the squared signal magnitude $|s[n]|^2$ was truncated to 18 bits.
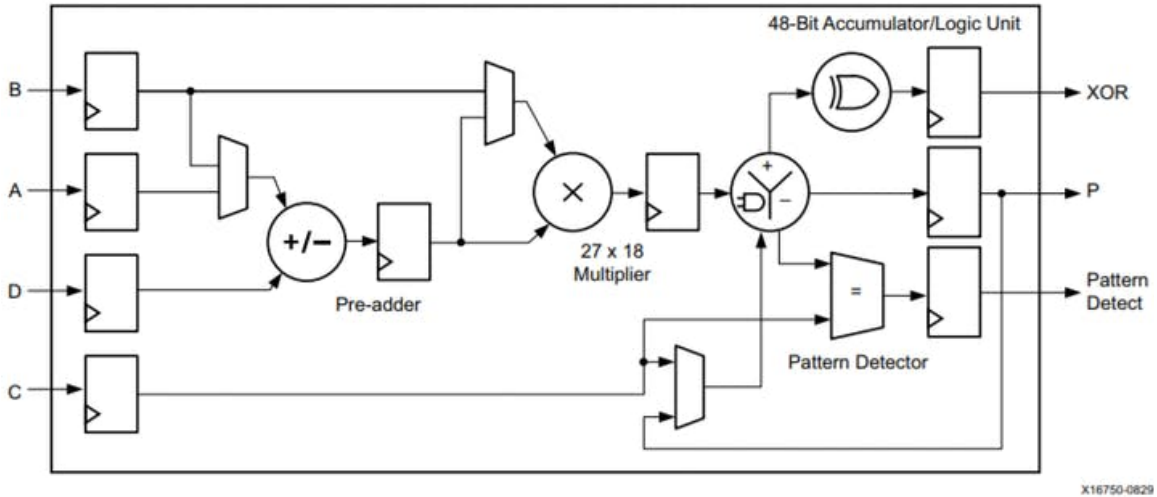
Figure 5.7: High-level block diagram of the DSP48E2 slice in Xilinx FPGAs [102].

Table 5.3 shows the FPGA resources utilized in each of the four parallel DPD branches. The table shows the number of look-up table (LUT) slices, flip-flops (FFs) and DSP slices utilized per branch by the proposed DPD model as well as those utilized when the proposed PWL functions (i.e., unequal segments of $|s[n]|^2$) are replaced by those in [94] (i.e., equal segments of $|s[n]|$). The square-root function for the model in [94] was implemented using Xilinx' coordinate-rotation digital computer (CORDIC) logic core. This ultra-efficient implementation involves no multiplications or divisions, but only additions, subtractions, bit-shift, and LUT operations. The downside of this efficient implementation is the signifi-

88

cant increase in latency (as Table 5.3 shows) and the restriction imposed on the maximum clock frequency. For the device in use, the maximum clock frequency supported by the CORDIC square-root core is only 254 MHz [103].

Table 5.3: FPGA Resources utilized per branch with $N = 6$ and $M = 4$.

	LUT slices	FFs	DSP slices	Latency in clock cycles
With PWL in [94]	5617	4028	61	34
With Proposed PWL	5286	3023	61	16
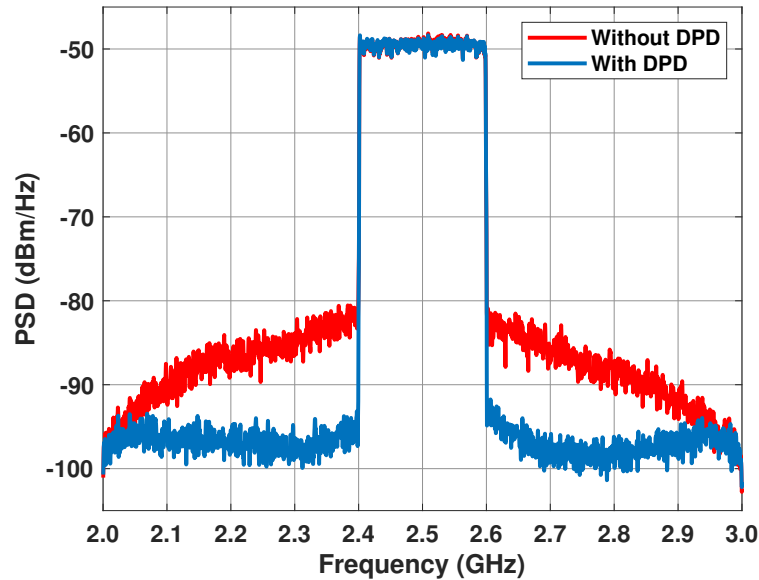
Figure 5.8: Output spectrum of the Wolfspeed CGH27015-TB PA with and without the proposed PWL-based DPD.

Fig. 5.8 shows the output spectrum of the PA with and without the proposed DPD implementation, where it can be seen that a 1-GHz linearization bandwidth was achieved with a core clock of 250 MHz. DPD improved the RNMSE and lower/upper ACPRs from 4.5% and -34.7/-35.7 dB to 1.1% and -47.1/-47.3 dB respectively. The PWL scheme in [94] gives nearly identical results but, as shown in Table 5.3, requires more resources, increases latency, and restricts the maximum clock frequency possible. Although other less-resource-efficient implementations of the square-root function can enable a higher clock frequency,

this problem can be avoided altogether by employing the proposed PWL implementation. Finally, with the proposed parallelization architecture, the number of cross-branch connections needed to implement the PWL DPD model in (5.36) is about one third of that required by the architecture in [100] since this model employs three types of cross terms.

5.3   Summary

In this chapter, we proposed two techniques that reduce the computational and power overheads of the DPD subsystem. First, a computationally efficient algorithm for estimating the delay and phase offsets between the transmitter and the TOR was presented. The proposed algorithm is more accurate and less resource-consuming than the two-dimensional exhaustive search methods employed in prior works. Second, a PWL-based DPD model, along with its parallelized implementation, was presented. The proposed model requires less hardware resources to implement and introduces less latency when compared with similar works in the literature. The proposed model was implemented on a commercially available FPGA, and was used to achieve a 1-GHz linearization bandwidth with a core clock frequency of only 250 MHz.

Chapter 6

Conclusion

Massive MIMO technology has emerged as one of the main pillars of 5G and future wireless systems. Through the utilization of tens or hundreds of RF transceiver chains, a 5G basestation can serve multiple users in the same time-frequency resource block, thereby substantially improving the spectral efficiency. Nevertheless, the adoption of massive MIMO technology in 5G basestations is met with a number of challenges. One of these is mitigating the hardware limitations and imperfections of all RF chains in real time. Most required digital compensation techniques in MIMO systems are straightforward extensions of their counterparts in SISO systems, with the most prominent exception being DPD. In a highly integrated MIMO transmitter, a DPD module must not only compensate for PA nonlinearity, but also for nonlinear crosstalk effects arising from unavoidable inter-antenna coupling. Furthermore, since tens or hundreds of low-power PAs are to be employed instead of a single high-power one, the overhead power budget for per-chain DPD (as a percentage of the PA transmit power) must be reduced to maintain a reasonable overall efficiency. The power overhead incurred includes the power consumed by the logic circuits in the always-running DPD engine and that consumed by the TOR required to capture the PA output and update the DPD coefficients.

This thesis has addressed the above-mentioned challenges facing the successful application of DPD in massive MIMO transmitters, and provided effective solutions that minimize the computational and power overheads incurred. The key contributions are as follows:

6.1 Summary of Contributions

1. In this work, we have analyzed the impact of precoding on the RF performance of massive MIMO transmitters exhibiting non-negligible antenna crosstalk. It was shown that the disparity in average-power levels arising from conventional precoding schemes (MRT, ZF, and MMSE) leads to substantial variations in the average active loads seen at the PA outputs. This load modulation behavior gives rise to channel-dependent variations in the RF performance and linearity of the PAs. We demonstrated that, although precoding is a system-level function that serves to mitigate multi-user channel effects, it has a direct impact on the RF performance of the PAs. Hence, the DPD and precoding subsystems should not be operated independently from one another.

2. Based on the aforementioned analysis, we proposed two solutions that ensure excellent linearity across all channel conditions. The first comprises a load-dependent DPD architecture and a low-complexity algorithm that reduces the disparity in average-power levels arising from the conventional precoders. The second comprises alternate precoding schemes that fully eliminate the disparity in average-power levels across the RF chains and, consequently, simplify the required DPD architecture. The proposed solutions exploit the additional degrees of freedom offered by the fact that the number of users is less than the number of chains in a MIMO system. Both solutions were experimentally validated on a prototype two-user four-chain MIMO system with 100-MHz OFDM signals, where the obtained results confirmed the efficacy of the proposed methods. Although these results were obtained using a relatively small MIMO transmitter, similar trends are expected in larger systems, as evident from the numerical simulations and theoretical analysis provided.

3. Finally, we proposed two techniques that reduce the computational and power overheads of the DPD subsystem. First, we formulated a computationally efficient algorithm for estimating the delay and phase offsets between the transmitter and the TOR used for DPD training. The proposed algorithm is more accurate and less resource-consuming than the exhaustive search methods employed in the literature. Second, we presented a PWL-based DPD model, along with its parallelized implementation, that requires less hardware resources to implement and introduces less latency when compared with prior works. The proposed model was implemented on a commercially available FPGA, where it achieved a 1-GHz linearization bandwidth with a core clock frequency of only 250 MHz.

6.2 Future Work

This work has investigated the effects of precoding and antenna crosstalk on the linearizability of the PAs in a massive MIMO system, and provided robust solutions that stabilize the RF performance across all channel conditions. Yet, these solutions were validated on a relatively small MIMO transmitter, and in a controlled lab environment. Thus, future research on the subject must be carried out on larger prototype transmitters, with more complex PA and antenna designs, to allow for a better understanding of performance-complexity trade-offs in realistic deployment scenarios. Moreover, future testing and investigation should be carried out with the transmitter deployed in an outdoor environment that features rich multi-path scattering, instead of an anechoic chamber. This would enable a more accurate prediction of the overall system performance in dense urban environments.

In addition, a realistic prototype transmitter should have all DSP functionalities implemented on signal processing hardware (e.g., FPGAs). In this work, however, all multi-channel experiments were carried out with a computer running MATLAB as the DSP unit (because of the limited availability of equipment). Since the use of FPGAs here was limited to a single-channel setting, some of the challenges associated with the FPGA implementation of multi-channel DPD were not addressed. Of particular significance are the timing constraints associated with on-chip routing. If the cross-channel routing structure is not properly designed, the maximum FPGA clock frequency can be severely limited. Another challenge is the limited DSP resources available on commercial FPGAs. Accordingly, it is expected that multiple FPGA chips would be needed to implement all required DSP functions, which would bring about the challenge of inter-chip synchronization and data transfer.

Finally, an interesting area of research is extending the proposed techniques and algorithms in this work to the multi-band transmission case. If the basestation transmitter covers multiple non-contiguous frequency bands, the employed DPD in each band must eliminate inter-band distortion as well. Multi-band DPD techniques in SISO systems are relatively well-studied, but there are virtually no works on multi-band MIMO-DPD.

6.3 List of Publications

1. **M. Almoneer**, P. Mitran and S. Boumaiza, "I/Q Imbalance Compensation in Wideband Millimeter-Wave Transmitters Using a Single Undersampling ADC," in *IEEE Transactions on Circuits and Systems I: Regular Papers*, vol. 67, no. 8, pp. 2730-2738, Aug. 2020.

2. **M. Almoneer**, P. Mitran and S. Boumaiza, "Investigation of the Impact of Zero-Forcing Precoding on the Variation of Massive MIMO Transmitters' Performance With Channel Conditions," in *IEEE Microwave and Wireless Components Letters*, vol. 31, no. 6, pp. 802-805, Jun. 2021.

3. **M. Almoneer**, H. Barkhordar-pour, P. Mitran and S. Boumaiza, "Hardware-Efficient Implementation of Piece-wise Digital Predistorters for Wideband 5G Transmitters," Accepted in the *2022 IEEE MTT-S International Microwave Symposium (IMS)*.

4. **M. Almoneer**, J. G. Lim, H. Yu, P. Mitran and S. Boumaiza, "Massive MIMO Precoding Methods that Minimize the Variation in Average Power and Active Impedance with Channel Conditions," Revised version submitted on 14.03.2022 to the *IEEE Transactions on Microwave Theory and Techniques*.

5. **M. Almoneer**, P. Mitran and S. Boumaiza, "Low-complexity Precoding and Load-aware DPD for Improved Linearization of MIMO Transmitters," Submitted to the *IEEE Transactions on Circuits and Systems II: Express Briefs*.

References

[1] A. Gupta and R. K. Jha, "A Survey of 5G Network: Architecture and Emerging Technologies," *IEEE Access*, vol. 3, pp. 1206–1232, 2015.

[2] M. Agiwal, A. Roy, and N. Saxena, "Next Generation 5G Wireless Networks: A Comprehensive Survey," *IEEE Commun. Surveys Tuts.*, vol. 18, no. 3, pp. 1617–1655, Thirdquarter 2016.

[3] T. L. Marzetta, "Noncooperative Cellular Wireless with Unlimited Numbers of Base Station Antennas," *IEEE Trans. Wireless Commun.*, vol. 9, no. 11, pp. 3590–3600, Nov. 2010.

[4] F. Rusek, D. Persson, B. K. Lau, E. G. Larsson, T. L. Marzetta, O. Edfors, and F. Tufvesson, "Scaling Up MIMO: Opportunities and Challenges with Very Large Arrays," *IEEE Signal Process. Mag.*, vol. 30, no. 1, pp. 40–60, Jan. 2013.

[5] E. G. Larsson, O. Edfors, F. Tufvesson, and T. L. Marzetta, "Massive MIMO for Next Generation Wireless Systems," *IEEE Commun. Mag.*, vol. 52, no. 2, pp. 186–195, Feb. 2014.

[6] T. L. Marzetta, E. G. Larsson, H. Yan, and H. Q. Ngo, *Fundamentals of Massive MIMO.* Cambridge, United Kingdom: Cambridge University Press, 2016.

[7] M. Shafi, A. F. Molisch, P. J. Smith, T. Haustein, P. Zhu, P. D. Silva, F. Tufvesson, A. Benjebbour, and G. Wunder, "5G: A Tutorial Overview of Standards, Trials, Challenges, Deployment, and Practice," *IEEE J. Sel. Areas Commun.*, vol. 35, no. 6, pp. 1201–1221, Jun. 2017.

[8] T. Schenk, *RF Imperfections in High-rate Wireless Systems.* Dodrecht, The Netherlands: Springer Netherlands, 2008.

[9] J. Wood, "System-Level Design Considerations for Digital Pre-Distortion of Wireless Base Station Transmitters," *IEEE Trans. Microw. Theory Tech.*, vol. 65, no. 5, pp. 1880–1890, May 2017.

[10] C. Fager, X. Bland, K. Hausmair, J. C. Cahuana, and T. Eriksson, "Prediction of Smart Antenna Transmitter Characteristics Using a New Behavioral Modeling Approach," in *2014 IEEE MTT-S International Microwave Symposium*, Tampa, FL, USA, 2014, pp. 1–4.

[11] K. Hausmair, S. Gustafsson, C. Sánchez-Pérez, P. N. Landin, U. Gustavsson, T. Eriksson, and C. Fager, "Prediction of Nonlinear Distortion in Wideband Active Antenna Arrays," *IEEE Trans. Microw. Theory Tech.*, vol. 65, no. 11, pp. 4550–4563, Nov. 2017.

[12] F. M. Barradas, P. M. Tomé, J. M. Gomes, T. R. Cunha, P. M. Cabral, and J. C. Pedro, "Power, Linearity, and Efficiency Prediction for MIMO Arrays With Antenna Coupling," *IEEE Trans. Microw. Theory Tech.*, vol. 65, no. 12, pp. 5284–5297, Dec. 2017.

[13] K. Hausmair, P. N. Landin, U. Gustavsson, C. Fager, and T. Eriksson, "Digital Predistortion for Multi-Antenna Transmitters Affected by Antenna Crosstalk," *IEEE Trans. Microw. Theory Tech.*, vol. 66, no. 3, pp. 1524–1535, Mar. 2018.

[14] E. Björnson, E. G. Larsson, and T. L. Marzetta, "Massive MIMO: Ten Mmyths and One Critical Qquestion," *IEEE Commun. Mag.*, vol. 54, no. 2, pp. 114–123, Feb. 2016.

[15] D. Galda and H. Rohling, "A Low Complexity Transmitter Structure for OFDM-FDMA Uplink Systems," in *2002 IEEE 55th Vehicular Technology Conference*, Birmingham, AL, 2002, pp. 1737–1741.

[16] S. B. Slimane, "Reducing the Peak-to-Average Power Ratio of OFDM Signals Through Precoding," *IEEE Trans. Veh. Technol.*, vol. 56, no. 2, pp. 686–695, Mar. 2007.

[17] C. Chung, "Spectrally Precoded OFDM," *IEEE Trans. Commun.*, vol. 54, no. 12, pp. 2173–2185, Dec. 2006.

[18] J. Vieira, F. Rusek, O. Edfors, S. Malkowsky, L. Liu, and F. Tufvesson, "Reciprocity Calibration for Massive MIMO: Proposal, Modeling, and Validation," *IEEE Trans. Wireless Commun.*, vol. 16, no. 5, pp. 3042–3056, May 2017.

[19] I. Ahmed, H. Khammari, A. Shahid, A. Musa, K. S. Kim, E. D. Poorter, and I. Moerman, "A Survey on Hybrid Beamforming Techniques in 5G: Architecture and System Model Perspectives," *IEEE Commun. Surveys Tuts.*, vol. 20, no. 4, pp. 3060–3097, Fourthquarter 2018.

[20] A. F. Molisch, V. V. Ratnam, S. Han, Z. Li, S. L. H. Nguyen, L. Li, and K. Haneda, "Hybrid Beamforming for Massive MIMO: A Survey," *IEEE Commun. Mag.*, vol. 55, no. 9, pp. 134–141, Sep. 2017.

[21] T. S. Rappaport, S. Sun, R. Mayzus, H. Zhao, Y. Azar, K. Wang, G. N. Wong, J. K. Schulz, M. Samimi, and F. Gutierrez, "Millimeter Wave Mobile Communications for 5G Cellular: It Will Work!" *IEEE Access*, vol. 1, pp. 335–349, 2013.

[22] S. Kutty and D. Sen, "Beamforming for Millimeter Wave Communications: An Inclusive Survey," *IEEE Commun. Surveys Tuts.*, vol. 18, no. 2, pp. 949–973, Secondquarter 2016.

[23] L. Ding, Z. Ma, D. R. Morgan, M. Zierdt, and G. T. Zhou, "Compensation of Frequency-Dependent Gain/Phase Imbalance in Predistortion Linearization Systems," *IEEE Trans. Circuits Syst. I*, vol. 55, no. 1, pp. 390–397, Feb. 2008.

[24] L. Anttila, M. Valkama, and M. Renfors, "Frequency-Selective I/Q Mismatch Calibration of Wideband Direct-Conversion Transmitters," *IEEE Trans. Circuits Syst. II*, vol. 55, no. 4, pp. 359–363, Apr. 2008.

[25] J. Luo, A. Kortke, W. Keusgen, and M. Valkama, "Efficient Estimation and Pilot-Free Online Re-Calibration of I/Q Imbalance in Broadband Direct-Conversion Transmitters," *IEEE Trans. Veh. Technol.*, vol. 63, no. 6, pp. 2506–2520, Jul. 2014.

[26] S. Cripps, *RF Power Amplifiers for Wireless Communications*, 2nd ed. Norwood, MA, USA: Artech House, 2006.

[27] T. May and H. Rohling, "Reducing the Peak-to-Average Power Ratio in OFDM Radio Transmission Systems," in *1998 IEEE 48th Vehicular Technology Conference*, vol. 3, Ottawa, ON, Canada, 1998, pp. 2474–2478.

[28] J. Armstrong, "Peak-to-average Power Reduction for OFDM by Repeated Clipping and Frequency Domain Filtering," *Electron. Lett.*, vol. 38, no. 5, pp. 246–247, Feb. 2002.

[29] M. Schetzen, *The Volterra and Wiener Theories of Nonlinear Systems.* Malabar, FL, USA: Krieger Publishing Company, 2006.

[30] S. Benedetto, E. Biglieri, and R. Daffara, "Modeling and Performance Evaluation of Nonlinear Satellite Links - A Volterra Series Approach," *IEEE Trans. Aerosp. Electron. Syst.*, vol. 15, no. 4, pp. 494–507, Jul. 1979.

[31] E. G. Lima, T. R. Cunha, H. M. Teixeira, M. Pirola, and J. C. Pedro, "Base-band Derived Volterra Series for Power Amplifier Modeling," in *2009 IEEE MTT-S International Microwave Symposium*, Boston, MA, USA, 2009, pp. 1361–1364.

[32] J. Kim and K. Konstantinou, "Digital Predistortion of Wideband Signals Based on Power Amplifier Model with Memory," *Electron. Lett.*, vol. 37, no. 23, pp. 1417–1418, Nov. 2001.

[33] L. Ding and G. T. Zhou, "Effects of Even-order Nonlinear Terms on Power Amplifier Modeling and Predistortion Linearization," *IEEE Trans. Veh. Technol.*, vol. 53, no. 1, pp. 156–162, Jan. 2004.

[34] M. Schetzen, "Theory of pth-order Inverses of Nonlinear Systems," *IEEE Trans. Circuits Syst.*, vol. 23, no. 5, pp. 285–291, May 1976.

[35] D. R. Morgan, Z. Ma, J. Kim, M. G. Zierdt, and J. Pastalan, "A Generalized Memory Polynomial Model for Digital Predistortion of RF Power Amplifiers," *IEEE Trans. Signal Process.*, vol. 54, no. 10, pp. 3852–3860, Oct. 2006.

[36] L. Guan and A. Zhu, "Simplified Dynamic Deviation Reduction-Based Volterra Model for Doherty Power Amplifiers," in *2011 Workshop on Integrated Nonlinear Microwave and Millimetre-Wave Circuits*, Vienna, Austria, 2011, pp. 1–4.

[37] F. Mkadem, M. C. Fares, S. Boumaiza, and J. Wood, "Complexity-reduced Volterra Series Model for Power Amplifier Digital Predistortion," *Analog Integr. Circ. Sig. Process.*, vol. 79, pp. 331–343, Feb. 2014.

[38] A. Zhu, "Decomposed Vector Rotation-Based Behavioral Modeling for Digital Predistortion of RF Power Amplifiers," *IEEE Trans. Microw. Theory Tech.*, vol. 63, no. 2, pp. 737–744, Feb. 2015.

[39] R. N. Braithwaite, "Memory Correction of a Doherty Power Amplifier with a WCDMA Input Using Digital Predistortion," in *2006 IEEE MTT-S International Microwave Symposium*, San Francisco, CA, USA, 2006, pp. 1526–1529.

[40] L. Ding, F. Mujica, and Z. Yang, "Digital Predistortion Using Direct Learning with Reduced Bandwidth Feedback," in *2013 IEEE MTT-S International Microwave Symposium Digest*, Seattle, WA, USA, 2013, pp. 1–3.

[41] T. Adali and S. Haykin, *Adaptive Signal Processing: Next Generation Solutions*. Hoboken, NJ, USA: John Wiley and Sons, 2010.

[42] A. H. Sayed, *Adaptive Filters*. Hoboken, NJ, USA: John Wiley and Sons, 2008.

[43] R. G. Vaughan, N. L. Scott, and D. R. White, "The Theory of Bandpass Sampling," *IEEE Trans. Signal Process.*, vol. 39, no. 9, pp. 1973–1984, Sep. 1991.

[44] *5G NR Base Station (BS) radio transmission and reception*, 3GPP TS 38.104 version 16.6.0 Release 16, Jan. 2021. [Online]. Available: https://www.etsi.org/deliver/etsi_ts/138100_138199/138104/16.06.00_60/ts_138104v160600p.pdf

[45] D. Pozar, *Microwave Engineering*, 4th ed. Hoboken, NJ, USA: John Wiley and Sons, 2011.

[46] J. Verspecht and D. E. Root, "Polyharmonic Distortion Modeling," *IEEE Microw. Mag.*, vol. 7, no. 3, pp. 44–57, Jun. 2008.

[47] M. Romier, A. Barka, H. Aubert, J. P. Martinaud, and M. Soiron, "Load-Pull Effect on Radiation Characteristics of Active Antennas," *IEEE Antennas Wireless Propag. Lett.*, vol. 7, pp. 550–552, 2008.

[48] S. Gustafsson, M. Thorsell, and C. Fager, "A Novel Active Load-pull System With Multi-band Capabilities," in *2013 81st ARFTG Microwave Measurement Conference*, Seattle, WA, USA, 2013, pp. 1–4.

[49] H. Zargar, A. Banai, and J. C. Pedro, "DIDO Behavioral Model Extraction Setup Using Uncorrelated Envelope Signals," in *2015 European Microwave Conference*, Paris, France, 2015, pp. 646–649.

[50] D. Nopchinda and K. Buisman, "Emulation of Array Coupling Influence on RF Power Amplifiers in a Measurement Setup," in *2016 87th ARFTG Microwave Measurement Conference*, San Francisco, CA, USA, 2016, pp. 1–4.

[51] G. Z. ElNashef, F. Torres, S. Mons, T. Reveyrand, T. Monediere, E. Ngoya, and R. Quere, "EM/Circuit Mixed Simulation Technique for an Active Antenna," *IEEE Antennas Wireless Propag. Lett.*, vol. 10, pp. 354–357, 2011.

[52] H. Zargar, A. Banai, and J. C. Pedro, "A New Double Input-Double Output Complex Envelope Amplifier Behavioral Model Taking Into Account Source and Load Mismatch Effects," *IEEE Trans. Microw. Theory Tech.*, vol. 63, no. 2, pp. 766–774, Feb. 2015.

[53] E. Zenteno, M. Isaksson, and P. Händel, "Output Impedance Mismatch Effects on the Linearity Performance of Digitally Predistorted Power Amplifiers," *IEEE Trans. Microw. Theory Tech.*, vol. 63, no. 2, pp. 754–765, Feb. 2015.

[54] Q. Luo, X. Zhu, C. Yu, and W. Hong, "Single-Receiver Over-the-Air Digital Predistortion for Massive MIMO Transmitters With Antenna Crosstalk," *IEEE Trans. Microw. Theory Tech.*, vol. 68, no. 1, pp. 301–315, Jan. 2020.

[55] N. Tervo, J. Aikio, T. Tuovinen, T. Rahkonen, and A. Parssinen, "Digital Predistortion of Amplitude Varying Phased Array Utilising Over-the-Air Combining," in *2017 IEEE MTT-S International Microwave Symposium*, Honololu, HI, USA, 2017, pp. 1165–1168.

[56] W. Pan, C. Li, X. Quan, W. Ma, Y. Liu, S. Shao, and Y. Tang, "Digital Linearization of Multiple Power Amplifiers in Phased Arrays for 5G Wireless Communications," in *2018 IEEE International Symposium on Signal Processing and Information Technology*, Louisville, KY, USA, 2018, pp. 247–251.

[57] M. Abdelaziz, L. Anttila, A. Brihuega, F. Tufvesson, and M. Valkama, "Digital Predistortion for Hybrid MIMO Transmitters," *IEEE J. Sel. Topics Signal Process.*, vol. 12, no. 3, pp. 445–454, Jun. 2018.

[58] E. Ng, Y. Beltagy, G. Scarlato, A. B. Ayed, P. Mitran, and S. Boumaiza, "Digital Predistortion of Millimeter-Wave RF Beamforming Arrays Using Low Number of Steering Angle-Dependent Coefficient Sets," *IEEE Trans. Microw. Theory Tech.*, vol. 67, no. 11, pp. 4479–4492, Nov. 2019.

[59] X. Liu, W. Chen, L. Chen, F. M. Ghannouchi, and Z. Feng, "Linearization for Hybrid Beamforming Array Utilizing Embedded Over-the-Air Diversity Feedbacks," *IEEE Trans. Microw. Theory Tech.*, vol. 67, no. 12, pp. 5235–5248, Dec. 2019.

[60] X. Wang, Y. Li, C. Yu, W. Hong, and A. Zhu, "Digital Predistortion of 5G Massive MIMO Wireless Transmitters Based on Indirect Identification of Power Amplifier Behavior With OTA Tests," *IEEE Trans. Microw. Theory Tech.*, vol. 68, no. 1, pp. 316–328, Jan. 2020.

[61] S. A. Bassam, M. Helaoui, and F. M. Ghannouchi, "Crossover Digital Predistorter for the Compensation of Crosstalk and Nonlinearity in MIMO Transmitters," *IEEE Trans. Microw. Theory Tech.*, vol. 57, no. 5, pp. 1119–1128, May 2009.

[62] D. Saffar, N. Boulejfen, F. M. Ghannouchi, A. Gharsallah, and M. Helaoui, "Behavioral Modeling of MIMO Nonlinear Systems With Multivariable Polynomials," *IEEE Trans. Microw. Theory Tech.*, vol. 59, no. 11, pp. 2994–3003, Nov. 2011.

[63] S. Amin, P. N. Landin, P. Händel, and D. Rönnow, "Behavioral Modeling and Linearization of Crosstalk and Memory Effects in RF MIMO Transmitters," *IEEE Trans. Microw. Theory Tech.*, vol. 62, no. 4, pp. 810–823, Apr. 2014.

[64] A. Abdelhafiz, L. Behjat, F. M. Ghannouchi, M. Helaoui, and O. Hammi, "A High-Performance Complexity Reduced Behavioral Model and Digital Predistorter for MIMO Systems With Crosstalk," *IEEE Trans. Commun.*, vol. 64, no. 5, pp. 1996–2004, May 2016.

[65] Z. A. Khan, E. Zenteno, P. Händel, and M. Isaksson, "Digital Predistortion for Joint Mitigation of I/Q Imbalance and MIMO Power Amplifier Distortion," *IEEE Trans. Microw. Theory Tech.*, vol. 65, no. 1, pp. 322–333, Jan. 2017.

[66] E. Björnson, J. Hoydis, and L. Sanguinetti, *Massive Mimo Networks: Spectral, Energy, and Hardware Efficiency.* Delft, The Netherlands: Now Publishers, 2017.

[67] T. A. Levanen, J. Pirskanen, T. Koskela, J. Talvitie, and M. Valkama, "Radio Interface Evolution Towards 5G and Enhanced Local Area Communications," *IEEE Access*, vol. 2, pp. 1005–1029, 2014.

[68] K. Karakayali, R. Yates, G. Foschini, and R. Valenzuela, "Optimum Zero-forcing Beamforming with Per-antenna Power Constraints," in *2007 IEEE International Symposium on Information Theory*, Nice, France, 2007, pp. 101–105.

[69] A. Wiesel, Y. C. Eldar, and S. Shamai, "Zero-Forcing Precoding and Generalized Inverses," *IEEE Trans. Signal Process.*, vol. 56, no. 9, pp. 4409–4418, Sep. 2005.

[70] R. Zhang, "Cooperative Multi-Cell Block Diagonalization with Per-Base-Station Power Constraints," *IEEE J. Sel. Areas Commun.*, vol. 28, no. 9, pp. 1435–1445, Dec. 2010.

[71] H. H. Dam, A. Cantoni, and B. Li, "A Fast Low Complexity Method for Optimal Zero-Forcing Beamformer MU-MIMO System," *IEEE Signal Process. Lett.*, vol. 22, no. 9, pp. 1443–1447, Sep. 2015.

[72] J. Jang, S. Jeon, H. Chae, H. Cha, and D. K. Kim, "Low Complexity Zeroforcing Precoder Design Under Per-Antenna Power Constraints," *IEEE Commun. Lett.*, vol. 19, no. 9, pp. 1556–1559, Sep. 2015.

[73] E. Björnson, M. Bengtsson, and B. Ottersten, "Optimal Multiuser Transmit Beamforming: A Difficult Problem with a Simple Solution Structure [Lecture Notes]," *IEEE Signal Process. Mag.*, vol. 31, no. 4, pp. 142–148, Jul. 2014.

[74] M. Joham, W. Utschick, and J. A. Nossek, "Linear Transmit Processing in MIMO Communications Systems," *IEEE Trans. Signal Process.*, vol. 53, no. 8, pp. 2700–2712, Aug. 2005.

[75] G. H. Golub and C. F. V. Loan, *Matrix Computations*, 4th ed. Baltimore, MD, USA: Johns Hopkins Univ Press, 2012.

[76] L. Lu, G. Y. Li, A. L. Swindlehurst, A. Ashikhmin, and R. Zhang, "An Overview of Massive MIMO: Benefits and Challenges," *IEEE J. Sel. Topics Signal Process.*, vol. 8, no. 5, pp. 742–758, Oct. 2014.

[77] S. boyd and L. Vandenberghe, *Convex Optimization.* Cambridge, UK: Cambridge University Press, 2004.

[78] W. Yu and T. Lan, "Transmitter Optimization for the Multi-Antenna Downlink with Per-Antenna Power Constraints," *IEEE Trans. Signal Process.*, vol. 55, no. 6, pp. 2646–2660, Jun. 2007.

[79] J. Nocedal and S. J. Wright, *Numerical Optimization*, 2nd ed. New York, NY, USA: Springer, 2006.

[80] K. B. Petersen and M. S. Pedersen, *The Matrix Cookbook.* Technical University of Denmark, 2012. [Online]. Available: http://www2.imm.dtu.dk/pubdb/edoc/imm3274.pdf

[81] C. Yu, L. Guan, E. Zhu, and A. Zhu, "Band-Limited Volterra Series-Based Digital Predistortion for Wideband RF Power Amplifiers," *IEEE Trans. Microw. Theory Tech.*, vol. 60, no. 12, pp. 4198–4208, Dec. 2012.

[82] Y. Ma, Y. Yamao, Y. Akaiwa, and K. Ishibashi, "Wideband Digital Predistortion Using Spectral Extrapolation of Band-Limited Feedback Signal," *IEEE Trans. Circuits Syst. I*, vol. 61, no. 7, pp. 2088–2097, Jul. 2014.

[83] Y. Liu, J. J. Yan, H. Dabag, and P. M. Asbeck, "Novel Technique for Wideband Digital Predistortion of Power Amplifiers with an Under-Sampling ADC," *IEEE Trans. Microw. Theory Tech.*, vol. 62, no. 11, pp. 2604–2617, Nov. 2014.

[84] Y. Liu, W. Pan, S. Shao, and Y. Tang, "A General Digital Predistortion Architecture Using Constrained Feedback Bandwidth for Wideband Power Amplifiers," *IEEE Trans. Microw. Theory Tech.*, vol. 63, no. 5, pp. 1544–1555, May 2015.

[85] H. Huang, P. Mitran, and S. Boumaiza, "Digital Predistortion Function Synthesis Using Undersampled Feedback Signal," *IEEE Microw. Wireless Compon. Lett.*, vol. 26, no. 10, pp. 855–857, Oct. 2016.

[86] Z. Wang, W. Chen, G. Su, F. M. Ghannouchi, Z. Feng, and Y. Liu, "Low Feedback Sampling Rate Digital Predistortion for Wideband Wireless Transmitters," *IEEE Trans. Microw. Theory Tech.*, vol. 64, no. 11, pp. 3528–3539, Nov. 2016.

[87] J. Chani-Cahuana, M. zen, C. Fager, and T. Eriksson, "Digital Predistortion Parameter Identification for RF Power Amplifiers Using Real-Valued Output Data," *IEEE Trans. Circuits Syst. II*, vol. 64, no. 10, pp. 1227–1231, Oct. 2017.

[88] N. Guan, N. Wu, and H. Wang, "Digital Predistortion of Wideband Power Amplifier with Single Undersampling ADC," *IEEE Microw. Wireless Compon. Lett.*, vol. 27, no. 11, pp. 1016–1018, Nov. 2017.

[89] Z. Wang, L. Guan, and R. Farrell, "Undersampling Observation-Based Compact Digital Predistortion for Single-Chain Multiband and Wideband Direct-to-RF Transmitter," *IEEE Trans. Microw. Theory Tech.*, vol. 65, no. 12, pp. 5274–5283, Dec. 2017.

[90] Y. Beltagy, P. Mitran, and S. Boumaiza, "Direct Learning Algorithm for Digital Predistortion Training Using Sub-Nyquist Intermediate Frequency Feedback Signal," *IEEE Trans. Microw. Theory Tech.*, vol. 67, no. 1, pp. 267–277, Jan. 2019.

[91] S. M. Kay, *Fundamentals of Statistical Signal Processing, Volume I: Estimation Theory*. Upper Saddle River, NJ, USA: Prentice Hall, 1993.

[92] T. I. Laakso, V. Valimaki, M. Karjalainen, and U. K. Laine, "Splitting the Unit Delay [FIR/All Pass Filters Design]," *IEEE Signal Process. Mag.*, vol. 13, no. 1, pp. 30–60, Jan. 1996.

[93] S. Afsardoost, T. Eriksson, and C. Fager, "Digital Predistortion Using a Vector-Switched Model," *IEEE Trans. Microw. Theory Tech.*, vol. 60, no. 4, pp. 1166–1174, Apr. 2012.

[94] A. Molina, K. Rajamani, and K. Azadet, "Digital Predistortion Using Lookup Tables with Linear Interpolation and Extrapolation: Direct Least Squares Coefficient Adaptation," *IEEE Trans. Microw. Theory Tech.*, vol. 65, no. 3, pp. 980–987, Mar. 2017.

[95] Y. Li, W. Cao, and A. Zhu, "Instantaneous Sample Indexed Magnitude-Selective Affine Function-Based Behavioral Model for Digital Predistortion of RF Power Amplifiers," *IEEE Trans. Microw. Theory Tech.*, vol. 66, no. 11, pp. 5000–5010, Nov. 2018.

[96] A. Brihuega, M. Abdelaziz, L. Anttila, M. Turunen, M. Allén, T. Eriksson, and M. Valkama, "Piecewise Digital Predistortion for mmWave Active Antenna Arrays: Algorithms and Measurements," *IEEE Trans. Microw. Theory Tech.*, vol. 68, no. 9, pp. 4000–4017, Sep. 2020.

[97] P. P. Campo, A. Brihuega, L. Anttila, M. Turunen, D. Korpi, M. Allén, and M. Valkama, "Gradient-Adaptive Spline-Interpolated LUT Methods for Low-Complexity Digital Predistortion," *IEEE Trans. Circuits Syst. I*, vol. 68, no. 1, pp. 336–349, Jun. 2021.

[98] Y. Li, X. Wang, J. Pang, and A. Zhu, "Boosted Model Tree-Based Behavioral Modeling for Digital Predistortion of RF Power Amplifiers," *IEEE Trans. Microw. Theory Tech.*, vol. 69, no. 9, pp. 3976–3988, Sep. 2021.

[99] A. Brihuega, M. Abdelaziz, L. Anttila, Y. Li, A. Zhu, and M. Valkama, "Mixture of Experts Approach for Piecewise Modeling and Linearization of RF Power Amplifiers," *IEEE Trans. Microw. Theory Tech.*, 2021.

[100] H. Huang, J. Xia, and S. Boumaiza, "Novel Parallel-Processing-Based Hardware Implementation of Baseband Digital Predistorters for Linearizing Wideband 5G Transmitters," *IEEE Trans. Microw. Theory Tech.*, vol. 68, no. 9, pp. 4066–4076, Sep. 2020.

[101] Z. Xu, J. Zhai, K. Wang, J. Liu, and C. Yu, "The Threshold Optimization of the Canonical Piecewise Linear Function-Based Model for RF PA Linearization," *IEEE Microw. Wireless Compon. Lett.*, 2021.

[102] *UltraScale Architecture DSP Slice User Guide, UG579 (v1.11)*, Xilinx, Inc., Aug. 2021. [Online]. Available: https://www.xilinx.com/support/documentation/user_guides/ug579-ultrascale-dsp.pdf

[103] *Performance and Resource Utilization for CORDIC v6.0*, Xilinx, Inc., Aug. 2021. [Online]. Available: https://www.xilinx.com/html_docs/ip_docs/pru_files/cordic.html

APPENDICES

Appendix A

Estimating Delay and Phase Offsets in Conventional TOR Architectures

Using Fig. 2.4b and the PA model in (2.9), the baseband feedback signal $y[n]$ can be expressed in terms of the baseband predistorted signal $z[n]$, in the presence of circularly-symmetric complex-valued AWGN $\eta[n]$, as

$$y[n] \approx h_0 e^{j\theta} z[n - n_0] + \eta[n], \qquad (A.1)$$

where n_0 is the system delay, h_0 is the nominal channel gain, and θ is the combined phase offset due to transmitter circuitry and phase incoherence. Note that h_0 is restricted to being a positive real value as the phase of the system response is absorbed into θ. The equation above represents a good approximation if the PA is weakly nonlinear.

Let N be the number of signal-containing samples of $z[n]$ and $S > N$ be the total number of received samples of $y[n]$ where the extra $S - N$ samples contain no signal component, i.e., only AWGN. Assuming that n_0 is an integer, (A.1) can be expressed as

$$y[n] = \eta[n] + \begin{cases} 0, & 0 \leq n < n_0 \\ \alpha z[n - n_0] \,, & n_0 \leq n < n_0 + N \,, \\ 0, & n_0 + N \leq n < S \end{cases} \qquad (A.2)$$

where $\alpha = h_0 e^{j\theta}$. Since $\eta[n]$ is circularly-symmetric AWGN, the likelihood function is [91]

$$p(\mathbf{y}; \alpha, n_0) = \frac{1}{(\pi\sigma^2)^S} \prod_{n=0}^{n_0-1} \exp\left(\frac{-\left|y[n]\right|^2}{\sigma^2}\right) \cdot \prod_{n=n_0+N}^{S-1} \exp\left(\frac{-\left|y[n]\right|^2}{\sigma^2}\right)$$
$$\cdot \prod_{n=n_0}^{n_0+N-1} \exp\left(\frac{-1}{\sigma^2}\left|y[n] - \alpha z[n - n_0]\right|^2\right), \tag{A.3}$$

where σ^2 is the AWGN power. The negative of the logarithm of the likelihood function, after omitting constant factors and changing the summation index of the last term, can be expressed as

$$C(\alpha, n_0) = \sum_{n=0}^{n_0-1} \left|y[n]\right|^2 + \sum_{n=n_0+N}^{S-1} \left|y[n]\right|^2 + \sum_{n=0}^{N-1} \left|y[n + n_0] - \alpha z[n]\right|^2$$
$$= \sum_{n=0}^{n_0-1} \left|y[n]\right|^2 + \sum_{n=n_0+N}^{S-1} \left|y[n]\right|^2 + (\mathbf{y}(n_0) - \alpha\,\mathbf{z})^H (\mathbf{y}(n_0) - \alpha\,\mathbf{z}), \tag{A.4}$$

where $\mathbf{y}(n_0) = [y[n_0], \ldots, y[n_0 + N - 1]]^T$, and $\mathbf{z} = [z[0], \ldots, z[N - 1]]^T$. The ML estimates of the two parameters (α, n_0) are obtained by maximizing the likelihood function in (A.3), or equivalently, minimizing $C(\alpha, n_0)$. For any n_0, the above function is quadratic in α and is minimized by [91]

$$\hat{\alpha} = \left(\mathbf{z}^H \mathbf{z}\right)^{-1} \mathbf{z}^H \mathbf{y}(n_0). \tag{A.5}$$

Substituting this back in (A.4) yields

$$C(\hat{\alpha}, n_0) = \sum_{n=0}^{n_0-1} \left|y[n]\right|^2 + \sum_{n=n_0+N}^{S-1} \left|y[n]\right|^2$$
$$+ \left(\left[\mathbf{I} - \mathbf{z}\left(\mathbf{z}^H\mathbf{z}\right)^{-1}\mathbf{z}^H\right]\mathbf{y}(n_0)\right)^T \cdot \left(\left[\mathbf{I} - \mathbf{z}\left(\mathbf{z}^H\mathbf{z}\right)^{-1}\mathbf{z}^H\right]\mathbf{y}(n_0)\right)$$
$$= \sum_{n=0}^{n_0-1} \left|y[n]\right|^2 + \sum_{n=n_0+N}^{S-1} \left|y[n]\right|^2 + \mathbf{y}^H(n_0)\left(\mathbf{I} - \mathbf{z}\left(\mathbf{z}^H\mathbf{z}\right)^{-1}\mathbf{z}^H\right)\mathbf{y}(n_0)$$
$$= \sum_{n=0}^{S-1} \left|y[n]\right|^2 - \mathbf{y}^H(n_0)\mathbf{z}\left(\mathbf{z}^H\mathbf{z}\right)^{-1}\mathbf{z}^H\mathbf{y}(n_0)$$
$$= \sum_{n=0}^{S-1} \left|y[n]\right|^2 - \left(\mathbf{z}^H\mathbf{z}\right)^{-1}\left|\mathbf{z}^H\mathbf{y}(n_0)\right|^2, \tag{A.6}$$

where the fact that $\mathbf{y}^H(n_0)\mathbf{y}(n_0) = \sum_{n=0}^{N-1} |y[n+n_0]|^2 = \sum_{n=n_0}^{n_0+N-1} |y[n]|^2$ was utilized. Since the first term is not a function of n_0 and $(\mathbf{z}^H\mathbf{z})^{-1} > 0$, the ML estimate of n_0 is simply obtained by maximizing $|\mathbf{z}^H\mathbf{y}(n_0)|$. The ML estimates of h_0 and θ can then be obtained from (A.5).

Although n_0 was assumed to be an integer in the derivation above, equation (A.6) remains valid for non-integer values of n_0 as well. The integer part of the delay should be obtained first through cross-correlating $\mathbf{z}^H$ with $\mathbf{y}(d)$ for integer-valued $d \in [0, S-N]$. The remaining fractional delay can be estimated by interpolating the cross-correlation function $L(d) = |\mathbf{z}^H\mathbf{y}(d)|$ around the estimated integer delay and finding the maximum. It can then be compensated for using fractional delay filters [92].

Appendix B

Evaluating the Jacobian Matrices in Section 4.1

The derivatives of the set of functions defined in (4.10) with respect to $\mathbf{w}_R, \mathbf{w}_I, t, \mu_1, \ldots, \mu_K$ are:

$$
\frac{\partial f_i}{\partial \mathbf{w}_R} =
\begin{cases}
\left(\mathbf{C}_R^T \mathbf{C}_R + \mathbf{C}_I^T \mathbf{C}_I + \sum_{k=1}^K \mu_k \mathbf{B}_k \right)^T \mathbf{v}_i, & i = 1, \ldots, KL \\
\left(-\mathbf{C}_I^T \mathbf{C}_R + \mathbf{C}_R^T \mathbf{C}_I \right)^T \mathbf{v}_{(i-KL)}, & i = KL+1, \ldots, 2KL \\
\mathbf{0}_{(KL) \times 1}, & i = 2KL+1 \\
2 \mathbf{B}_k \mathbf{w}_R, & i = 2KL+2, \ldots, 2KL+K+1
\end{cases}
$$

$$
\frac{\partial f_i}{\partial \mathbf{w}_I} =
\begin{cases}
\left(-\mathbf{C}_R^T \mathbf{C}_I + \mathbf{C}_I^T \mathbf{C}_R \right)^T \mathbf{v}_i, & i = 1, \ldots, KL \\
\left(\mathbf{C}_I^T \mathbf{C}_I + \mathbf{C}_R^T \mathbf{C}_R + \sum_{k=1}^K \mu_k \mathbf{B}_k \right)^T \mathbf{v}_{(i-KL)}, & i = KL+1, \ldots, 2KL \\
\mathbf{0}_{(KL) \times 1}, & i = 2KL+1 \\
2 \mathbf{B}_k \mathbf{w}_I, & i = 2KL+2, \ldots, 2KL+K+1
\end{cases}
$$

$$
\frac{\partial f_i}{\partial t} =
\begin{cases}
0, & i = 1, \ldots, 2KL+1 \\
-1, & i = 2KL+2, \ldots, 2KL+K+1
\end{cases}
$$

$$
\frac{\partial f_i}{\partial \mu_k} =
\begin{cases}
\mathbf{v}_i^T \left(\mathbf{B}_k \mathbf{w}_R \right), & i = 1, \ldots, KL \\
\mathbf{v}_{(i-KL)}^T \left(\mathbf{B}_k \mathbf{w}_I \right), & i = KL+1, \ldots, 2KL \\
-1, & i = 2KL+1 \\
0, & i = 2KL+2, \ldots, 2KL+K+1,
\end{cases}
$$

where $\mathbf{v}_i$ is a $(KL) \times 1$ all-zero vector with a one in the ith position. The Jacobian matrix can then be formed, as in (4.11), using these derivatives and the fact that

$$\begin{bmatrix} \mathbf{v}_1^T \mathbf{F} \\ \vdots \\ \mathbf{v}_{KL}^T \mathbf{F} \end{bmatrix} = \mathbf{F}$$

when the number of rows of $\mathbf{F}$ is KL.

Likewise, the derivatives of the set of functions defined in (4.21) with respect to $\mathbf{w}_R, \mathbf{w}_I, \beta, \mu_1, \ldots, \mu_K$ are:

$$\frac{\partial f_i}{\partial \mathbf{w}_R} = \begin{cases} \left(\mathbf{Q}_R + \beta^2 \sum_{k=1}^{K} \mu_k \mathbf{B}_k \right)^T \mathbf{v}_i, & i = 1, \ldots, KL \\ \mathbf{Q}_I^T \mathbf{v}_{(i-KL)}, & i = KL+1, \ldots, 2KL \\ \beta \, \mathbf{h}_R - 2 \, \mathbf{Q}_R \mathbf{w}_R - 2 \, \mathbf{Q}_I^T \mathbf{w}_I, & i = 2KL+1 \\ 2 \, \mathbf{B}_k \mathbf{w}_R, & i = 2KL+2, \ldots, 2KL+K+1 \end{cases}$$

$$\frac{\partial f_i}{\partial \mathbf{w}_I} = \begin{cases} -\mathbf{Q}_I^T \mathbf{v}_i, & i = 1, \ldots, KL \\ \left(\mathbf{Q}_R + \beta^2 \sum_{k=1}^{K} \mu_k \mathbf{B}_k \right)^T \mathbf{v}_{(i-KL)}, & i = KL+1, \ldots, 2KL \\ -\beta \, \mathbf{h}_I - 2 \, \mathbf{Q}_R \mathbf{w}_I - 2 \, \mathbf{Q}_I \mathbf{w}_R & i = 2KL+1 \\ 2 \, \mathbf{B}_k \mathbf{w}_I, & i = 2KL+2, \ldots, 2KL+K+1 \end{cases}$$

$$\frac{\partial f_i}{\partial \beta} = \begin{cases} \mathbf{v}_i^T \left(-\mathbf{h}_R + 2\beta \sum_{k=1}^{K} \mu_k \mathbf{B}_k \mathbf{w}_R \right), & i = 1, \ldots, KL \\ \mathbf{v}_{(i-KL)}^T \left(\mathbf{h}_I + 2\beta \sum_{k=1}^{K} \mu_k \mathbf{B}_k \mathbf{w}_I \right), & i = KL+1, \ldots, 2KL \\ \mathbf{h}_R^T \mathbf{w}_R - \mathbf{h}_I^T \mathbf{w}_I, & i = 2KL+1 \\ 0, & i = 2KL+2, \ldots, 2KL+K+1 \end{cases}$$

$$\frac{\partial f_i}{\partial \mu_k} = \begin{cases} \beta^2 \, \mathbf{v}_i^T \left(\mathbf{B}_k \mathbf{w}_R \right), & i = 1, \ldots, KL \\ \beta^2 \, \mathbf{v}_{(i-KL)}^T \left(\mathbf{B}_k \mathbf{w}_I \right), & i = KL+1, \ldots, 2KL \\ 0, & i = 2KL+1, \ldots, 2KL+K+1. \end{cases}$$

The corresponding Jacobian matrix is that in (4.22).